TECHNISCHE UNIVERSITÄT MÜNCHEN
Department Chemie
Lehrstuhl I für Technische Chemie

Mechanistic modeling of reaction kinetics and dynamic changes in catalyst morphology on a mesoscopic scale

Maximilian Peter

Vollständiger Abdruck der von der Fakultät für Chemie der Technischen Universität München zur Erlangung des akademischen Grades eines

Doktor-Ingenieurs (Dr.-Ing.)

genehmigten Dissertation.

Vorsitzender:	Univ.-Prof. Dr. Karsten Reuter
Prüfer der Dissertation:	1. Univ.-Prof. Dr.-Ing. Kai-Olaf Hinrichsen
	2. Univ.-Prof. Dr.-Ing. Harald Klein

Die Dissertation wurde am 17.01.2012 bei der Technischen Universität München eingereicht und durch die Fakultät für Chemie am 20.06.2012 angenommen.

Acknowledgments

As a doctoral candidate many challenges during the last years had to be managed. These were mostly, but not always, of scientific nature. I would like to thank all who have contributed to the success of this work within the last years.

First of all I would like to thank Prof. Dr.-Ing. Kai-Olaf Hinrichsen for giving me the opportunity to work in his research group at the Chair of Chemical Engineering. I am very grateful for the chance to work on a very interesting field in scientific research and for his guidance and supervision.

Furthermore, I would like to thank Prof. Dr. Martin Muhler for giving me the chance to collaborate with his group at the Ruhr-Universität Bochum on the field of methanol synthesis. In particular my special thank goes to Dr. Holger Ruland for providing his kinetic data and for discussing them. Furthermore I would like to thank Dr. Stefan Kaluza for nice and fruitful discussions at the Katalytikertagung in Weimar.

I would also like to mention all my colleagues, Dr. Karin Dänhardt, Dr. Susanne Witt, Cornelia Ablasser, Annemarie Frey, Dr. Georg Simson, Franz Haseidl, Holger Marschall, David Schlereth and especially my office colleagues, Dr. Nikolas Jacobsen, Robert Mornhinweg and Florian Habla, who helped a lot, discussing (non-)scientific topics and for having such a nice working atmosphere. During my last year Matthias Fichtl always had an open door for discussions, for which I am very thankful.

In this context I would also like to thank Heidi Holweck and Dr. Thomas Michel for the administrative support.

In particular I want to thank all students I advised during this thesis, who contributed a lot to the success, namely Tassilo von Aretin, Johannes Fendt, Hanna Sundberg, Manfred Greisel, Maximilian Moser, Patrick Schuh, Stefan Pleintinger, Stefan Kaiser, Arne Holtz, Mareike Braun, Marvin Maschke, Matthias Lenarz and Roland Schindl.

My personal thanks go to Conny, Steffi, Georg, Nik, Andi and Flo, who made working much more fun.

I am very grateful to Carmen, especially for all the patience and understanding.

Last but not least I would like to thank my family for the extraordinary support during my studies and for always being there when needed.

To my family...

Kurzzusammenfassung

In dieser Arbeit wird die Mikrokinetik der Methanolsynthese an ternären $Cu/ZnO/Al_2O_3$ Katalysatoren unter Einbindung struktureller Änderungen der Cu/ZnO-Grenzfläche behandelt. Dies schließt eine genauere Betrachtung der Wechselwirkung von Intermediaten mit dem Substrat und der Intermediate untereinander mit ein.

Die Kinetik der Methanolsynthese wird mit drei Modellen unterschiedlichen Detailgrads beschrieben. Neben einem Potenzansatz und einem Langmuir-Hinshelwood-Hougen-Watson-(LHHW)-Ansatz wird ein aus der Literatur angepasstes mikrokinetisches Modell verwendet. Das mikrokinetische Modell beschreibt die Strukturensitivität sowie die dynamische Veränderung der Katalysatormorphologie. Ein Vergleich mit experimentell ermittelten kinetischen Daten zeigt eine gute qualitative Übereinstimmung. Das auf Einkristallstudien unter Ultrahochvakuumbedingungen basierende Modell kann mittels zwei angepasster Parameter über mehrere Größenordnungen zur Beschreibung von Hochdruckexperimenten extrapoliert werden. Der Potenzansatz und das LHHW-Modell beschreiben die Kinetik der Methanolsynthese sehr genau, allerdings werden hierzu neun Parameter nahezu ohne Beschränkungen variiert. Das LHHW-Modell ist aus der Literatur übernommen und basiert auf einem spezifischen Reaktionsmechanismus, daher unterliegen die Modellparameter einigen physikalisch-chemischen Beschränkungen. Dies führt zu einer geringfügig schlechteren Beschreibung der Kinetik, als es beim Potenzansatz der Fall ist. Extrapoliert man beide Modelle, ergibt sich im Wesentlichen das gleiche Verhalten. Das mikrokinetische Modell beschreibt qualitativ die Strukturveränderungen des Katalysators. Es zeigt sich, dass besonders Wasser den Katalysator signifikant beeinflusst und die Methanolbildungsgeschwindigkeit durch die Oxidierung der Cu-Zn-Grenzfläche erheblich verlangsamt wird.

Darüber hinaus kann das mikrokinetische Modell zur theoretischen Untersuchung der anfänglichen Desaktivierung des Kupferkatalysators herangezogen werden. Für die Desaktivierung wird aktuell thermisches Sintern als Hauptgrund für die Aktivitätsabnahme während der Methanolsynthese angenommen. Es kann gezeigt werden, dass durch die Berücksichtigung von irreversiblen Strukturänderungen als zusätzlichen Desaktivierungsmechanismus die Übereinstimmung von Modell und Experiment während der ersten Stunden signifikant verbessert werden kann. Diese Änderungen könnten durch die Adsorption von Gasphasenmolekülen oder Oberflächenspezies hervorgerufen werden. Durch die irreversiblen Strukturänderungen könnte zusätzlich der ausgeprägte Unterschied bei der Desaktivierung zwischen verschieden reduzierenden Synthesegasen erklärt werden.

Die Morphologieänderungen werden darüber hinaus mittels temperaturprogrammierter Desorption von Wasserstoff untersucht. Zunächst wird eine mögliche Readsorptions- oder Massentransportlimitierung überprüft. Da die Adsorption von Wasserstoff an Kupferoberflächen stark aktiviert ist, kann ein bestehendes Kriterium für die innerpartikuläre Transportlimitierung erweitert werden. Die Absenz von Readsorption erlaubt es darüber hinaus die reine Desorptionskinetik an dem Katalysator zu untersuchen. Zu diesem

Zweck werden neben einer Analyse mit festem präexponentiellen Faktor die *lineshape analysis* Methode, die Heizratenvariation und eine numerische Modelloptimierung mit bedeckungsabhängiger Aktivierungsenergie herangezogen. Es zeigt sich, dass alle Methoden angewendet werden können. Allerdings sind einige nur dann gültig, wenn physikalisch sinnvolle Eingangsparameter bekannt sind. Ein fester präexponentieller Faktor sollte für die Kinetikanalyse nur dann gewählt werden, wenn dieser aus anderen Studien bekannt ist, um physikalisch sinnvolle Werte für die Aktivierungsenergie zu erhalten. Die *lineshape analysis* Methode zeigt gute Ergebnisse für mittlere Bedeckungsgrade an adsorbiertem Wasserstoff, allerdings ergibt sich eine schlechte experimentelle Übereinstimmung und unphysikalische Werte für einen vollständig bedeckten Katalysator. Mittels der Heizratenvariation werden physikalisch sinnvolle Mittelwerte extrahiert. Diese drei Methoden basieren auf den Annahmen einer Langmuir-Isotherme, was sich in zu schmalen Wasserstoffsignalen im Ausgangsstrom äußert. Daher wird für eine erweiterte Betrachtung eine bedeckungsabhängige Aktivierungsenergie eingeführt, was zu einer sehr genauen Übereinstimmung von Modell und Experiment führt. Die erhaltenen Parameter sind physikalisch sinnvoll, wenn für die Modellformulierung adäquate Startwerte, z.B. aus der Heizratenvariation, berücksichtigt werden. In Übereinstimmung mit der Literatur ergeben sich kinetische Parameter, die darauf hinweisen, dass unter diesen Bedingungen hauptsächlich Cu(111)-Flächen exponiert sind.

Ein während der Methanolsynthese desaktivierter Katalysator zeigte im Vergleich zu einem frischen Katalysator bezüglich der Anfangs- und Maximaltemperatur und auch der Form das gleiche Desorptionssignal an Wasserstoff. Eine Modelloptimierung ergibt daher dieselben Kinetikparameter für beide Katalysatoren. Demzufolge kann angenommen werden, dass durch die vorliegende Desaktivierung nur die Anzahl der aktiven Zentren verringert wird, die Katalysatormorphologie aber unverändert bleibt. Experimente an Katalysatoren, die mit CO vorbehandelt wurden, zeigten Signale, die mit zunehmender Vorbehandlungsdauer unsymmetrischer wurden. Mittels des bedeckungsabhängigen Modells, das bei Bedingungen, unter denen hauptsächlich Cu(111)-Flächen exponiert werden, erstellt wurde, kann nun gezeigt werden, dass sich der Katalysator umstrukturiert und Cu(110)- und Cu(100)-Ebenen aktiviert werden. Dieses dynamische Verhalten wurde auch schon an binären Cu/ZnO-Modellkatalysatoren mit geringen Kupferanteilen mittels *in-situ* EXAFS- und TEM-Experimenten gezeigt. Die Modellierung der Experimente mit einem hoch beladenen ternären Kupferkatalysator unter Normaldruck legt nahe, dass die Strukturänderungen auch näher an industriellen Bedingungen stattfinden.

Zusätzlich werden die Wechselwirkungen von Kohlenstoffmonoxid und dem ternären $Cu/ZnO/Al_2O_3$-Katalysator mittels temperaturgesteuerter Oberflächenreaktion von CO mit vorbeladenem Sauerstoff untersucht. Dies ist ein wichtiger Reaktionsschritt während der CO-Konvertierungsreaktion und daher auch der Methanolsynthese. Es zeigt sich, dass die Berücksichtigung einer logarithmischen Bedeckungsabhängigkeit gute Modellierungsergebnisse liefert. Diese Art der Oberflächenabhängigkeit ist in guter Übereinstimmung mit der geringen apparenten Aktivierungsenergie, die über einen großen Bedeckungsbereich an adsorbiertem Sauerstoff ermittelt wurde.

Abstract

This thesis focuses on the microkinetics of methanol synthesis over ternary $Cu/ZnO/Al_2O_3$ catalysts including catalyst morphology changes, especially due to changes in the Cu/ZnO interface. This further includes a closer analysis of adsorbate-substrate and adsorbate-adsorbate interactions.

The kinetics of methanol synthesis is described *via* three differently detailed kinetic model approaches, a power law and a Langmuir-Hinshelwood-Hougen-Watson (LHHW) approach as well as a microkinetic model adapted from literature. The microkinetic model, which includes structure sensitivity and dynamic catalyst morphology changes, shows good qualitative agreement between modeling and experimental results. This model is based on single crystal studies conducted in UHV. It is possible to extrapolate this model over several orders of magnitudes to describe high pressure experiments with only two parameters being optimized. The power law and LHHW model however, can predict the methanol formation rate very precisely, but nine almost freely varying parameters are required in model optimization. The LHHW model is adapted from literature and is based on a specific reaction scheme, hence constrained by some physico-chemical rules. This results in a slightly less accurate description of the kinetics, compared to the power law model. Both models exhibit essentially the same behavior upon model extrapolation. The microkinetic model qualitatively describes the catalysts morphology changes. It is shown that especially water may significantly influence the catalysts morphology and inhibits the methanol production rate by re-oxidation of the copper zinc interface, leading to a less active catalyst.

The experimentally observed initial deactivation of the copper catalyst during methanol synthesis is further theoretically studied using the microkinetic model. In general, sintering is believed to be the main cause for deactivation. It can be shown that an inclusion of irreversible catalyst morphology changes as a deactivation mechanism, induced by adsorption of gas-phase molecules or surface intermediates, may enhance the model experiment conformity during the first hours of operation. This catalyst re-structuring may furthermore explain the pronounced differences in deactivation behavior between differently reducing feed gases.

These morphology changes are further studied by the means of modeling hydrogen temperature-programmed flow experiments from the copper catalyst. First, possible effects of re-adsorption or mass transfer limitations are studied. Hereby, a criterion for intra-particle mass transfer limitations from literature can savely be enlarged, as hydrogen adsorption on the copper containing catalyst is a highly activated process. This further allows to study the pure desorption kinetics from this catalyst by the means of different analysis methods. The evaluated methods comprise of an analysis using a fixed pre-exponential factor, lineshape analysis, heating rate variation and full analysis including coverage-dependence. It is found that all methods can be applied, however, some are only valid when physical meaningful input parameters are known.

An analysis with a fixed pre-exponential factor should only be applied when a physically reasonable prefactor is initially known, i.e. from supporting experiments, to ensure valid values for the activation energy of desorption. Lineshape analysis showed good results for intermediate initial coverages of hydrogen, whereas it failed at full coverage. The heating rate variation extracts mean values, which are physical meaningful. These three methods are based on ideal Langmuirian assumptions and show too narrow hydrogen output signals compared to the experimental results. Hence, a full analysis comprising a coverage-dependent activation energy of desorption is introduced and proven to yield a very precise description of the experiments. The obtained parameters are physical meaningful when the model formulation is guided by appropriate initial values, i.e. from heating rate variation. The obtained kinetic parameters suggest that hydrogen is predominately desorbing from Cu(111) surface sites, which is consistent with literature.

Comparing a deactivated and fresh catalyst in terms of hydrogen temperature-programmed desorption, shows the same TPD signal, concerning onset and maximum temperature, as well as the shape of the resulting signal. Only the number of active sites decreased, hence, the same kinetic parameters are derived from a fresh and deactivated catalyst. Experiments with CO pre-treated catalysts showed a change in the very symmetric TPD signals. With increasing pre-treatment time the signals become highly unsymmetrical. Using the coverage-dependent model formulated under conditions where mainly Cu(111) planes are exposed, it is shown that Cu(110) and Cu(100) are activated during such a pre-treatment. This is consistent with *in-situ* EXAFS and TEM experiments with binary Cu/ZnO catalysts comprising a low copper loading. Here, it was shown that the catalyst undergoes structural changes, depending on the reduction potential of the gas phase. Modeling the experiments over a high copper loaded ternary catalyst under ambient pressure suggests that these changes also occur closer to industrial conditions.

In addition, the interactions of carbon monoxide and the ternary $Cu/ZnO/Al_2O_3$ catalyst are investigated by the means of modeling the temperature-programmed surface reaction of carbon monoxide and pre-adsorbed oxygen to yield carbon dioxide. This step is very important during water-gas shift and hence methanol synthesis reactions. It is found that an inclusion of a logarithmic coverage-dependence yields a good conformity between model and experiment. This kind of dependence can also capture the low apparent activation energy for this reaction, which was found over a wide range of oxygen coverages.

List of symbols

Latin symbols

A	[according to model]	Arrhenius factor
A	[m^2]	area
a	[-]	coefficient for coverage-dependence
B_i	[cm^{-1}]	rotational constant
b	[-]	coefficient for coverage-dependence
c	[$mol \cdot m^{-3}$]	concentration
c	[$m \cdot s^{-1}$]	speed of light
c_t	[$mol \cdot m^{-3}$]	total concentration of active sites
D	[-]	site density
D	[$m^2 \cdot s^{-1}$]	diffusion coefficient
D_{ab}	[$m^2 \cdot s^{-1}$]	molecular diffusion coefficient
D_{ax}	[$m^2 \cdot s^{-1}$]	axial dispersion coefficient
D_e	[$m^2 \cdot s^{-1}$]	effective diffusion coefficient
d	[m]	diameter
d	[m^{-2}]	number of active sites per area
E	[$J \cdot mol^{-1}$]	activation energy
F_{coll}	[$s^{-1} \cdot m^{-2}$]	number of collisions per second and area
f	[Pa]	fugacity, power law and microkinetic model
f	[bar]	fugacity, LHHW model
f	[arbitrary]	arbitrary function of coverage
$f_{1/2}$	[mol-%]	experimental/modeling result
$f\,(\gamma/\gamma_0)$	[-]	dimensionless surface area of particular copper facet from Wulff construction
G	[$J \cdot mol^{-1}$]	Gibbs free energy

g	[arbitrary]	arbitrary function of time
H	[J·mol^{-1}]	enthalpy
h	[Js]	Planck constant
I_{abc}	[kg$^3 \cdot$ m^6]	moment of inertia
hkl	[-]	Miller indices
j	[-]	running variable
k	[according to model]	reaction rate constant
k_B	[J·K^{-1}]	Boltzmann constant
K	[according to model]	equilibrium constant
K	[J·mol^{-1}]	factor of coverage-dependent activation energy
L	[m]	length
M_i	[kg·mol^{-1}]	molar mass of specific species
m_i	[kg]	mass of molecule
N	[mol]	number of active sites
N	[mol·g$_{\mathrm{cat}}^{-1}$]	coverage/number of active sites per catalyst weight
No	[-]	number of data points
n	[mol]	amount of substance
n	[m]	distance of surface normal to the center of the epitaxy
n	[-]	power of coverage-dependent activation energy
$\dot{n}$	[mol·s^{-1}]	molar flow rate
p	[Pa]	pressure
p_i	[Pa]	partial pressure
p_0	[according to model]	thermodynamic reference pressure
par	[-]	evaluated parameter in sensitivity analysis
PK	[-]	parameter for equilibrium constant
Q	[Nml·min^{-1}]	volumetric flow rate
q	[-]	molecular partition function
R	[J·mol^{-1}K^{-1}]	ideal gas constant
R_i	[s^{-1}]	overall rate for a specific species

r	[s^{-1}]	reaction rate, microkinetic model
r	[$mol \cdot s^{-1} \cdot kg_{cat}^{-1}$]	reaction rate, power law and LHHW model
$R_{MeOH,simulation}$	[$mol \cdot s^{-1} \cdot g_{cat}^{-1}$]	integral reaction rate methanol, simulation
$R_{MeOH,experimental}$	[$mol \cdot s^{-1} \cdot g_{cat}^{-1}$]	integral reaction rate methanol, experimental
r_p	[m]	radius of catalyst particle
S	[$J \cdot mol^{-1}$]	entropy
S	[-]	relative sensitivity
$S_{critical}$	[-]	value for criterion
Sn	[-]	stoichiometric number
s	[-]	sintering coefficient
s	[-]	sensitivity
s	[-]	sticking coefficient
T	[K]	temperature
$T_{Hüttig}$	[K]	Hüttig temperature
$T_{Tammann}$	[K]	Tammann temperature
$T_{melting}$	[K]	melting temperature
T_{max}	[K]	temperature at peak maximum
t	[s]	time
$\tilde{t}$	[-]	dimensionless time
u	[$m \cdot s^{-1}$]	superficial velocity
var	[-]	variation in sensitivity analysis
V	[m^3]	volume
X_{ref}	[mol-%]	reference value
x	[-]	dimensionless space coordinate
z	[-]	dimensionless space coordinate

Greek symbols

α	[-]	power of driving force in methanol synthesis
β	[-]	equilibrium term
β	[K·min^{-1}]	heating rate
β	[-]	normalized concentration of free active sites
χ	[-]	progress of restructuring
ϵ	[-]	fraction of Cu(110)
ϵ	[J]	energy
ϵ_b	[-]	bed porosity
ϵ_p	[-]	particle porosity
φ	[-]	power of driving force in reverse water-gas shift reaction
Γ	[-]	tortuosity factor
γ	[mol·m^{-3}s^{-1}]	source term
γ_{hkl}	[J·m^{-2}]	surface free energy
γ/γ_0	[-]	relative surface contact free energy
η	[-]	fraction of Cu(100)
λ	[-]	stoichiometric coefficient
ν	[-]	stoichiometric coefficient
θ	[-]	degree of coverage
ρ_p	[kg·m^{-3}]	particle density
σ	[-]	stoichiometric number of an elementary step
σ_i	[-]	symmetry factor
τ	[s]	residence time
ω	[cm^{-1}]	frustrated translational parameter
ω_{cat}	[g]	catalyst weight
ω_{e1}	[-]	degeneracy
ψ	[cm^{-1}]	vibrational parameter

ψ	[-]	irreversible change in relative surface contact free energy
ξ	[Pa]	inhibition term
ζ	[-]	fraction of Cu(111)

Contents

1 Introduction

1.1 Background

In chemical engineering microkinetic analysis has become increasingly important, i.e. for reaction and catalyst design [1, 2]. The understanding of principle processes occurring on catalysts surfaces is essential for a basic understanding of the particular catalytic process. The importance of such studies was recently outlined by the Nobel Prize in Chemistry awarded to Gehard Ertl in 2007 for "his studies of chemical processes on solid surfaces" [3]. In here, microkinetic analysis may serve as tool to combine fundamental concepts of surface chemistry and experimental studies [1, 2]. Starting from a specific elementary reaction mechanism, which is mostly formulated by chemical intuition and by means of spectroscopic studies of reaction intermediates, microkinetic analysis may support or guide further theoretical and experimental research [1, 2]. Hereby, different reaction schemes can be formulated to describe the general kinetics of a chemical process. However, a feasible mechanism should represent all significant chemistry on the surface, including all known intermediates and reactants [1, 2]. Influencing parameters on the reaction rate, in particular slow reaction steps and their interaction with the catalyst may be found *via* such an analysis [2]. The information can then further be used to synthesize new catalysts or to define more suitable reaction conditions. Hereby, all model input parameters should be physically meaningful and can either be estimated or measured. Figure 1.1 gives an overview of input parameters for the purpose of microkinetic analysis [4].

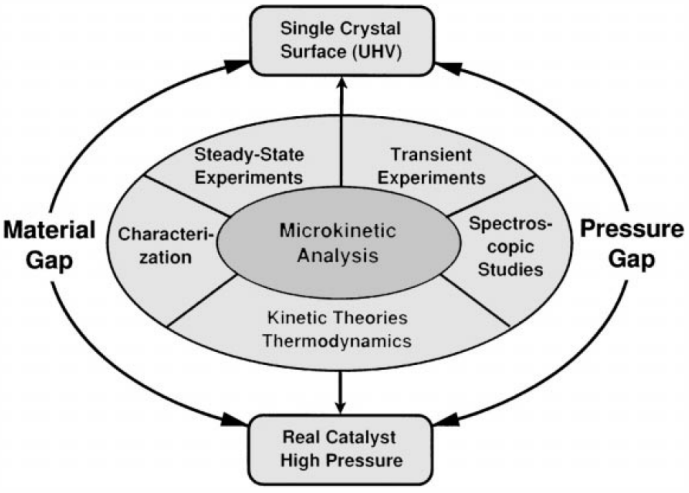

Figure 1.1: Microkinetic analysis [4].

Surface studies under ultrahigh vacuum (UHV) give important knowledge about reactions on well defined surfaces, which might be extrapolated to working conditions

(*pressure* and *material gap*) [4]. Furthermore, theoretical approaches like transition state or collision theory may provide physical meaningful input parameters for the model formulation.

Nowadays, with increasing computational performance, also density functional theory becomes more and more important for an *ab initio* description of microkinetic models. Hereby, the kinetic constants and thermodynamic properties can be approximated by density functional calculations and serve as a starting point for further investigations.

Waugh and co-workers [5, 6] and Stoltze and co-workers [7–9] introduced the *surface-science-approach*, where the kinetics includes a microscopic description of all molecular properties of the surface intermediates based on statistical thermodynamics and hence spectral properties [4]. These are usually determined under ideal conditions. Besides, at a *mesoscopic* scale, these parameters can be revisited and furthermore directly optimized with respect to experiments close to working conditions and also for porous catalyst systems, i.e. temperature-programmed flow experiments at ambient pressures. Hereby, the respective *pressure* and *material gap*, which may arise from parameters obtained under UHV conditions, is significantly reduced. The morphology of such catalysts can usually be defined by standard techniques, i.e. BET measurements [4].

Besides the microkinetic approach, semiempirical rate expressions (i.e. power laws) are widely used for catalyst and process design. The use of such an analysis differs from microkinetics, but is not less important [1]. Applications for a semiempirical analysis are for example reactor performance, heat and mass transfer or reactor stability issues [1].

The *surface-science-approach* was already proven to be able to bridge the *pressure* and *material gaps* between UHV and industrial conditions for the ammonia synthesis over iron catalysts by Stoltze and Nørskov [7–9]. Furthermore, especially the Topsøe group has extensively studied the water-gas shift reaction and methanol synthesis over copper single crystals [10–17]. Based on their findings Askgaard et al. [10] established a microkinetic model for methanol synthesis, which was later extended by Ovesen et al. [13] and could also be proven to describe the general kinetics for a commercial copper catalyst under industrial conditions. The inclusion of dynamical changes in the catalysts morphology led to significant model improvements.

A microkinetic description of chemical processes is often very tedious, a lot of input information is needed (see also figure 1.1). Thus, especially large scale processes as ammonia or methanol synthesis are among the most investigated issues. As methanol counts among the top three basic chemicals [18, 19], research on methanol synthesis is still a great issue. During the last decades methanol was mainly used to produce formaldehyde, methyl tertiary butyl ether (MTBE) and acetic acid. However, nowadays methanol capacity is mainly increasing due to its emerging use as an alternative fuel [19]. Besides MTBE as a fuel additive, methanol is now progressively used for gasoline blending and combustion, for biodiesel and for the production of dimethyl ether (DME) [20]. DME can be used as a substitute for propane in liquified natural gas. Processes like methanol to olefins (MTO) and methanol to gasoline (MTG) make methanol even more important as a building block for olefins and gasoline. Methanol is

believed to be a promising hydrogen storage, which could, in contrast to hydrogen itself or methane, as a liquid be used keeping the current gasoline infrastructure. Besides the re-conversion of methanol to hydrogen for the use of a hydrogen fuel cell, methanol can be used directly in the direct methanol fuel cell (DMFC). The high energy density, compared to conventional H_2-PEM fuel cells or batteries makes this usage highly valuable [19].

Intensive research has been conducted to reveal all relevant information about methanol synthesis, however, there is still a lack of understanding in different aspects for the used $Cu/ZnO/Al_2O_3$ catalyst system. The role of the different catalyst components is still under (controversial) debate [21–29]. Based on this, the long term stability and hence detailed deactivation mechanisms are still issues to be investigated [30]. Besides, the reaction mechanism and hence the kinetics of single reaction steps are still under investigation [10, 13, 31].

1.2 Objectives of the work

This work aims on the description of processes occuring in methanol synthesis over $Cu/ZnO/Al_2O_3$ catalysts. In order to further investigate proposed morphology changes as well as to enhance the knowledge about different important elementary reactions, a thorough modeling of the (surface) kinetics and of the catalyst morphology changes is conducted.

The first part comprises a differently detailed description of the methanol synthesis kinetics under industrial relevant conditions. Semiempirical rate expressions as well as a microkinetic description of the overall process are applied to describe the kinetics of methanol synthesis. These kinetic expressions are further investigated and compared with respect to their sensitivities and information level.

In the second part, the microkinetic model is further used to theoretically study the deactivation of the ternary copper catalyst. Hereby, thermal sintering and irreversible catalyst morphology changes are considered to cause the known decrease in methanol formation activity.

The detailed kinetics of hydrogen desorption from a ternary copper catalyst are investigated in the third part, also with respect to possible transfer limitations occurring during such experiments. Different evaluation methods are discussed to extract the desired kinetic parameters. Hereby, the typically applied Langmuir assumptions are reconsidered to describe this important surface process as accurate as possible.

This knowledge can then further be used to quantitatively study dynamical morphology changes on a ternary copper catalysts, which was up to now only be possible by *in-situ* methods on model systems. Finally, the knowledge of these changes can be used to model the CO oxidation, a very important step during water-gas shift and methanol synthesis reactions, to give a better description of surface dependencies, which may also occur due to a shift from UHV to ambient pressure conditions.

2 Theory

2.1 General aspects in methanol synthesis

2.1.1 The industrial process

Methanol is typically synthesized by synthesis gas, containing CO, CO_2 and H_2, over ternary $Cu/ZnO/Al_2O_3$ catalysts. This exothermic process is carried out at pressures ranging from 50 to 100 bar and temperatures from 473 – 573 K. After the invention of the high pressure methanol production process by BASF during the 1920s, methanol was commercially synthesized by a catalyst comprising chrome oxide and zinc oxide at pressures of 250 to 350 bar and temperatures ranging from 573 to 673 K. This catalyst was very stable against impurities from coal derived syngas. Lower levels of impurities, which can today be removed very efficiently, allowed the introduction of the copper zinc based catalyst during the 1960s, which is still used today. This process is also called low pressure process. Synthesizing at lower pressures and temperatures enhances the methanol production profitability. Also side products, like dimethyl ether, higher alcohols or methane, are drastically reduced - usually selectivites greater than 99% are achieved [19]. The methanol synthesis can be described by two global reaction pathways, the hydrogenation of CO (equation 2.1) and CO_2 (equation 2.2) [19]:

$$CO + 2\,H_2 \rightleftharpoons CH_3OH \qquad \Delta H_{298\,K} = -90.85\,kJ \cdot mol^{-1} \tag{2.1}$$

$$CO_2 + 3\,H_2 \rightleftharpoons CH_3OH + H_2O \qquad \Delta H_{298\,K} = -49.82\,kJ \cdot mol^{-1} \tag{2.2}$$

Both reaction pathways are highly exothermic and result in a decrease of volume, hence favored by low temperatures and high pressures, according to Le Chatelier's principle. Nowadays, especially isotope labeling experiments, but also transient pulse and step experiments with CO and CO_2 revealed that methanol is primarily formed *via* the hydrogenation of carbon dioxide [18, 32–34]. Besides the methanol synthesis reactions, the water-gas shift reaction plays an essential role during the process:

$$CO + H_2O \rightleftharpoons CO_2 + H_2 \qquad \Delta H_{298\,K} = -41.03\,kJ \cdot mol^{-1} \tag{2.3}$$

Equations 2.1, 2.2 and 2.3 are linear dependent, i.e. equation 2.1 can be expressed *via* 2.2 and 2.3. The low temperature water-gas shift reaction is also catalyzed by the ternary copper catalyst [14]. By the formation of carbon dioxide and hydrogen from carbon monoxide and water, the latter is removed from the reactive gas during reaction. As water is known to decrease the methanol production rate and enhance sintering of the particles, the water-gas shift reaction plays an essential role, also for the stability of the catalyst [33, 35–37]. The synthesis gas can be derived by many processes, among

those steam reforming and partial oxidation. The composition of the synthesis gas can be characterized by the stoichiometric number, ideally around 2 [19]:

$$Sn = \frac{n_{H_2} - n_{CO_2}}{n_{CO} + n_{CO_2}} \tag{2.4}$$

A stoichiometric number above 2 means an excess of hydrogen, whereas values below 2 indicate a hydrogen deficit. Depending on the production process a further (water-gas shift) treatment of the synthesis gas may become necessary to obtain an optimal hydrogen to carbon ratio [19].

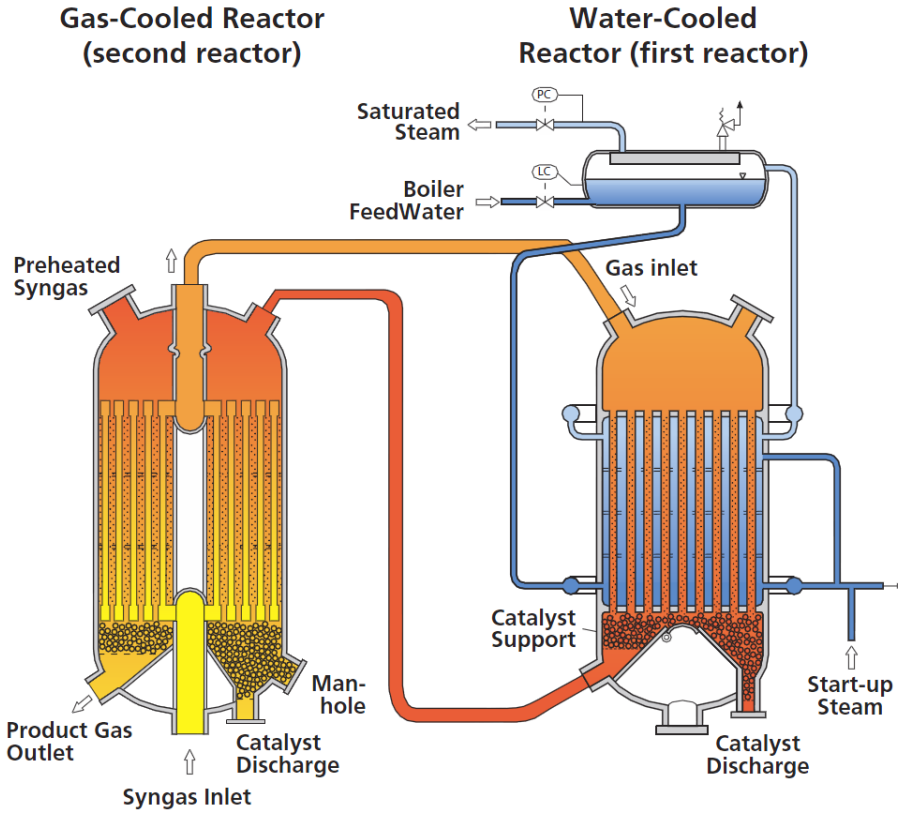

Figure 2.1: Lurgi MegaMethanol® process [38].

The highly exothermic reactions occurring during methanol synthesis make the removal of heat an essential issue for reactor design. In general, three different types of fixed-bed reactors are used for methanol synthesis, namely isothermal reactors through boiling water cooling, quench reactors and indirectly cooled reactors [18]. Since methanol synthesis is an equilibrium limited process, the synthesis gas is typically recycled. As an example, figure 2.1 shows the concept of the MegaMethanol® process by Lurgi [38]. In the first reactor, the heat of reaction is removed *via* boiling water, the temperature is controlled by the steam pressure. The catalyst is loaded in tubes and rests on a bed of an inert material. In order to allow high space velocities, the partly converted synthesis gas is routed to a second reactor, where it flows counter-currently to fresh and cold synthesis gas. As the temperature is lowered over the reactor length, the outlet concentration of methanol rises due to the thermodynamic equilibrium [38]. On

larger scale other concepts than fixed-bed reactors rarely exist [18]. Only slurry phase reactors, with the catalyst suspended in an inert oil were also considered, providing a better temperature control. However, the volume of such a reactor is larger and a lower conversion per pass due to high back mixing are main disadvantages of such reactors [18]. Only a few companies contribute to the worldwide methanol production capacity, among those ICI (about 61%), Lurgi (about 27%) and MGC (8%) [19].

2.1.2 The industrial catalyst

2.1.2.1 The nature of active sites

The industrial catalyst comprises of copper, zinc oxide and alumina. It is usually prepared by co-precipitation of salts such as nitrates of copper, zinc and aluminum. The basic precipitating agents are commonly carbonates, hydroxycarbonates or hydroxides of alkali metals [18].

The influence of each component on the activity during methanol synthesis is still under debate. Various studies indicate an almost linear relationship of the catalytic activity to the metallic copper area [39–42]. However, this might be only valid within the catalytic system used. Different intrinsic activities for binary copper alumina, copper zinc oxide and ternary catalysts were found (see also figure 2.2). Catalytic activity increases from Cu/Al_2O_3 to Cu/ZnO and finally $Cu/ZnO/Al_2O_3$.

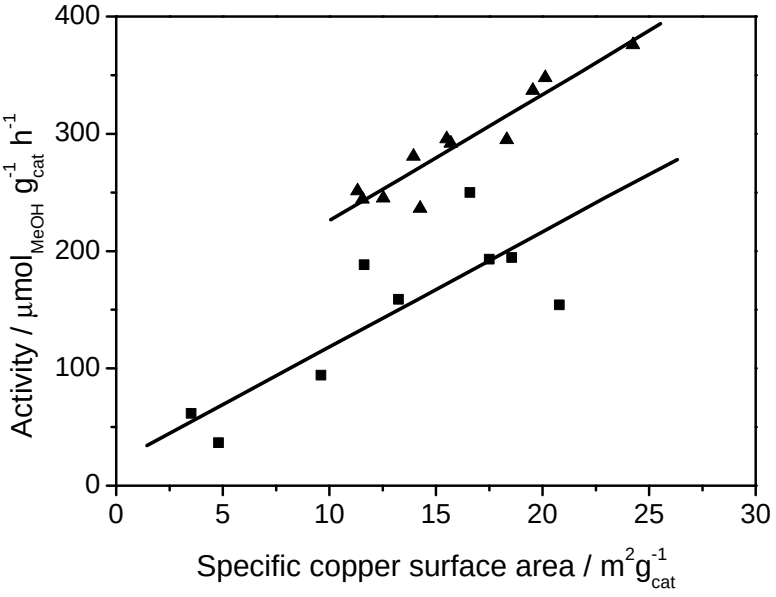

Figure 2.2: Intrinsic activity of binary copper zinc oxide (■) and ternary copper (▲) catalysts in methanol synthesis, adapted from [42].

The enhanced activity of alumina containing catalysts might be caused by increased copper concentrations in the support induced by the presence of alumina in the catalyst system [43]. However, it is generally accepted that the presence of alumina significantly enhances the catalysts thermal stability [43, 44]. A higher copper dispersion was discussed, resulting from an enrichment of Al at the catalysts surface [45].

The effect of zinc oxide is also still under debate. Zinc oxide itself exhibits very low activity for methanol synthesis under typical reaction conditions. The higher activities for ternary $Cu/ZnO/Al_2O_3$ catalysts than Cu/Al_2O_3 therefore supports synergy effects between copper and zinc oxide. A possible explanation for the enhanced methanol production rates may be hydrogen stored in the zinc oxide, which could further spillover to copper and enhance the hydrogenation of surface intermediates [46]. Zinc oxide microcrystallites may also stabilize strained copper particles, which was also correlated to the methanol synthesis activity [21, 22, 47].

Nakamura and co-workers [23, 48, 49] used H_2/CO_2 and H_2/CO as a feed gas over different catalysts, consisting of physical mixtures of Cu/SiO_2 and ZnO/SiO_2, Zn-containing Cu/SiO_2 and $(Zn)Cu/SiO_2$, which led to the conclusion that CO and CO_2 hydrogenation may proceed over different catalytic active sites.The catalytic active site for CO_2 hydrogenation is proposed to be a Cu-Zn alloy, created by Zn dissolved in the copper, while CO may be hydrogenated over Cu-O-Zn sites [23, 48–50]. The presence of a Cu-Zn alloy was also indicated by XRD measurements [50].

Besides the surface alloy model [23], another attempt to explain the synergy effect was introduced by the Topsøe group [24–27] in terms of strong metal-support interactions (SMSI), which may cause wetting of the copper particles under highly reducing conditions. Upon a treatment with reducing gases the copper particles supported on zinc oxide become more flat and spread over the ZnO surface, which finally leads to Cu-Zn alloying and brass formation at severe reducing conditions. This behavior, observed by *in-situ* extended X-ray absorption fine structure experiments, could also be verified by *in-situ* TEM measurements [28, 29]. Figure 2.3 shows the progress of dynamical changes as the reduction potential of the gaseous environment increases. The copper particles become disk like under reducing conditions (figure 2.3 b), whereas spherical particles are found under oxidizing conditions (figure 2.3 a). Figure 2.3 also illustrates Cu-Zn (c) and brass alloy (d) formation under most reducing conditions.

The dynamical behavior can be correlated to the Wulff construction, which will be revisited later in more detail (section 2.3). The SMSI effect may also explain the enhanced transient methanol synthesis activity for catalysts pre-treated with highly reducing gases [29, 34, 41].

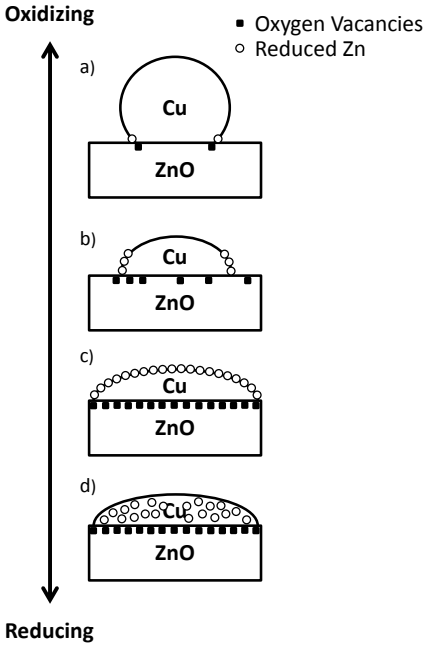

Figure 2.3: Dynamic catalyst behavior: wetting/non-wetting effect [24].

2.1.2.2 Deactivation

It is known that industrial methanol catalysts undergo a relatively fast deactivation during the first thousand hours of operation, which can be assigned to chemical poisoning or thermal sintering [35]. Even when there are no catalyst poisons present, the loss in activity may be around one third of the initial activity [28]. Sintering, i.e. a decrease in surface area due to agglomeration of copper particles, is mainly responsible for the loss in activity. Sintering describes the migration of atoms or crystals to larger agglomerates [30], which lowers the catalytic active surface area. This migration is a function of the mobility of such atoms and hence the Brownian motion, which means that sintering processes highly depend on the temperature. There are two different indicators how the atoms or crystals may agglomerate, the Hüttig and Tammann temperatures, both being dependent on the melting temperature of a component [18, 30, 51]. The Hüttig temperature is defined as:

$$T_{Hüttig} = 0.3 \cdot T_{melting} \tag{2.5}$$

and gives a temperature correlation to the movement of single atoms. For copper and zinc oxide, this temperature is 402 and 696 K, respectively [30]. The movement of whole agglomerates is described by the Tammann temperature according to:

$$T_{Tammann} = 0.5 \cdot T_{melting} \tag{2.6}$$

and is 670 K for copper and 1160 K for zinc oxide [30]. It is expected that neither copper nor zinc oxide sinters in considerable amounts, however, several experimental studies

show significant growth of copper crystal above temperatures of 543 K [35, 52]. Also sintering of ZnO was reported [35]. Sintering effects may be decreased by lowering the temperature, however, this will also influence the rate of methanol formation and hence the reactor performance. As stated above, the addition of alumina also increases the thermal stability of the catalyst system [44]. Another highly sensitive parameter on sintering of the catalyst is the water content in the reaction gas. Water can be formed *via* the reverse water-gas shift reaction or the methanol formation from carbon dioxide and enhances the formation of agglomerates [35]. Feed with a high content of carbon dioxide may also accelerate the catalyst aging, possible due to the increased formation of water by the reverse water-gas shift reaction [18, 30] or the strong adsorption of CO_2 [53]. Also syngas containing exclusively carbon monoxide and hydrogen without water or carbon dioxide showed irreversible deactivation, possibly due to an over-reduction of the catalyst [53]. Other explanations could be Zn evaporation or brass formation [18].

In literature, catalyst poisoning is mainly attributed to site blocking effects [18, 54]. Nowadays, sulfur poisoning is rarely a problem if the feedstock is derived from natural gas, however, if the synthesis gas is produced by gasification of coal or heavy oils, the active sites may be blocked by deposited sulfur originating from hydrogen sulfide [18, 54]. However, ZnO may act as a sulfur reservoir and hence decrease the sulfur poisoning process. Zinc oxide is hereby converted to zinc sulfide. However, even traces of chloride may deactivate the catalyst by site blocking and also enhance sintering effects. Zinc oxide may also be converted to $ZnCl_2$, which does not prevent the catalyst from poisoning, in contrast to ZnS [54]. Highly volatile $Fe(CO)_5$ or $Ni(CO)_4$, which can be solved from metal containing equipment, are transformed into their metals and further block active sites by metal deposition [18]. In case of the iron metal the poisoning effect can partly be described by the Fischer-Tropsch activity, which will produce high boiling waxes irreversible covering the catalysts surface [18].

2.1.3 Kinetics of methanol synthesis

Various general kinetic rate expressions for methanol synthesis (equations 2.1 - 2.3) have been published during the last decades [53, 55–59]. First, carbon monoxide was exclusively considered as carbon source [55, 56], even for synthesis gas containing carbon dioxide. However, it is not straightforward and still under debate to conclude how methanol is primarily formed [18], since carbon dioxide and carbon monoxide are not discriminable due to the water-gas shift reaction (equation 2.3). This means that a choice of either carbon monoxide or carbon dioxide as a primarily educt may be arbitrary, at least to some extent [60]. McNeil et al. [57], Klier et al. [53] and Graaf et al. [58] considered both carbon oxides as a source for methanol. Among the most used kinetic models in literature is the model by Graaf et al. [58], where carbon dioxide and monoxide adsorb on different active sites, compared to water and hydrogen. They formulated many different models based on stepwise hydrogenation of both carbon species and the water-gas shift reaction occuring *via* a formate mechanism, considering

different steps to be rate determining. Using statistical methods, final kinetic expressions with the best description of their experiments were derived. However, this approach simultaneously predicts two different concentrations for some surface intermediates, i.e. formyl and methoxy species [59]. Vanden Bussche and Froment [59] considered only the carbon dioxide hydrogenation for the formation of methanol, which is consistent with previously mentioned isotope labeling and pulse or step experiments [18, 32–34]. In their mechanism, adsorption of carbon dioxide leads to carbonate structures, which are further hydrogenated to yield methanol. The water-gas shift reaction occurs *via* a redox mechanism. All reactions, except the hydrogenation of formate and the carbon dioxide adsorption are in pseudo-equilibrium. The proposed mechanism is displayed in table 2.1, the derivation of the respective overall rate equations will be shown in the modeling section. All parameters were fitted to experimental data simultaneously, which implies that the physical significance of these parameters may be low.

Table 2.1: Model of methanol synthesis, according to Vanden Bussche and Froment [59].

Step	**Surface reactions**		
1	$H_{2(g)} + 2*$	$\rightleftharpoons$	$2\,H*$
2	$CO_{2(g)} + *$	$\rightleftharpoons$	$O* + CO_{(g)}$
3	$CO_{2(g)} + O* + *$	$\rightleftharpoons$	$CO_3 2*$
4	$CO_3 2* + H*$	$\rightleftharpoons$	$HCO_3 2* + *$
5	$HCO_3 2* + *$	$\rightleftharpoons$	$HCO_2 2* + O*$
6	$HCO_2 2* + H*$	$\rightleftharpoons$	$H_2CO_2 2* + *$
7	$H_2CO_2 2*$	$\rightleftharpoons$	$H_2CO* + O*$
8	$H_2CO* + H*$	$\rightleftharpoons$	$H_3CO* + *$
9	$H_3CO* + H*$	$\rightleftharpoons$	$CH_3OH_{(g)} + 2*$
10	$O* + H*$	$\rightleftharpoons$	$OH* + *$
11	$OH* + H*$	$\rightleftharpoons$	$H_2O* + *$
12	H_2O*	$\rightleftharpoons$	$H_2O_{(g)} + *$

However, the detailed kinetics of methanol synthesis is still under debate. As stated before, Askgaard et al. [10] were the first to propose a mechanistic model using a microkinetic approach, based on single crystal studies performed under UHV conditions. The microkinetic model has the advantage that all coverages of intermediates can be explicitly calculated, since no lumped parameters are used for the model formulation. Table 2.2 shows the proposed 16 equilibrium reactions, where methanol is believed to be formed by the hydrogenation of carbon dioxide.

In this mechanism, reactions 1-8 belong to the water-gas shift reaction, assuming a redox mechanism [10], similar to Vanden Bussche and Froment [59]. This mechanism was already proposed by Ovesen et al. [14] and was shown to be adequate under UHV as well

Table 2.2: Elementary reactions in methanol synthesis taken from Askgaard et al. [10].

Step	Surface reactions		
1	$H_2O_{(g)} + *$	$\rightleftharpoons$	H_2O*
2	$H_2O* + *$	$\rightleftharpoons$	$OH* + H*$
3	$2\,OH*$	$\rightleftharpoons$	$H_2O* + O*$
4	$OH* + *$	$\rightleftharpoons$	$O* + H*$
5	$2\,H*$	$\rightleftharpoons$	$H_{2(g)} + 2*$
6	$CO_{(g)} + *$	$\rightleftharpoons$	$CO*$
7	$CO* + O*$	$\rightleftharpoons$	$CO_2* + *$
8	CO_2*	$\rightleftharpoons$	$CO_{2(g)} + *$
9	$CO_2* + H*$	$\rightleftharpoons$	$HCOO* + *$
10	$HCOO* + H*$	$\rightleftharpoons$	$H_2COO* + *$
11	$H_2COO* + H*$	$\rightleftharpoons$	$H_3CO* + O*$
12	$H_3CO* + H*$	$\rightleftharpoons$	$CH_3OH* + *$
13	CH_3OH*	$\rightleftharpoons$	$CH_3OH_{(g)} + *$
14	$H_2COO* + *$	$\rightleftharpoons$	$HCHO* + O*$
15	$H_2COO* + H*$	$\rightleftharpoons$	$HCHO* + OH*$
16	$HCHO*$	$\rightleftharpoons$	$HCHO_{(g)} + *$

as under industrial conditions, when including the formation of formate as a "dead end" by blocking active sites [12]. Under methanol synthesis conditions, the selectivity towards formaldehyde is very low (steps 14-16), hence, for the microkinetic analysis by Askgaard et al. [10] these side reactions were omitted from further investigations. The successive hydrogenation of carbon dioxide further leads to methanol (steps 9-13), where steps 10, 11 or step 12 may be rate limiting [10]. Closer analysis revealed that an adequate description of single crystal experiments is best for considering step 11, the hydrogenation of H_2COO_{ads} to methoxide, as rate determining step. In the present model, adsorbate-adsorbate interactions are neglected. Equilibrium constants for all considered steps are calculated by the means of statistical thermodynamics, with data obtained from single crystal studies, except for the ground state energy of dioxymethylene and methoxide [18]. Besides the single crystal experiments, the model could be successfully extrapolated to industrial relevant conditions, measured by Graaf et al. [58]. However, systematic deviations at specific p_{CO}/p_{CO_2} ratios were found. At high ratios, the experimental values exceed the predicted ones, whereas at low ratios of the partial pressures the opposite observation can be made. Subsequently, Ovesen et al. [13] incorporated the dynamic behavior of copper on zinc oxide (see sections 2.1.2 and 2.3) into the microkinetic model. Together with an implementation of the structure

sensitivity over different copper low-index planes, most of the deviations could be eliminated.

Recently, Grabow and Mavrikakis [31] developed a new mechanistic model based on density functional calculations. In their calculations, the kinetics of the overall methanol synthesis could be re-produced using Cu(111) as active sites. Their calculations led to the conclusion that CO_2 hydrogenation is responsible for about 2/3 and CO hydrogenation for 1/3 of the methanol formed. The methanol synthesis rates are limited by the methoxy formation for low and the hydrogenation of such a methoxy species for feeds containing a high amount of CO_2. After fitting their DFT values to data from experiments by Graaf et al. [58], they suggest a more open Cu surface, e.g. Cu(110), Cu(100), and Cu(211), partially covered by oxygen as a better model for the active site. However, according to the authors synergy effects of copper and zinc oxide cannot be excluded and should not be neglected. Further research concerning the structure sensitivity is suggested [31]. Hence, in this thesis the model by Ovesen et al. [13] was further investigated for methanol synthesis, since this model comprises the above mentioned effects.

2.2 Thermodynamic and kinetic fundamentals

2.2.1 Thermodynamics

2.2.1.1 Statistical thermodynamic

Statistical thermodynamics of chemical reactions and chemisorptions can be very important for estimation of equilibrium constants or rate constants [7, 61]. Molecules usually have several degrees of freedom, i.e. translation, vibration, rotation and electronic. In order to calculate the partition function of a molecule, several assumptions have to be made, namely [7, 11]:

- thermal equilibrium
- no pairwise interaction energies between molecules
- indistinguishable molecules of the same chemical kind
- temperatures well above absolute zero
- all sites of a specific plane are identical
- only one molecule can adsorb on a site

The energy of a molecule is given by the sum of its (independent) degrees of freedom [61]:

$$\epsilon = \epsilon_t + \epsilon_v + \epsilon_r + \epsilon_e \tag{2.7}$$

where the indices denote the respective contributions.

Furthermore, the specific molecular partition function is simply the product of the degrees of freedom, when there is no interaction between the molecules [11]:

$$q = q_t \cdot q_v \cdot q_r \cdot q_e \tag{2.8}$$

In the following, the different contributions to the molecular partition function, as well as the calculation of the entropy, enthalpy and Gibbs energy shall be presented.

Translational energy

Usually one has to distinguish between the translational partition function of a gas and an adsorbed molecule. For gaseous molecules, the translational part is substantially dependent on the thermal wave length and hence the temperature, pressure and mass of the molecule (particle in a box) [62]:

$$q_t = \frac{k_B T}{p h^3} \cdot (2\pi m_i k_B T)^{\frac{3}{2}} \tag{2.9}$$

The translation of adsorbed molecules can be approximated by frustrated translation and is treated as vibrations, separated into frustrated translation parallel, frustrated translation orthogonal to the surface and frustrated rotational translation, when there is data available [10, 11]:

$$\begin{aligned} q_t = & \frac{\exp\left(-\frac{hc\omega_{ortho}}{2k_B T}\right)}{1-\exp\left(-\frac{hc\omega_{ortho}}{k_B T}\right)} \cdot \frac{\exp\left(-\frac{hc\omega_{para}}{k_B T}\right)}{\left(1-\exp\left(-\frac{hc\omega_{para}}{k_B T}\right)\right)^2} \\ & \cdot \frac{\exp\left(-\frac{3hc\omega_{rot}}{2k_B T}\right)}{\left(1-\exp\left(-\frac{hc\omega_{rot}}{k_B T}\right)\right)^3} \end{aligned} \tag{2.10}$$

Vibrational energy [61]

The vibrational partition function for all kind of molecules can be calculated by equation 2.11. Each vibrational degree of freedom, *no*, contributes to the vibrational partition function.

$$q_v = \prod_{i=1}^{no_{\psi_i}} \left(\frac{\exp\left(-\frac{\psi_i hc}{2k_B T}\right)}{1-\exp\left(-\frac{\psi_i hc}{k_B T}\right)} \right) \tag{2.11}$$

Rotational energy

The rotational partition function for linear molecules, i.e. carbon monoxide, can be calculated by:

$$q_r = \frac{1}{\sigma_i} \sum_{k=1}^{\infty} \left((2k+1) \cdot \exp\left(\frac{-k(k+1) B_i hc}{k_B T} \right) \right) \tag{2.12}$$

For most of the linear molecules, this equation can be simplified to [7]:

$$q_r = \frac{kT}{hcB_i} \cdot \frac{1}{\sigma_i}, \tag{2.13}$$

An exception is hydrogen, even for high temperatures, it has to be calculated by equation 2.12.

For asymmetric molecules, i.e. methanol, the following approximation is used [61]:

$$q_r = \frac{1}{\sigma_i} (\pi I_{abc})^{\frac{1}{2}} \cdot \left(\frac{k_B T 8\pi^2}{h^2} \right)^{\frac{3}{2}} \tag{2.14}$$

Ground state energy

The ground state partition function can be calculated by equation 2.15 [11]. The ground state energy is related to the stability of a molecule. It can be determined by temperature-programmed desorption experiments or from the enthalpy of formation.

$$q_e = \exp\left(\frac{-E_i}{RT} \right) \tag{2.15}$$

Finally, thermodynamic properties like the entropy, enthalpie and Gibbs energy can be calculated from the partition functions. For gas phase molecules, the entropy for a linear molecule is given by [63]:

$$\begin{aligned} S_i = R \Bigg\{ & \ln\left(\left(\frac{2\pi m_i k_B T}{h^2} \right)^{\frac{3}{2}} \cdot \frac{k_B T}{p} \cdot \exp(2.5) \right) \\ & + \ln\left(\frac{k_B T \exp(1)}{B_i c h \sigma_i} \right) \\ & + \sum_{i=1}^{no_{\psi_i}} \left(\frac{\frac{h\psi_i c}{k_B T}}{\exp\left(\frac{h\psi_i c}{k_B T}\right) - 1} - \ln\left(1 - \exp\left(\frac{-h\psi_i c}{k_B T}\right)\right) \right) + \ln(\omega_{e1}) \Bigg\} \end{aligned} \tag{2.16}$$

The entropy of an ideal polyatomic gas can be calculated according to [63]:

$$\begin{aligned} S_i = R \Bigg\{ & \ln\left(\left(\frac{2\pi m_i k_B T}{h^2} \right)^{\frac{3}{2}} \cdot \frac{k_B T}{p} \cdot \exp(2.5) \right) \\ & + \ln\left(\left(\frac{\pi^{\frac{1}{2}} \exp(1.5)}{\sigma_i} \right) \cdot \left(\frac{T^3 \cdot I_{abc}}{\left(\frac{h^2}{8\pi^2 k_B}\right)^3} \right)^{\frac{1}{2}} \right) \\ & + \sum_{i=1}^{no_{\psi_i}} \left(\frac{\frac{h\psi_i c}{k_B T}}{\exp\left(\frac{h\psi_i c}{k_B T}\right) - 1} - \ln\left(1 - \exp\left(\frac{-h\psi_i c}{k_B T}\right)\right) \right) + \ln(\omega_{e1}) \Bigg\} \end{aligned} \tag{2.17}$$

The entropy of adsorbed molecules can be calculated equally for linear and not linear cases and is determined by contributions from vibrations relative to the surface.

$$\begin{aligned} S_i = R\Bigg\{ & \sum_{i=1}^{no_{\psi_i}} \left(\frac{\frac{\psi_i hc}{k_B T}}{\exp\left(\frac{\psi_i hc}{k_B T}\right) - 1} - \ln\left(1 - \exp\left(\frac{-\psi_i hc}{k_B T}\right)\right)\right) \\ & + \sum_{l}^{no_{\omega_{ortho}}} \left(\frac{\frac{\omega_{ortho} hc}{k_B T}}{\exp\left(\frac{\omega_{ortho} hc}{k_B T}\right) - 1} - \ln\left(1 - \exp\left(-\frac{\omega_{ortho} hc}{k_B T}\right)\right)\right) \\ & + \sum_{m}^{no_{\omega_{para}}} \left(\frac{\frac{\omega_{para} hc}{k_B T}}{\exp\left(\frac{\omega_{para} hc}{k_B T}\right) - 1} - \ln\left(1 - \exp\left(-\frac{\omega_{para} hc}{k_B T}\right)\right)\right) \\ & + \sum_{n}^{no_{\omega_{rot}}} \left(\frac{\frac{\omega_{rot} hc}{k_B T}}{\exp\left(\frac{\omega_{rot} hc}{k_B T}\right) - 1} - \ln\left(1 - \exp\left(-\frac{\omega_{rot} hc}{k_B T}\right)\right)\right)\Bigg\} \end{aligned} \tag{2.18}$$

The Gibbs energy can easily calculated by the formula [7]:

$$G_i = -RT \cdot \ln(q_i) \tag{2.19}$$

Finally the enthalpy of a specific molecule is given by the relationship:

$$H_i = G_i + T \cdot S_i \tag{2.20}$$

In general, the Gibbs energy and the equilibrium constant of a reaction are related as:

$$K = \exp\left(-\Delta G / RT\right) \tag{2.21}$$

which can be re-arranged in terms of the molecular partition functions:

$$K = \prod q_i^{\nu_i} \tag{2.22}$$

2.2.1.2 Application to methanol synthesis

All thermodynamic data for a reaction mechanism can be calculated, when the specific input parameters for all species are known [10, 11, 13, 14]. Ovesen et al. [11, 14] determined the experimental and theoretical input for the statistical thermodynamic treatment of the water-gas shift reaction. Various experiments (i.e. High-Resolution Electron Energy Loss Spectroscopy, temperature-programmed desorption) were evaluated to calculate the thermodynamics of this important reaction. Later, Askgaard et al. [10] used this data to calculate the thermodynamics of the methanol synthesis. Using the elementary reactions in table 2.2, the enthalpy of formation as well as the entropy and Gibbs energy can be calculated [10], the corresponding input data is given in the Appendix.

As an example figure 2.4 shows the enthalpy of formation as well as the entropy for the methanol synthesis, evaluated for a pressure of 50 bar and a temperature of 525 K at a coverage of 0.5. It can be seen that the obtained values agree well with the fundamental thermodynamics of methanol synthesis, being an exothermic reaction with an overall loss in entropy due to the loss in volume.

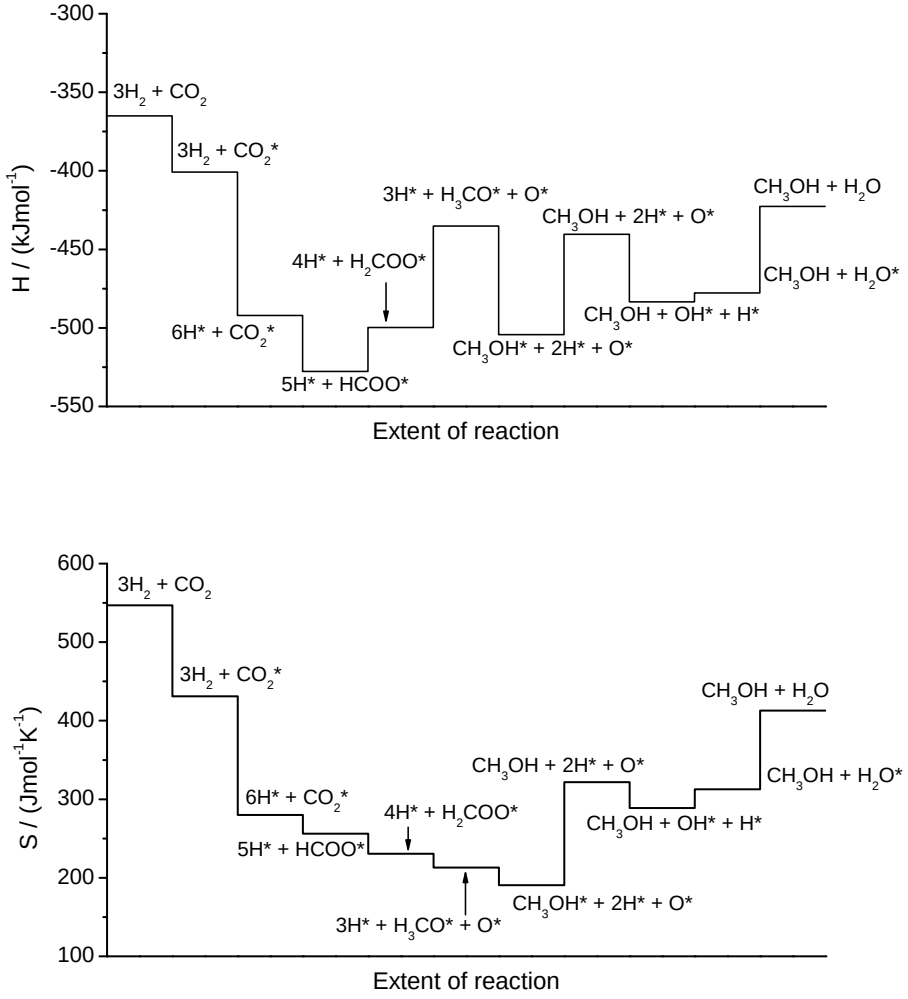

Figure 2.4: Enthalpy (top) and entropy (bottom) for the methanol synthesis, $p = 50\,\text{bar}$ and $T = 525\,\text{K}$, analogous to [10].

Furthermore, as described above all equilibrium constants can be calculated straightforward. As an example figure 2.5 shows the equilibrium mole fraction of methanol at different pressures and temperatures. It can clearly be seen that the methanol fraction increases with increasing pressure and decreasing temperature.

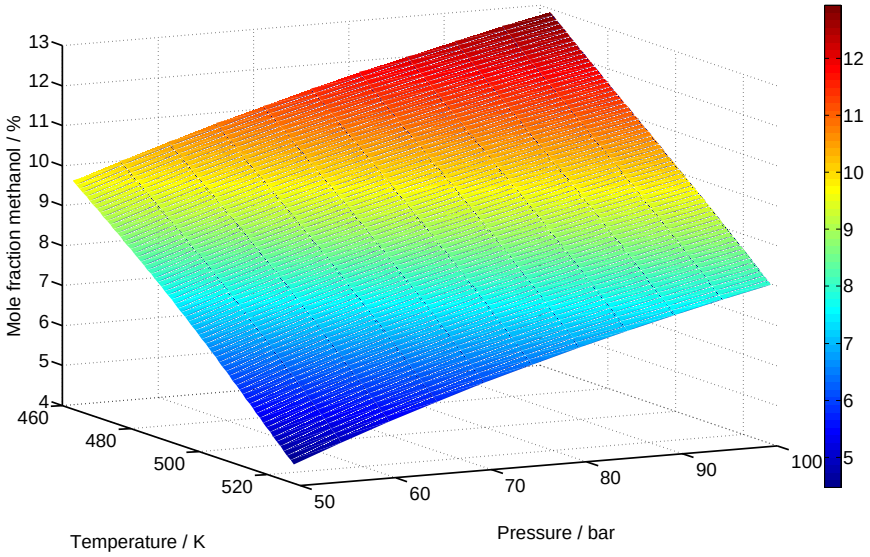

Figure 2.5: Equilibrium mole fraction of methanol for a feed consisting of 59.5% H_2, 8% CO_2, 6% CO and 26.5% inert.

2.2.2 Microkinetics

Usually heterogeneously catalyzed reactions can be described by Langmuir-Hinshelwood or Eley-Rideal kinetics. The latter describes the reaction of a chemisorbed molecule directly with a gas phase molecule. On the other hand a Langmuir-Hinshelwood mechanism implies that all species are adsorbed before reaction, which is mainly the case for such reactions [61].

Surface reactions

Considering an equilibrium elementary reaction of the adsorbed molecules A and B to yield C and D (i.e. step 11 in table 2.2):

$$\nu_A \mathrm{A}* + \nu_B \mathrm{B}* \underset{k_-}{\overset{k_+}{\rightleftharpoons}} \nu_C \mathrm{C}* + \nu_D \mathrm{D}* \tag{2.23}$$

where k_+ and k_- are the forward and reverse rate constants, respectively. The following relationship for the reaction rate is obtained:

$$r = k_+ [A*]^{\nu_A} [B*]^{\nu_B} - k_- [C*]^{\nu_C} [D*]^{\nu_D} \tag{2.24}$$

In here, [X$*$] represents the concentration of the surface species $X*$, which can also be normalized to the number of active sites and ν_i is the stoichiometric factor. Usually the temperature-dependent rate constants are calculated by an Arrhenius term:

$$k = A \cdot \exp\left(\frac{-E_a}{RT}\right) \tag{2.25}$$

where k has units in accordance with the Arrhenius coefficient A. The activation energy may further be dependent on sorption processes and hence coverages [61], which will be discussed later.

The equilibrium constant is given by the microscopic reversibility of the reaction or the surface concentrations:

$$K = \frac{k_+}{k_-} = \frac{[C*]^{\nu_C}[D*]^{\nu_D}}{[A*]^{\nu_A}[B*]^{\nu_B}} \tag{2.26}$$

According to equation 2.22 the equilibrium constants can also be calculated by partition functions.

Sorption processes

Besides surface reactions, ad- and desorption phenomena play an essential role during heterogeneously catalyzed processes. Such a reaction may look like (i.e. step 1 in table 2.2):

$$\mathrm{B} + * \underset{k_{des}}{\overset{k_{ads}}{\rightleftharpoons}} \mathrm{B}* \tag{2.27}$$

In the most simple case Langmuir assumptions are applied. This means it is assumed that only a monolayer of adsorbed species can be formed, the adsorption and desorption energy is independent of the coverage and the active sites are homogeneous. This may be valid when the coverage of species is small, i.e. under UHV conditions, however, when adsorbat-adsorbat interactions or surface heterogeneities cannot be neglected, sorption may become coverage-dependent, which can be expressed *via* coverage-dependent Arrhenius parameters (equation 2.25). The coverage-dependence can be described with many mathematical expressions, i.e. a linear, Temkin-type, or a logarithmic, Freundlich-type relationship.

The kinetics of adsorption processes can also be estimated by the collision theory. Usually used for gas phase processes, where the rate of reaction is based on the number of collisions between the molecules and the activation energy barrier, the rate of adsorption is somehow proportional to the number of collisions between the gas phase molecules and the surface, F_{coll} [2, 61]:

$$F_{coll} = \frac{p_i}{\sqrt{2\pi m_i k_B T}} \tag{2.28}$$

where the collision flux, given in $\mathrm{s^{-1}m^{-2}}$, is dependent on the partial pressure of the species p_i, its mass m_i and the temperature T. However, not every collision may lead to adsorption of the molecule, i.e. when an activation energy is needed or a specific orientation of the molecule is necessary. Furthermore, the number of uncovered sites may play an essential role. The probability for adsorption upon collision can be described by a sticking coefficient s [2]:

$$r_{ads} = F_{coll} \cdot s \tag{2.29}$$

The dependence on the activation energy and hence temperature can be described by the exponential term. Moreover, the sticking coefficient is a function of surface coverage and can further be described by the sticking coefficient on a clean surface, s_0:

$$s = s_0 f(\theta) \exp\left(\frac{-E_a}{RT}\right) \tag{2.30}$$

Hence the rate of adsorption finally equals:

$$r_{ads} = \frac{f(\theta) p_i}{\sqrt{2\pi m_i k_B T} d} \exp\left(\frac{-E_a}{RT}\right) \tag{2.31}$$

when the rate is furthermore related to the number of active sites per m^2, d, and has the unit s^{-1}. Assuming non activated adsorption and a sticking coefficient of unity yields the upper limit for the rate constant of adsorption:

$$k_{ads} = \frac{p_i}{\sqrt{2\pi m_i k_B T} d} \tag{2.32}$$

Coverage-dependence and apparent activation energies

When estimating activation energies, it should be noted that these activation energies may only represent apparent activation energies, since their values depend strongly on the conditions where they are determined [61]. Often, when the coverages of key intermediates are high, the apparent activation energy may be lower than the real activation energy, i.e. CO oxidation over oxygen pre-adsorbed copper catalysts [64]. The apparent activation energy can therefore be given by:

$$E_{a,app} = E_a + \Delta H_{ads} \tag{2.33}$$

Usually such an adsorption energy is negative, which means the apparent activation energy is lowered by the modulus of ΔH_{ads}, which may furthermore be coverage-dependent [65]. This effect can be explained by the resulting heat of adsorption, which may be directly accessible to overcome the energy barrier of the surface reaction, when adsorption takes place right next to an reactive intermediate. This effect is therefore coverage-dependent, since for the limit $\theta \to 0$ the probability of an educt adsorbing next to such a reactive intermediate becomes less. At low coverages, the adsorbed molecules have to diffuse over the surface in order to react. Hereby, the heat of adsorption is emitted and is no longer accessible for reaction. A general expression for a relationship of E_a and ΔH_{ads}, within the limit of $E_{a,app}$ and E_a, yields an effective activation energy:

$$E_{a,eff} = f(\theta) E_a \tag{2.34}$$

Different types of coverage-dependencies can be described by a equation introduced by Keskitalo et al. [66]:

$$f(\theta) = b + \frac{\ln(1+a) - \ln(\theta/\theta_{max} + a)}{\ln(1+a) - \ln(a)} \cdot (1-b) \tag{2.35}$$

in here b represents the minimum of the function at $\theta = \theta_{max}$ in the limits of $0 \leq \theta/\theta_{max} \leq 1$. The factor a determines the curvature of the function. Figure 2.6 displays the different types of dependencies realizable. For $\theta = 0$ the function reaches its maximum of one. For values of a greater than one, a linear relationship is obtained, i.e. Temkin-like. For values smaller than one, the bigger the coverage range were the function is almost constant. When a tends towards zero, a constant low value, b, is obtained, which therefore determines the minimum function value. For $b = 1$ a coverage-independent value of 1 is obtained, resulting in a Langmuir-type dependence [66].

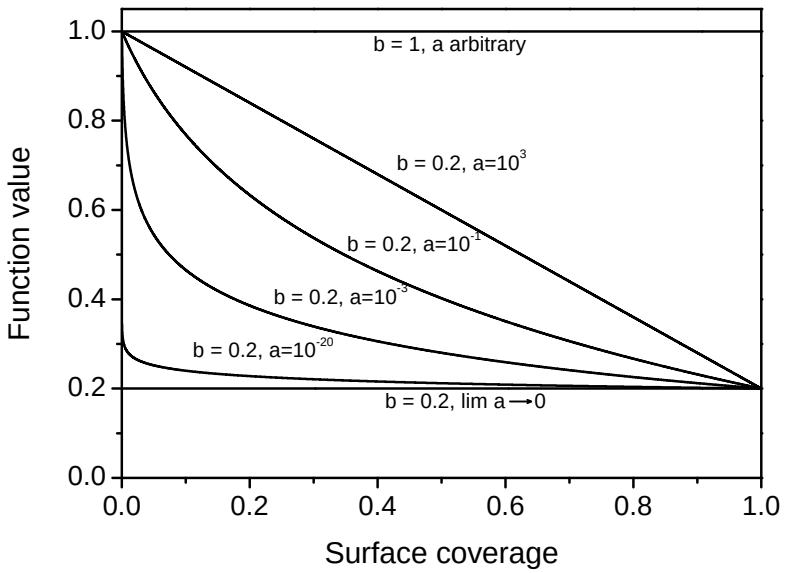

Figure 2.6: Logarithmic coverage-dependence [66], normalized to $E_a = 1$ and $\Delta H_{ads} = -0.8$.

Thermodynamic consistency

In microkinetic analysis thermodynamic consistency plays an essential role. Thermodynamic consistency is satisfied when an elementary step follows the relationships [1, 2, 67]:

$$E_{a,-} = E_{a,+} - \Delta H \tag{2.36}$$

and

$$A_- = A_+ \cdot \exp\left(-\frac{\Delta S}{R}\right) \tag{2.37}$$

These equations have to be satisfied for each reaction. For the net reaction, the overall consistency can be verified by [2, 67]:

$$\sum_i \sigma\left(E_{a,i,+}\right)) - \sum_i \sigma\left(E_{a,i,-}\right) = \Delta H_{net} \tag{2.38}$$

Which corresponds to the condition that the sum of the activation energies of all independent reaction paths in a mechanism must equal the heat of the net reaction [2]. In here, σ is the stoichiometric number of an elementary step. Furthermore, the products of the Arrhenius factors of all independent reactions paths are related to the overall entropy change by [2]:

$$\prod_i \left(\frac{A_{i,-}}{A_{i,+}}\right)^{\sigma_i} = \exp\left(-\frac{\Delta S_{net}}{T}\right) \tag{2.39}$$

2.3 Dynamics of copper on zinc oxide

As mentioned in section 2.1.2, experimental studies concerning dynamical changes of the copper attached to zinc oxide have been performed in great detail by the Topsøe group [24, 25, 28, 29]. *In-situ* methods, such as extended X-ray adsorption fine structure (EXAFS) and transmission electron measurements (TEM) revealed a reversible dynamic behavior. As an example figure 2.7 shows the TEM images recorded by Hansen et al. [28] of the equilibrated shapes of Cu/ZnO and the corresponding Wulff construction of the copper nanocrystals at different gas atmospheres.

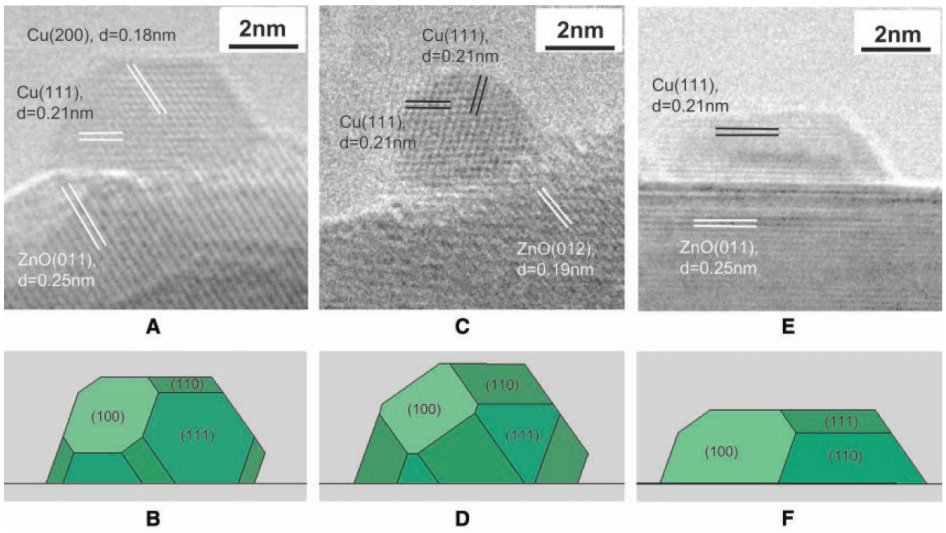

Figure 2.7: TEM images of a Cu/ZnO catalyst at different gas atmospheres (A, C, E) and corresponding Wulff construction of the copper particle (B, D, F), taken from [28].

It can clearly be seen that the shapes change remarkably, suggesting dynamical morphology changes of the catalyst. Changing the atmosphere from pure hydrogen (A) to a more oxidizing environment by the addition of water (C), the particle becomes

more spherical. Upon a combined treatment of hydrogen and carbon monoxide, which is more reducing than hydrogen itself, the particle shows remarkable flattening (E). The corresponding Wulff constructions are in good agreement with the obtained TEM images of the copper particles.

2.3.1 Wulff construction

In order to account for the above mentioned effects, the shape and plane distribution of the copper particles have to be determined for several gas environments. A relatively simple and straightforward way is the usage of the Wulff construction [25]. The shape of a crystal will always be defined by the minimization of the surface free energy [68]. Hereby, the sum of the surface free energies of all crystal planes gives the surface free energy of the crystal. The surface free energy of a crystal plane is proportional to the distance of the surface normal to the center of the epitaxy [68]:

$$\gamma_{hkl} \sim n_{hkl} \tag{2.40}$$

Hence, the shape of a crystal can be obtained by the Wulff construction, when the surface normal in equation 2.40 generates a plane and the intersecting lines of each plane build the crystals edges. A plane far away from the center of the epitaxy is therefore a plane with a high surface free energy and has the lowest fraction of the overall surface area, since the intersecting lines with the low energy planes determine its extent. Thus, when these free energies of the different crystal low-index planes are known, the shape and distribution of such planes can be calculated straightforward. The surface free energies of the low-index planes under vacuum were calculated by Vitos et al. [69]. Later, Hansen et al. [28] measured these energies *via in-situ* TEM experiments for different gas atmospheres at a pressure of 1.5 mbar. Table 2.3 lists the surface free energies relative to Cu(111), determined by Hansen et al. [28] in a hydrogen atmosphere, which are very close to the values published by Vitos et al. [69] under vacuum conditions.

Table 2.3: Relative surface free energies in a hydrogen atmosphere at 1.5 mbar [28].

Crystal plane	**Relative surface free energy**
Cu(100):	1.08 ± 0.03
Cu(110):	1.11 ± 0.02
Cu(111):	1.00

The structure of a free copper particle can now be calculated, using the program WinXMorph [70, 71]. Input parameters are the length of the surface normals as well as the symmetry of the crystal. The symmetry of the face-centered cubic (*fcc*) copper particle is described by the $Fm\bar{3}m$ space group. As a results one gets the distribution of the different surface planes and the volume of the crystal. In order to describe a copper

particle bound to zinc oxide, for the plane attached to the substrate the value for the surface free energy of the interacting components has to be assigned. Clausen et al. [25] introduced the term γ/γ_0 as contact surface free energy relative to the free energy of the clean surface γ_0. Hereby, γ can be described as the difference of the interface energy and the surface energy of the substrate $\gamma_{interface} - \gamma_{substrate}$ [25]. Upon variation of the surface normal perpendicular to the plane attached to the substrate, all shape characteristics of the crystal can be described. The following limiting behavior can be found:

$$-1 \leq \frac{\gamma}{\gamma_0} \leq 1 \tag{2.41}$$

In the limiting case of $\gamma/\gamma_0 = -1$ a degenerated two dimensional surface is obtained, which corresponds to the most reducing conditions. The distance of the surface normal, perpendicular to the zinc oxide, to the center of the epitaxy is hereby negative, which means that it points in the same direction as the surface normal of the plane on the opposite side of the crystal. Hence, the modulus of the distance to the center of the epitaxy of these two planes is equal, the symmetrical copper crystal degenerates into a two dimensional monolayer of copper atoms. On the other hand, when the contact surface free energy equals 1 the shape of the free crystal is obtained. All other crystal shapes can be obtained by varying γ/γ_0 in its domain according to equation 2.41. The length of the surface normals are adjusted, while keeping the overall volume of the crystal constant. Since WinXMorph does not comprise such an approach, the problem can only be solved iteratively. Such an approach yields a correlation of the overall surface of the respective crystal plane of the copper particle as well as γ/γ_0, which corresponds to the dependence of the crystal structure on the gas environment.

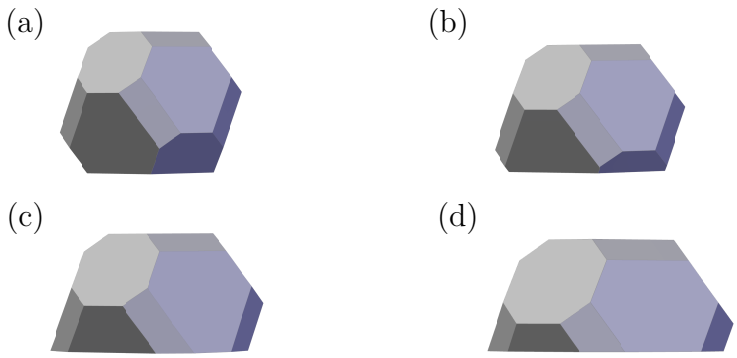

Figure 2.8: Equilibrium shape of a copper particle at different values for γ/γ_0, based on [25]:
(a) $\gamma/\gamma_0 = 0.75$ (b) $\gamma/\gamma_0 = 0.50$
(c) $\gamma/\gamma_0 = 0.25$ (d) $\gamma/\gamma_0 = 0.00$

Figure 2.8 illustrates the change of the particle morphology due to different values of γ/γ_0, visualized using WinXMorph. The total surface area and hence the total number of active sites is not constant when varying γ/γ_0. In this example, the particle is bound

via a Cu(111) surface plane, with a varying distance to the center of the epitaxy for different contact surface free energies. In order to keep the total volume of the particle constant, the surface normals of the unbound planes have to be adjusted. Their surface free energy is constant for a change in the contact surface free energy, which means the surface normals of all unbound planes become greater in the same dimension, according to equation 2.40. As a result the crystal structure of the unbound planes in figure 2.8 remains unchanged. Theoretically, the crystal grows or shrinks, however, the plane bound to the substrate cuts off the crystal, which leads to a constant volume. Copper particles comprising negative values of γ/γ_0 cannot be described by WinXMorph, since the center of the epitaxy is outside the crystal for these conditions. This limitation can be circumvented by the subtraction of a free crystal from a second, which is generated by the positive value of the desired γ/γ_0 ratio.

The results for this approach are depicted in figure 2.9, where the dimensionless surface areas are plotted against γ/γ_0. The graphs are similar to the ones published by Clausen et al. [25] and Ovesen et al. [13], minor differences may be caused by the choice of the surface free energies. Figure 2.9 shows that the total surface of the copper crystal rises asymptotically when γ/γ_0 tends towards -1, which is consistent with the limiting case of a two-dimensional crystal. For extreme reducing conditions, when γ/γ_0 tends towards -1, the area of the surface plane attached to the substrate is dominant. When a copper (111) plane is attached to the substrate, the surface area of these planes is always the highest, for a copper (110) plane attached to the zinc oxide the area of Cu(111) becomes dominant for a relative surface free energy above -0.92.

2.3.2 Correlation of gas phase reduction potential and catalyst morphology

Ovesen et al. [13] correlated the reduction potential of the gas phase with the catalysts morphology, based on the assumption that the concentration of oxygen vacancies at the Zn-O-Cu interface is determined by the following equations:

$$\mathrm{H_{2(g)}} + \mathrm{Zn{-}O{-}Cu} \rightleftharpoons \mathrm{H_2O_{(g)}} + \mathrm{Zn - [\ ] - Cu} \tag{2.42}$$

$$\mathrm{CO_{(g)}} + \mathrm{Zn{-}O{-}Cu} \rightleftharpoons \mathrm{CO_{2(g)}} + \mathrm{Zn - [\ ] - Cu} \tag{2.43}$$

The corresponding equilibrium term reads:

$$K_1 = \frac{p_{H_2O} \cdot [\mathrm{Zn - [\ ] - Cu}]}{p_{H_2} \cdot [\mathrm{Zn{-}O{-}Cu}]} \tag{2.44}$$

and

$$K_2 = \frac{p_{CO_2} \cdot [\mathrm{Zn - [\ ] - Cu}]}{p_{CO} \cdot [\mathrm{Zn{-}O{-}Cu}]} \tag{2.45}$$

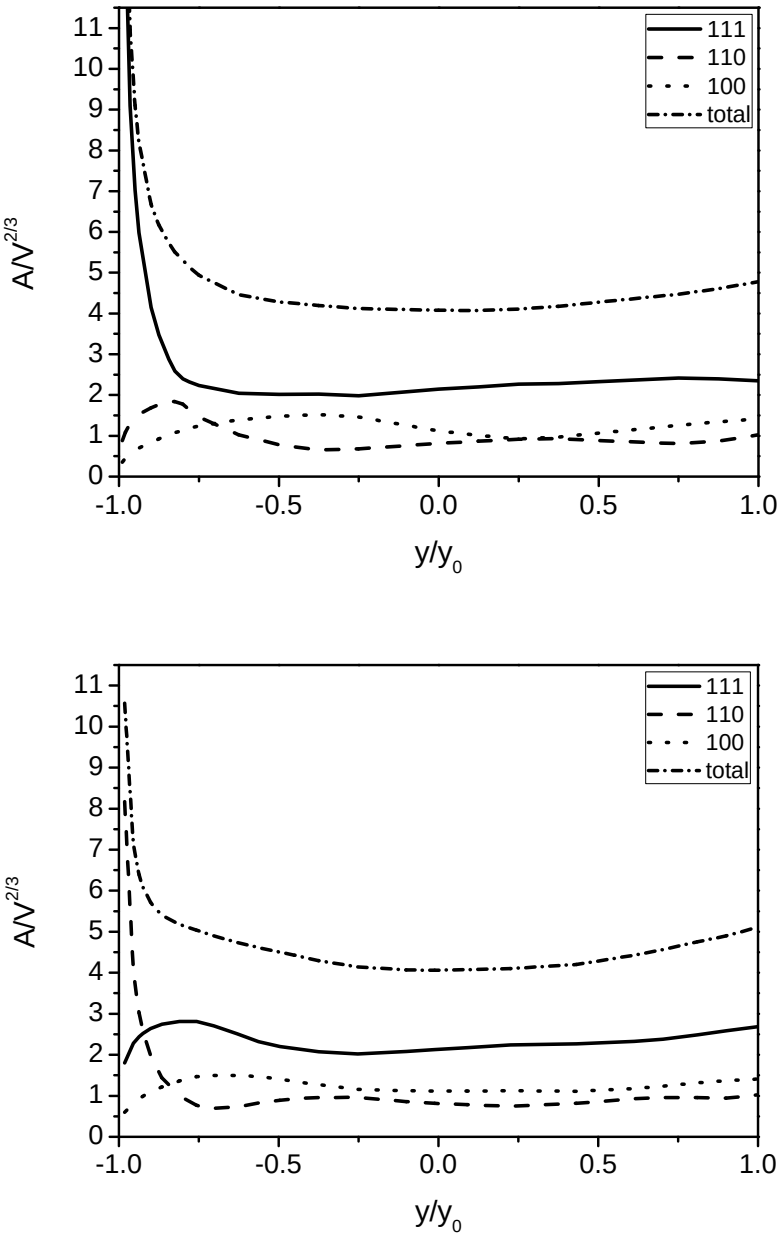

Figure 2.9: Dimensionless surface area $A/V^{2/3}$ vs. γ/γ_0, assuming that one of the Cu(111) planes is attached to the substrate (top) and one of the Cu(110) planes is attached to the substrate (bottom).

which can be coupled by:

$$[\text{Zn–O–Cu}] = 1 - [\text{Zn} - [\ ] - \text{Cu}] \tag{2.46}$$

Furthermore, assuming a linear relationship between the reduction potential of the gas phase and the relative contact surface free energy leads to [13]:

$$[\text{Zn} - [\ ] - \text{Cu}] = (1 - \gamma/\gamma_0)/2 \tag{2.47}$$

Finally coupling equations 2.44 to 2.47 gives:

$$\frac{\gamma}{\gamma_0} = \frac{1 - \sqrt{(K_1 \cdot \frac{p_{H_2}}{p_{H_2 0}}) \cdot (K_2 \cdot \frac{p_{CO}}{p_{CO_2}})}}{1 + \sqrt{(K_1 \cdot \frac{p_{H_2}}{p_{H_2 0}}) \cdot (K_2 \cdot \frac{p_{CO}}{p_{CO_2}})}} \tag{2.48}$$

In this equation, K_i corresponds to the equilibrium terms for the formation of oxygen vacancies by H_2 and CO, respectively. These terms can be calculated from the Gibbs free energy of the formation of oxygen vacancies in the Zn-O-Cu interface [13]:

$$K_i = \exp\left(\frac{\Delta G_i}{R \cdot T}\right) \qquad i = 1, 2 \tag{2.49}$$

Recently, Vesborg et al. [29] determined the distances of the surface normals to the epitaxy and hence were able to extract the Gibbs free energies. Hereby, G_1 was determined to yield 4.9 kJ·mol^{-1} and G_2 -1.1 kJ·mol^{-1}, respectively. Based on this results, the parameter γ/γ_0 can be determined for a given gas composition. Typical methanol synthesis gas does not comprise water, however the gas purity can be used as a good approximation. The total number of active sites N_{total} can be derived by the following relationship [13]:

$$N_{total} = N_{ini} \cdot \frac{\sum f_{hkl}\,(\gamma/\gamma_0) \cdot D_{hkl}}{\sum f_{hkl}\,((\gamma/\gamma_0)_{ini}) \cdot D_{hkl}} \tag{2.50}$$

where f_{hkl} is the surface area at a specific γ/γ_0 taken from figure 2.9, D_i the site density from table 2.4 and N_{ini} the number of active sites at fixed initial conditions $(\gamma/\gamma_0)_{ini}$. The fraction of Cu(100), η, and Cu(110), ϵ, can be derived as a function of f, yielding for Cu(100) [13]:

$$\eta = \frac{f_{100}\,(\gamma/\gamma_0) \cdot D_{100}}{\sum f_{hkl}\,(\gamma/\gamma_0) \cdot D_{hkl}} \tag{2.51}$$

and

$$\epsilon = \frac{f_{110}\,(\gamma/\gamma_0) \cdot D_{110}}{\sum f_{hkl}\,(\gamma/\gamma_0) \cdot D_{hkl}} \tag{2.52}$$

respectively.

From the conservation of active sites, the fraction of Cu(111), ζ, exposed on the catalyst can be derived as:

$$\zeta = 1 - \eta - \epsilon \tag{2.53}$$

Table 2.4: Site densities of specific copper planes.

Plane	Surface fraction
D_{111}	$\frac{\pi}{2\cdot\sqrt{3}}$
D_{110}	$\frac{\pi}{4\cdot\sqrt{2}}$
D_{100}	$\frac{\pi}{4}$

In order to account for the morphology changes during reaction, the curves in figure 2.8 can be approximated by polynomials and directly implemented into the corresponding modeling equations. When modeling transient processes, i.e. catalyst deactivation, the change in surface area and active site distribution with time has to be accounted for. The change in surface distributions lead to changing coverages on the specific low-index planes. As the mass conservation has to be satisfied, ratios of the different planes are only added or subtracted from uncovered sites. The shortly changed relative coverages are irrelevant in the following calculations, as the equilibrium between gas phase and coverages is regained within seconds *via* the kinetic equations. In the following, the governing equations for $N(t)$ is derived, exemplary for Cu(100), η. The number of covered and uncovered sites can be calculated as a function of time:

$$N_{free\,(t+\Delta t)} = N_{free\,(t)} + N_{total} \cdot \left(\eta_{(t+\Delta t)} - \eta_{(t)}\right) \tag{2.54}$$

$$N_{ads\,(t+\Delta t)} = N_{ads\,(t)} \tag{2.55}$$

Extending equations 2.54 and 2.55 by $\eta_{(t)}/\eta_{(t)}$ and dividing them by $N_{total} \cdot \eta_{(t+\Delta t)}$ yields:

$$\frac{N_{free\,(t+\Delta t)}}{N_{total} \cdot \eta_{(t+\Delta t)}} = \frac{N_{free\,(t)}}{N_{total} \cdot \eta_{(t+\Delta t)}} \cdot \frac{\eta_{(t)}}{\eta_{(t)}} + \frac{N_{total} \cdot \left(\eta_{(t+\Delta t)} - \eta_{(t)}\right)}{N_{total} \cdot \eta_{(t+\Delta t)}} \tag{2.56}$$

$$\frac{N_{ads\,(t+\Delta t)}}{N_{total} \cdot \eta_{(t+\Delta t)}} = \frac{N_{ads\,(t)}}{N_{total} \cdot \eta_{(t+\Delta t)}} \cdot \frac{\eta_{(t)}}{\eta_{(t)}} \tag{2.57}$$

Finally, as $\theta_{free}\,(t)$ equals $N_{free}/N_{total} \cdot \eta\,(t)$ and equally $\theta_{ads}\,(t)$ equals $N_{ads}/N_{total} \cdot \eta\,(t)$, one obtaines:

$$\theta_{free\,(t+\Delta t)} = \theta_{free\,(t)} \cdot \frac{\eta_{(t)}}{\eta_{(t+\Delta t)}} + \frac{\eta_{(t+\Delta t)} - \eta_{(t)}}{\eta_{(t+\Delta t)}} \tag{2.58}$$

$$\theta_{ads\,(t+\Delta t)} = \theta_{ads\,(t)} \cdot \frac{\eta_{(t)}}{\eta_{(t+\Delta t)}} \tag{2.59}$$

Equation 2.58 describes the coverage of free sites on Cu(100), when η changes, where the second term describes the increase or decrease of the coverage of free sites. The relationship of the coverage of adsorbates on Cu(100) with varying total number of active sites is described by equation 2.59. For Cu(110), ϵ, an analogous derivation, substituting η with ϵ, can be derived. Equation 2.50 gives the actual total number of actives sites at a specific gas composition. Furthermore equations 2.51 and 2.52 give the corresponding ratios of active sites. Finally the new coverages at $t = (t + \Delta t)$ can be calculated according to equations 2.58 and 2.59.

2.4 Modeling

In this thesis, two different mathematical programs are used to handle the differential equations and for optimization issues. MATLAB®, a script based numerical computing environment by MathWorks Inc. [72], is an interpreted language. Its key features are matrix operations and efficient built-in solvers. The standard program can be expanded by numerous toolboxes specially designed for various problems in science and engineering. Besides, the Athena Visual Studio engineering software is used [73]. Athena Visual Studio is particularly designed for chemical engineering issues, i.e. optimization and parameter estimations. It is, in contrast to MATLAB® a compiled programming language, based on FORTRAN. There are two steps to create results. First, the source code is compiled to yield a general machine code. In a second step the program is invoked, the input parameters for the machine code are specified, the machine code is run and hence the results are obtained. An interpreted language can be invoked in one step. There is no need to translate the source code into a machine code, the commands in the script are directly called during the runtime of the program by an interpreter. Hence, in MATLAB® the program code is called line by line, whereas Athena first transforms the code into a FORTRAN code, which is subsequently compiled and run. This machine code may be more efficient in computation time. However, often it is more convenient and clearer when the programs are based on scripts, which can be separated into different files. Athena requires well defined sequences during program development in order to transform the code into FORTRAN. Athena Visual Studio comprises several methods for discretization of partial differential equation, i.e. finite differences or orthogonal collocation. Using MATLAB®, the discretization has to be done by hand, i.e. by the methods of lines [74].

2.4.1 Discretization

This section deals with finite differences for discretization of partial differential equations [75]. A general partial differential equation in chemical engineering may be written as:

$$\frac{\partial c}{\partial t} = \frac{1}{z}\frac{\partial c}{\partial z} + \frac{\partial^2 c}{\partial z^2} \tag{2.60}$$

The key to solve this kind of differential equation is to divide the dimensions, i.e. time t and space z, in infinitesimal small segments to solve the given equation. Figure 2.10 shows a discretization for space and time:

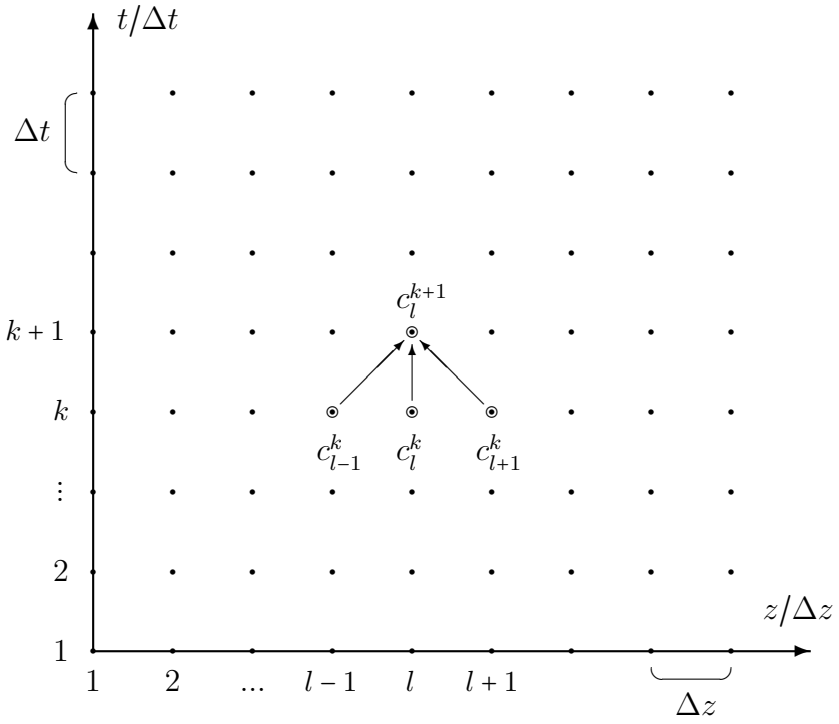

Figure 2.10: Discretization of time t and space z and exemplary the dependence of one point of data from the previous (time) step, adapted from [75].

Each value of z in equation 2.60 at a specific point l in such a coordinate system can be calculated as

$$z = (l-1)\Delta z \tag{2.61}$$

or

$$z = (l-0.5)\Delta z \tag{2.62}$$

when the origin of the coordinate system is centered between two points. Hence, the derivatives in equation 2.60 can be approximated after discretization. The known values of the previous integration step yield the difference quotients, usually given by the two points around the considered value and the value itself. Now it is straightforward to calculate the first order derivative of the space z, under the assumption of a constant, infinitesimal small Δz:

$$\left(\frac{\partial c}{\partial z}\right)_{FDQ} \approx \frac{c_{l+1} - c_l}{\Delta z} \tag{2.63}$$

$$\left(\frac{\partial c}{\partial z}\right)_{BDQ} \approx \frac{c_l - c_{l-1}}{\Delta z} \tag{2.64}$$

$$\left(\frac{\partial c}{\partial z}\right)_{CDQ} \approx \frac{c_{l+1} - c_{l-1}}{2\Delta z} \tag{2.65}$$

These equations comprise the three values of a time step k in figure 2.10. Equation 2.63 is named forward difference quotient (FDQ), equation 2.64 backward difference quotient (BDQ) and equation 2.65 is called central difference quotient (CDQ). The latter comprises a very high accuracy in approximation of the differences, hence, when suitable boundary conditions are given this method should be chosen. When a suitable amount of points and thus more computational time is expended, all approximations approach the real behavior of the curve. In case of central differences this will become valid for less points. The method for approximation of the second order derivatives is very similar:

$$\left(\frac{\partial^2 c}{\partial z^2}\right)_{FDQ} \approx \frac{c_{l+2} - 2c_{l+1} + c_l}{\Delta z^2} \tag{2.66}$$

$$\left(\frac{\partial^2 c}{\partial z^2}\right)_{BDQ} \approx \frac{c_l - 2c_{l-1} + c_{l-2}}{\Delta z^2} \tag{2.67}$$

$$\left(\frac{\partial^2 c}{\partial z^2}\right)_{CDQ} \approx \frac{c_{l+1} - 2c_l + c_{l-1}}{\Delta z^2} \tag{2.68}$$

Finally equation 2.60 can be approximated, i.e. by central differences:

$$\frac{\partial c}{\partial t} = \frac{1}{(l-1)\Delta z}\frac{c_{l+1} - c_{l-1}}{2\Delta z} + \frac{c_{l+1} - 2c_l + c_{l-1}}{\Delta z^2} \tag{2.69}$$

There exist several methods to solve the resulting differential equation, i.e. a direct method where all dimensions are discretized. However, this method may become unstable and oscillatory for certain ratios of Δz and Δt. Therefore the method of lines [74] was used to solve the governing equations. All dimensions except one where only first order derivatives occur are discretized according to the method described above. The resulting ordinary differential equation can simply be solved by a mathematical algorithm, i.e. a Runge-Kutta method. Such a method is implemented in MATLAB®'s "ode15s" solver for stiff ordinary differential equations. The equation is solved for all points of the discretization grid at each integration step. Figure 2.10 illustrates this procedure, for the calculation of c_l^{k+1} the values of c_{l-1}^k, c_l^k and c_{l+1}^k from the former integration step are evaluated. Integration of equation 2.69 with respect to the time yields the new values. This method has several advantages, i.e. a clear programming structure, high efficiency and flexibility of the solver. Relative and absolute tolerances can be specified, the solver comprises an adaptive method, which uses different increments for each integration step depending on the gradient.

As mentioned before, for solving partial differential equations boundary constraints have to be specified. Depending on the differential equation different information is needed to solve the given system. In the following, parabolic differential equations

are considered as typical problems like heat transfer or diffusional effects are treated *via* such kind of equations. These kind of systems are called initial or boundary value problems. First, all initial values at $t_0 = 0\,\mathrm{s}$ must be given. Usually this vector is known and can be specified for the initialization. Moreover, space boundaries have to be specified for the whole range of the considered time interval. The value of c_{l-1}^k is needed to calculate c_l^{k+1}, which may be outside of the discretization grid for $l = 1$. In order to avoid this problem, the boundaries are specified *via* different constraints. These boundaries can be separated into three different cases [76]. A boundary condition of the first kind, called Dirichlet condition, in terms of concentration is given by:

$$c_{z=0} = c_0 \tag{2.70}$$

A Neumann condition, or boundary condition of the second kind in the case of a given flux can be expressed *via* equation 2.71:

$$\frac{\partial c}{\partial z}\Big|_{z=0} = g(t) \tag{2.71}$$

Finally, a combination of 2.70 and 2.71 yields the Robin condition, also called boundary condition of the third kind, i.e. when a flux is defined in terms of a mass transfer coefficient with a known concentration, analogous to heat transfer problems [76].

For Dirichlet boundary conditions, a value is given at the boundary $l = 1$, which can be variable. Hereby, it is possible to calculate $c_{l=2}^{k+1}$ by using the known concentrations $c_{l=1}^k$, $c_{l=2}^k$ and $c_{l=3}^k$. Thus, the grid is chosen that the boundaries are located at a grid line [75]. When using the Neumann boundary condition, a derivative is given at the boundary value. In this case, the grid has to be chosen that the boundary lies in between two discretization points [75], which introduces values outside the grid. In order to eliminate the value outside the grid for $l = 1$, equation 2.71 can be discretized by backward differences:

$$\frac{\partial c}{\partial z}\Big|_{z=0} \approx \frac{c_l^k - c_{l-1}^k}{\Delta z} \tag{2.72}$$

Finally, the value of c_{l-1} is given by:

$$c_{l-1}^k = c_l^k - g(t) \cdot \Delta z \tag{2.73}$$

Coupling equation 2.69 and 2.73 at $l = 1$ eliminates the unknown value outside the grid. Right boundary conditions can be implemented straightforward. When boundaries at the left or right side are unknown, first order derivatives can be calculated using forward or backward differences, which do not require both boundary conditions.

2.4.2 Kinetics of methanol synthesis

In this thesis several models are used to describe the kinetics of methanol synthesis, namely the microkinetic models by Askgaard et al. [10] and Ovesen et al. [13] as well as two global kinetic models, a straightforward power law approach and a Langmuir-Hinshelwood-Hougen-Watson approach, adapted from Vanden Bussche and Froment [59]. Subsequently, the mechanistical models are discussed.

2.4.2.1 Microkinetic model

For a microkinetic model according to table 2.2 a general form for a plug-flow reactor on molar basis can be written as (see also 2.123):

$$\frac{\partial n_i}{\partial t} = R_i \cdot N_{total} - \frac{\partial \dot{n}_i}{\partial z} \qquad i = 1, \ldots, 5 \tag{2.74}$$

$$\frac{d\theta_{i_{111}}}{dt} = \sum_{j=1}^{13} \lambda_{ij} \cdot r_{j_{111}} \qquad i = 6, \ldots, 16 \tag{2.75}$$

$$\frac{d\theta_{i_{110}}}{dt} = \sum_{j=1}^{13} \lambda_{ij} \cdot r_{j_{110}} \qquad i = 17, \ldots, 27 \tag{2.76}$$

$$\frac{d\theta_{i_{100}}}{dt} = \sum_{j=1}^{13} \lambda_{ij} \cdot r_{j_{100}} \qquad i = 28, \ldots, 38 \tag{2.77}$$

$$\frac{\partial n_{Inert}}{\partial t} = -\frac{\partial \dot{n}_{Inert}}{\partial z} \tag{2.78}$$

In here, the general component balances for CO, CO_2, H_2O, H_2, CH_3OH and an inert are given by equations 2.74 and 2.78, respectively. The total number of active sites, N_{total}, can be calculated by equation 2.50. The overall rate R_i for a specific compound is a contribution from each considered surface plane, i.e. [13]:

$$R_i = (1 - \eta - \epsilon) \cdot \sum_{j=1}^{13} \lambda_{ij} \cdot r_{j_{111}} + \epsilon \cdot \sum_{j=1}^{13} \lambda_{ij} \cdot r_{j_{110}} + \eta \cdot \sum_{j=1}^{13} \lambda_{ij} \cdot r_{j_{100}} \tag{2.79}$$

The dimensionless surface concentrations for Cu(111), Cu(110) and Cu(100) are given by equations 2.75 - 2.77. The corresponding rate equations for the surface reactions, according to table 2.2 following the Langmuir-Hinshelwood mechanism (section 2.2.2), can be written as (valid for each kind of surface plane):

$$r_1 = k_1 p_{H_2O}/p_0 \theta^* - k_{-1} \theta_{H_2O} \tag{2.80}$$

$$r_2 = k_2 \theta_{H_2O} \theta^* - k_{-2} \theta_{OH} \theta_H \tag{2.81}$$

$$r_3 = k_3 (\theta_{OH})^2 - k_{-3} \theta_{H_2O} \theta_O \tag{2.82}$$

$$r_4 = k_4 \theta_{OH} \theta^* - k_{-4} \theta_O \theta_H \tag{2.83}$$

$$r_5 = k_5 \theta_H^2 - k_{-5} p_{H_2}/p_0 (\theta^*)^2 \tag{2.84}$$

$$r_6 = k_6 p_{CO}/p_0 \theta^* - k_{-6} \theta_{CO} \tag{2.85}$$

$$r_7 = k_7\theta_{CO}\theta_O - k_{-7}\theta_{CO_2}\theta^* \tag{2.86}$$
$$r_8 = k_8\theta_{CO_2} - k_{-8}p_{CO_2}/p_0\theta^* \tag{2.87}$$
$$r_9 = k_9\theta_{CO_2}\theta_H - k_{-9}\theta_{HCOO}\theta^* \tag{2.88}$$
$$r_{10} = k_{10}\theta_{HCOO}\theta_H - k_{-10}\theta_{H_2COO}\theta^* \tag{2.89}$$
$$r_{11} = k_{11}\theta_{H_2COO}\theta_H - k_{-11}\theta_{H_3CO}\theta_O \tag{2.90}$$
$$r_{12} = k_{12}\theta_{H_3CO}\theta_H - k_{-12}\theta_{CH_3OH}\theta^* \tag{2.91}$$
$$r_{13} = k_{13}\theta_{CH_3OH} - k_{-13}p_{CH_3OH}/p_0\theta^* \tag{2.92}$$

This system can now be discretized by a backward difference scheme, equation 2.64, since there is no boundary condition for the reactor outlet considered. Therefore, a definition of the inlet boundary condition is sufficient for the model definition. In this thesis the feed-gas composition does not change during a single simulation, hence it is straightforward to define the following space boundary condition:

$$n_{i\,(z=0)} = n_{i_{Feed}} \tag{2.93}$$

As initial values the gas composition and coverages inside the reactor are specified, which can be conditions close to steady state or for example an uncovered catalyst and a gas phase exclusively comprised of inerts. In this case, equations 2.94 and 2.95 define the uncovered sites on each surface plane equal to one and hence the coverage of adsorbed species equal to zero at each point of the reactor:

$$\theta^*_{(t=0\,\mathrm{s})} = 1 \tag{2.94}$$
$$\theta_{ads\,(t=0\,\mathrm{s})} = 0 \tag{2.95}$$

Moreover the molar flow is constant at $t = 0\,\mathrm{s}$:

$$\dot{n}_{\,(t=0\,\mathrm{s})} = const. \tag{2.96}$$

In order to calculate this system of differential equations, all rate constants, k_j, have to be known or assumed.

Steady state conditions

Under steady state conditions, time dependent gradients can be neglected, which means equations 2.74 to 2.78 are transformed into ordinary differential equations or algebraic equations, respectively. One may further speculate that only a few of them are relevant under methanol synthesis conditions. When it is known or can savely be assumed that one or more reactions are in equilibrium, the system can be significantly simplified. This attempt was shown by Ovesen [11] and Askgaard et al. [10]. They reduced the system of rate equations 2.80-2.92 by assuming only step 2, 4, 7 and either step 10, 11 or 12 as rate determining [10]. In previous studies, steps 2, 4 and 7 were already considered to limit the water-gas shift reaction [11, 12, 14]. Under these assumptions,

the rates of fast steps in table 2.2 can be re-arranged to yield an equilibrated equation, i.e. for step 12:

$$k_{12}\theta_{H_3CO}\theta_H = k_{-12}\theta_{CH_3OH}\theta^* \tag{2.97}$$

or, with the condition for microscopic reversibility ($K_{12} = k_{12}/k_{-12}$):

$$K_{12}\theta_{H_3CO}\theta_H = \theta_{CH_3OH}\theta^* \tag{2.98}$$

where K_{12} is the equlibrium constant of step 12, which may be described by statistical thermodynamics (section 2.2.1.1). The other steps in equilibrium can be described in a similar manner. Furthermore, at steady state, a site balance for adsorbed hydroxyl groups and oxygen relates the considered slow steps in methanol synthesis [10]:

$$r_7 - r_{xx} = \frac{1}{2}\left(r_2 + r_4\right) \tag{2.99}$$

In here, the index xx can either represent step 10, 11, 12. However, Askgaard et al. [10] could show that step 11 is rate determining in the mechanism. The insertion of the rate equations yields a second order equation in the form of [10]:

$$a \cdot \frac{\theta_O}{\theta^*} + b \cdot \left(\frac{\theta_O}{\theta^*}\right)^{1/2} + c = 0 \tag{2.100}$$

Each plane is considered seperately, hence an active site must be either free or covered by an intermediate [10]:

$$\begin{aligned} &\theta^* + \theta_{H_2O} + \theta_{OH} + \theta_O + \theta_H + \theta_{CO} + \theta_{CO_2} \\ &+\theta_{HCOO} + \theta_{H_2COO} + \theta_{H_3CO} + \theta_{CH_3OH} = 1 \end{aligned} \tag{2.101}$$

The factors a, b and c can be derived from equation 2.99 and are given in the Appendix, as well as the derived explicit forms of the coverage of the surface intermediates. As Askgaard et al. [10] identified step 11 as rate determining step, the rate of methanol synthesis is equal to r_{11} and the reverse water-gas shift reaction equals the reverse reaction step 7:

$$r_{MeOH} = r_{11} = k_{11}K_{10}\theta_{HCOO}\theta_H^2/\theta^* - k_{11}/K_{11}\theta_{H_3CO}\theta_O \tag{2.102}$$

$$r_{RWGS} = -r_7 = k_7/K_7\theta_{CO_2}\theta^* - k_7\theta_{CO}\theta_O \tag{2.103}$$

Similar equations can be derived when step 10 or 12 is considered to be rate determining in methanol synthesis [10, 11]. These equations can now be used to calculate the whole system with only 5 ordinary differential equations, which enhances the computational time significantly. The only boundary needed is the feed gas composition at the reactor inlet. Calculating the system according to equations 2.80 to 2.92 with sufficient high rate constants k_j for the fast steps and assuring thermodynamic consistency (section 2.2.2) yields the same results.

Deactivation model

Using the microkinetic model, sintering effects can be directly related to a change in the total number of active sites. Furthermore, one might suspect that adsorbed gas molecules, i.e. water, or surface intermediates may further influence the relative surface free energy irreversible due to structural changes. Hence, the deactivation of the catalyst may comprise two effects: thermal sintering and irreversible changes in the catalyst morphology. Sintering is hereby considered analogous to the work of Løvik [30]. A deactivation model of Skrzypek et al. [51] was extended by a temperature-dependence and hence made applicable to industrial scale process data.

The total number of active sites is described by the following relationship:

$$N_{total} = N_{ini} \cdot \frac{\sum f_{hkl}\,(\gamma/\gamma_0) \cdot D_{hkl}}{\sum f_{hkl}\,((\gamma/\gamma_0)_{ini}) \cdot D_{hkl}} \cdot s \tag{2.104}$$

In here s describes the reduction in active sites, which is directly related to sintering effects according to [30]:

$$\frac{\partial s}{\partial t} = -A_d \cdot \exp\left[\frac{-E_d}{R} \cdot \left(\frac{1}{T} - \frac{1}{T_0}\right)\right] \cdot s(t)^5 \tag{2.105}$$

with an initial value for s:

$$s(t = 0\,\mathrm{s}) = s_0 \tag{2.106}$$

In order to account for the irreversible morphology changes of the catalyst, the equation for the contact surface free energy (equation 2.50) is modified as follows:

$$\frac{\gamma}{\gamma_0} = \frac{1 - \sqrt{(K_1 \cdot \frac{p_{H_2}}{p_{H_2 0}}) \cdot (K_2 \cdot \frac{p_{CO}}{p_{CO_2}})}}{1 + \sqrt{(K_1 \cdot \frac{p_{H_2}}{p_{H_2 0}}) \cdot (K_2 \cdot \frac{p_{CO}}{p_{CO_2}})}} + \chi\,(t) \tag{2.107}$$

The term $\chi\,(t)$ describes the progress of restructuring due to adsorbed species or surface intermediates in dependence of the exposure time. Hereby different dependencies, i.e. linear with time or a function of e can be considered.

2.4.2.2 Langmuir-Hinshelwood-Hougen-Watson model

In this thesis a LHHW model accoring to Vanden Bussche and Froment is considered [59]. According to their assumptions, only two steps in table 2.1 are rate determining, namely the dissociative adsorption of carbon dioxide and the hydrogenation of formiate to yield dioxomethylene:

$$\mathrm{CO_{2(g)}} + * \rightleftharpoons \mathrm{O*} + \mathrm{CO_{(g)}} \tag{2.108}$$

$$\mathrm{HCO_2 2*} + \mathrm{H*} \rightleftharpoons \mathrm{H_2CO_2 2*} + * \tag{2.109}$$

Implying pseudo-steady state for the surface intermediates and neglecting concentrations of higher carbonate structures, i.e. bicarbonate or methoxy, gives a total site balance [59]:

$$\theta^* + \theta^*_O + \theta^*_{H_2O} + \theta^{2*}_{HCOO} + \theta^{2*}_{CO_3} + \theta^*_H = 1 \tag{2.110}$$

where the surface concentrations are based on the total concentration of active sites, c_t. Further inspection of the system with regard to the rate determining steps and an elimination of the concentration of surface intermediates led to the following rate expressions for the reverse water-gas shift and methanol synthesis reactions [59]:

$$r_{MeOH} = k'_{5a} K_2 K_3 K_4 K_{H_2} p_{CO_2} p_{H_2} \left(1 - \frac{1}{K_{MeOH}} \frac{p_{H_2O} p_{CH_3OH}}{p^3_{H_2} p_{CO_2}}\right) \beta^3 \tag{2.111}$$

$$r_{RWGS} = k'_1 p_{CO_2} \left(1 - K_{RWGS} \frac{p_{H_2O} p_{CO}}{p_{H_2} p_{CO_2}}\right) \beta \tag{2.112}$$

In here, k'_{5a} equals $k_{5a} c_t^2$, $k'_1 = k_1 c_t$ and K_i is the equilibrium constant of the respective reaction in table 2.1. The normalized concentration of free active sites, β, relates the partial pressures to parameter groups obtained by the balance for surface species [59], given in the Appendix. These equations can be used for modeling the methanol synthesis reaction, analogous to the simplified microkinetic model (equations 2.102 and 2.103). In contrast to the microkinetic model, where all rate constants of non-equilibrated steps and equilibrium constants are deduced from separate experiments, these values are fitted simultaneously to the respective experimental results, which yields a total set of 10 parameters [59].

2.4.3 Temperature-programmed methods

Temperature-programmed methods are widely used for the evaluation of catalysts properties, i.e. active surface sites or for extraction of kinetic parameters [77–81]. In general, these experiments are carried out at UHV single crystals or at ambient pressure for high porous media. Temperature-programmed experiments under ambient pressure and flow are often performed using a glass-lined U-tube reactor, as displayed in figure 2.11. The ground catalyst is put between two glass wool plugs. The reactor is heated *via* an aluminum oven, which ensures an isothermal temperature profile in the fixed-bed [82].

When the temperature is raised linearly with time, both variables are coupled by:

$$T(t) = T(t = 0\,\mathrm{s}) + \beta t \tag{2.113}$$

where β is the heating rate in $\mathrm{K \cdot min^{-1}}$.

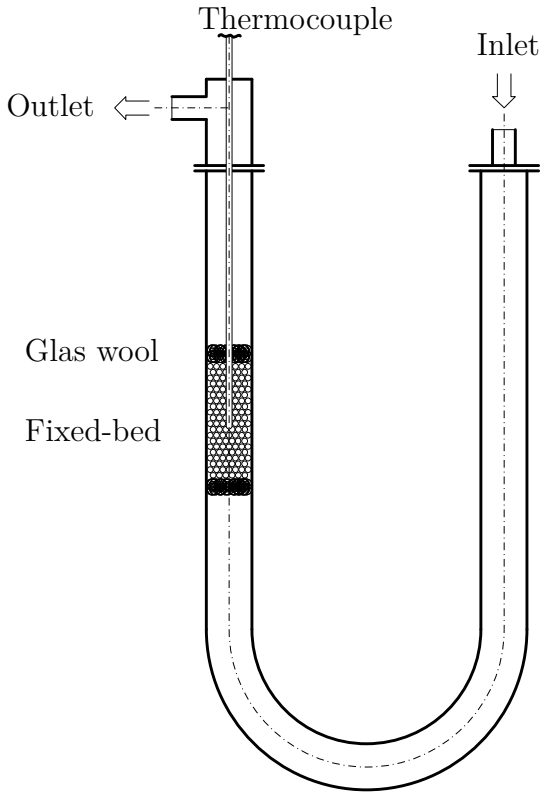

Figure 2.11: Flow TPD set-up, adapted from [82].

Furthermore, the volume flow will change with time according to:

$$Q(T) = Q_{std.}\frac{T}{T_N} \tag{2.114}$$

In here, *std.* denotes values at standard conditions ($T = 273.15\,\mathrm{K}$ and $p = 1\,\mathrm{bar}$). Furthermore, ideal gas behavior is assumed. In the following the general modeling aspects of temperature-programmed methods under ambient pressure are discussed.

2.4.3.1 Diffusion

Evaluation of temperature-programmed experiments under ambient pressure often requires treatment of diffusion limitations. Diffusional effects are related to mass transport due to concentration gradients over a reactor or particle. Usually, diffusion limitations during the experiments limit the direct evaluation of the flow experiments [2, 81]. Slow diffusion processes broaden the TP signal, since the transport to the outer surface of the particle is limited. Moreover, the TP signal maximum may be smaller and shifted to lower temperatures. As temperature-programmed experiments are transient

in time, the time-dependent concentration balance can be expressed *via* Fick's second law [75]:

$$\frac{\partial c_A}{\partial t} = D \, \frac{\partial^2 c_A}{\partial L^2} \tag{2.115}$$

Herein, D is the diffusion coefficient, c_A the concentration of A, t the time and L the position, i.e. particle radius. In this thesis particles are treated as spherical, this yields for a dimensionless particle length z with r_p being the particle radius [75]:

$$\frac{\partial c_A}{\partial t} = \frac{D}{r_p^2}\left(\frac{\partial^2 c}{\partial z^2} + \frac{2}{z}\frac{\partial c}{\partial z}\right) \tag{2.116}$$

This is equation is scaled by the ratio of $\frac{D}{r_p^2}$, where D in the case of molecular diffusion between two gas phase components varies with [83]:

$$D_{AB} \sim \frac{T^{3/2}}{p_{total}} \tag{2.117}$$

Usually the binary diffusion coefficient D_{AB} is in the range of $10^{-6}\,\mathrm{m^2 s^{-1}}$ to $10^{-5}\,\mathrm{m^2 s^{-1}}$ [84]. It can further be estimated by the following numerical value equation [85]:

$$\frac{p D_{AB}}{(p_A p_B)_{crit}^{1/3}\,(T_A T_B)_{crit}^{5/12}\,(1/M_A + 1/M_B)^{1/2}} = a\left[\frac{T}{(T_A T_B)_{crit}^{1/2}}\right]^b \tag{2.118}$$

with $a = 2.74{\cdot}10^{-8}$ and $b = 1.823$. In here, the specific pressures are given in bar, the temperatures in K and the molar weights in $\mathrm{g{\cdot}mol^{-1}}$.

However, in porous media such as porous catalysts, the geometry of the pores limits the diffusion between the molecules. Hence, the diffusion coefficient is corrected by the internal void fraction ϵ_p and the tortuosity factor Γ to yield an effective diffusion coefficient [83]:

$$D_{AB,e} = \frac{\epsilon_p}{\Gamma} D_{AB} \tag{2.119}$$

In here, the void fraction describes the pore volume relative to the volume of the particle and the tortuosity factor describes the inhomogeneity and "zigzag" nature of the pores. These values lie in the range of $0.2 < \epsilon_p < 0.7$ and $3 < \Gamma < 4$ [83], respectively.

These equations are generally valid when the pore diameter is greater than the mean free path of the diffusing gas molecules. However, when the pores are very small or the pressure is very low, the molecules collide with the pore walls very frequently, which can no longer be neglected. The diffusion regime changes and is no longer called molecular

diffusion, but Kundsen diffusion regime. The kinetic gas theory, assuming ideal gas behavior, gives the Knudsen diffusion coefficient as [83]:

$$D_K = 48.5\ d_{pore} \sqrt{\frac{T}{M_i}} \qquad [\mathrm{m^2\ s^{-1}}] \tag{2.120}$$

Analogous to the molecular diffusion, the Knudsen diffusion coefficient has to be related to the void fraction and tortuosity factor, when considering porous media:

$$D_{K,e} = 48.5\ \frac{d_{pore}\epsilon_p}{\Gamma} \sqrt{\frac{T}{M_i}} \quad [\mathrm{m^2\ s^{-1}}] \tag{2.121}$$

2.4.3.2 Criteria for TPD flow experiments

Before analyzing TPD flow experiments, several criteria can be applied to check for possible limitations for evaluation of such experiments. Kanervo et al. [81] gave an overview on different published parameters for the design of temperature-programmed desorption experiments, which summarizes the criteria published by Demmin and Gorte [86]. These dimensionless parameters are given in table 2.5.

Table 2.5: Criteria for TPD experiments [86], taken from ref. [81].

Dimensionless parameter	Tested effect	Ideal requirement
D-G 1: $\frac{\epsilon_b L \pi d_b^2 \beta}{4Q(T_f - T_{ini})}$	Convective lag	< 0.01
D-G 2: $\frac{\epsilon_b r_p^2 \beta}{D_e(T_f - T_{ini})}$	Diffusive lag	< 0.01
D-G 3: $\frac{\rho_p r_p^2 Q}{3 w_{cat} D_e}$	Particle concentration gradients	< 0.05
D-G 4: $\frac{4QL}{\pi d_b^2 D_{ax}}$	Bed concentration gradients	< 0.1 (for CSTR)
D-G 5: $\frac{N_{tot}\rho_p r_p^2}{3D_e} k_{ads}$	Re-adsorption at infinite flow rate	< 1
D-G 6: $\frac{N_{tot}\rho_p \pi d_b^2 L(1-\epsilon_b)}{4Q} k_{ads}$	Re-adsorption at low flow rate	< 1

In here, ϵ_b represents the porosity, L the length, w_{cat} the mass and d_b the diameter of the catalyst bed. The radius and density of catalyst particle are denoted by r_p and ρ_p. β is the heating rate, Q the volumetric flow rate, D_{ax} the axial dispersion coefficient, D_e the effective diffusion coefficient, N_{tot} the number of active sites and k_{ads} corresponds to the rate constant of adsorption. The final and initial temperature are represented by T_f and T_{ini}, respectively. All parameters listed in table 2.5, D-G, are dimensionless ratios of rates of elementary dynamic processes [81]. D-G 1 through D-G 6 can determine possible convective and diffusive lags, particle and bed concentration gradients, as well as re-adsorption effects.

Experiments are usually carried out at conditions where convective and diffusive lags can be excluded [81]. Hereby, D-G 1 is the ratio of the reactor residence time to the

total time of an experiment and D-G 2 the respective ratio to the diffusion effect. As high flow rates are common for such experiments, the suggested requirements are always satisfied under typical temperature-programmed desorption conditions.

Possible particle concentration gradients can be analyzed by D-G 3, which relates the convective flow to the rate of diffusion. The respective dimensionless term was furthermore expanded by Kanervo et al. [81] and differs by the factor of $3(1\text{-}\epsilon_b)/\epsilon_b$, which enlarges the ideal requirement to 0.16 [81].

Parameter D-G 4 relates the gas flow to the rate of axial mixing and depends on the axial dispersion coefficient. Axial dispersion may be caused by turbulences, uneven velocity distributions in the reactor cross section or molecular diffusion [85]. Molecular diffusion, however, has a very weak influence compared to the other effects. The term for axial dispersion originates from Fick's second law (see also equation 2.115). The corresponding value for D_{ax} can be calculated using the dimensionless Peclet number $Pe = \bar{u}d_p/D_{ax}$, which is the ratio of convective flow to the rate of diffusion. For a packing of spheres, a value for Pe around two is obtained [85]. Backmixing and turbulence may be present during a TPD experiment, when D-G 4 is larger than 0.1 [81, 86].

Finally, D-G 5 and D-G 6 are related to re-adsorption effects, depending on the rate of diffusion (D-G 5) and the gas flow rate (D-G 6). Both criteria are highly influenced by the rate constant of adsorption. Kanervo et al. [81] found a definitive presence of re-adsorption evaluated at typical experimental conditions, when re-adsorption is a non- or low-activated process. These effects may further affect the possibility to analyze the pure desorption parameters. However, under quasi-equilibrium conditions, the ratio of adsorption to desorption parameters can be derived [81].

2.4.3.3 Reactor models

In order to extract the different kinetic parameters, i.e. E_{des} or A_{des}, the concentration along the U-tube reactor can be calculated by different reactor models, which will now be discussed in more detail. The validity and applicability of the different reactor models or intraparticle transfer limitations, which is often accompanied by several assumptions regarding flow properties or diffusional aspects, can be estimated by the criteria discussed in the previous section 2.4.3.2. An overview of the implemented reactor models is given in figure 2.12.

For all models considered below, time and space time boundaries have to be specified. Usually such boundaries are given by the coverages at $t = 0\,\mathrm{s}$, $\theta\,(t = 0\,\mathrm{s}, x)$, the reactor inlet concentration, $c\,(t, x = 0)$ and the concentration inside the reactor $c\,(t = 0\,\mathrm{s}, x)$.

Continuously stirred-tank reactor

The (ideal) continuously stirred-tank reactor (CSTR) is, from a mathematical point of view, the simplest reactor model that can be applied. The CSTR is an ideal reactor, where complete back-mixing is assumed ($Pe \to 0$). That means there are no local

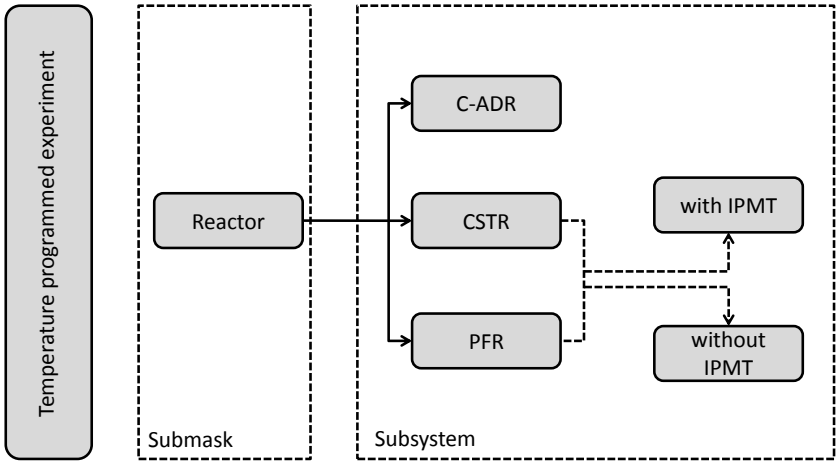

Figure 2.12: Model structure for evaluating temperature-programmed experiments.

temperature or concentration gradients in the reactor. The concentration in the reactor can be calculated by an ordinary differential equation [81]:

$$\frac{\partial c_A}{\partial t} = -\frac{1}{\tau(t)}\, c_A + \gamma \tag{2.122}$$

where c is the concentration, τ the residence time, t the time and γ a source term, originating from surface reactions or sorption processes, specified below.

Plug flow reactor

The (ideal) plug flow reactor (PFR) can be characterized by the absence of any back-mixing or dispersion ($\mathrm{Pe} \to \infty$). The velocity profile for a cross section is constant but can vary along the reactor axis. This can be explained by the continuity equation, with a constant mass flow along the axial coordinate. This yields a partial differential equation [81]:

$$\frac{\partial c_A}{\partial t} = -\frac{u(t)}{L\epsilon_b}\,\frac{\partial c_A}{\partial x} + \gamma \tag{2.123}$$

In here, $u(t)$ is the superficial velocity, L the length of the reactor and ϵ_b the void fraction of the catalyst bed.

Convection-axial dispersion reactor model

The convection-axial dispersion reactor model (C-ADR) can describe any behavior of both reactor models stated above. It is an extension of the PFR model with a term for axial dispersion, treated as a diffusion-like process superimposed on the plug flow [87]. The term D_{ax} introduces any kind of uneven distribution along the reactor and can be calculated by the Peclet number (see section 2.4.3.2).

$$\frac{\partial c_A}{\partial t} = \frac{D_{ax}}{L^2\ \epsilon_b}\ \frac{\partial^2 c_A}{\partial x^2} -\ \frac{u(t)}{L\epsilon_b}\ \frac{\partial c_A}{\partial x} + \gamma \tag{2.124}$$

Intraparticle mass transfer

The source term, introduced above may be given by

$$\gamma = \frac{(1-\epsilon_b)\,\rho_p N_{sites}}{\epsilon_b} r_i \tag{2.125}$$

when intraparticle mass transfer can be neglected. In here, ρ_p represents the particle density, N_{sites} the number of active sites per catalyst weight and r_i an elementary rate equation, i.e. equation 2.80. Intraparticle mass transfer can be described by the following relationship [81]:

$$\gamma_{IPMT} = -\ \frac{3D_e(1-\epsilon_b)}{r_p^2\epsilon_b}\frac{\partial c}{\partial z}\Big|_{z=1} \tag{2.126}$$

where D_e is the effective diffusion coefficient, r_p the particle radius and $z = 1$ denotes the particle outer surface. For spherical particles, the following differential equation describes the concentration inside this particle [81]:

$$\frac{\partial c_A}{\partial t} = \frac{D_e}{r_p^2\epsilon_p}\left(\frac{\partial^2 c_A}{\partial z^2} + \frac{2}{z}\frac{\partial c_A}{\partial z}\right) + \frac{\rho_p N_{sites}}{\epsilon_p}\left(-\ \frac{\partial \theta}{\partial t}\right) \tag{2.127}$$

For solving this equation two additional boundaries are needed. The first one is given by:

$$\frac{\partial c}{\partial z}\Big|_{z=0} = 0 \tag{2.128}$$

which describes the symmetry inside the particle. The second boundary condition at $z = 1$ is given by the respective differential equation of the chosen reactor model at $z = 1$.

2.5 Sensitivity analysis

Modeling chemical systems always includes uncertainties in the evaluated parameters, such as rate constants, activation energies or thermodynamic properties [88]. It is crucial for a model definition to analyze which parameters are important and hence identify the most influencing parameters. This aspect is commonly done by conducting a sensitivity analysis [89].

Sensitivity analysis can also help to simplify complex catalytic reaction mechanisms by elimination of insensitive parameters. These systems may include many elementary reactions and therefore unknowns. Identification of the insensitive steps of such mechanisms can help to reduce the number of unknowns, while maintaining the behavior of the overall system [90]. Especially Campbell [91] suggested the "degree of rate control" as a useful strategy to find the rate determining step(s) in a complex reaction mechanism.

A lot of methods for sensitivity analysis exist, which can be separated in global and local methods. Hereby, a local sensitivity analysis is based on gradients around the nominal solution and hence is only valid for little changes in the system. Common methods for the local sensitivity analysis include *finite differences*, *direct differential methods* and the *Green's function method* [88].

A global sensitivity analysis, which is often based on stochastics, leads to sensitives which are valid for a wide range of the parameter space. By calculation of averaged sensitivities over the region of parameters uncertainty, large variations in the evaluated parameters can be captured, which may however differ from those obtained by a local sensitivity analysis [88, 90].

The choice of the sensitivity analysis should always be dedicated to the system studied [88]. In general local methods require less extensive calculations and provide a higher level of detail. In this thesis the sensitivity analysis is used to identify the most influencing parameters on the rate of methanol synthesis at specific operating conditions, hence the local sensitivity analysis is chosen and now discussed in more detail. Besides, this method was proven to be highly informative when analyzing chemical reaction schemes [91].

A general differential equation for a typical problem in sensitivity analysis reads:

$$\frac{\partial c}{\partial t} = f\left(c, \vec{par}, t\right), \text{ with } c\left(0\right) = c_0 \tag{2.129}$$

In here, c represents a dependent variable, i.e. a species concentration and $\vec{par}$ is a vector of the length m for all independent model parameters, including the initial conditions. The integration variable is given by t and it is assumed that f is continuous and can be constantly differentiated [90]. The system can be calculated at a specific solution, which yields a nominal unique solution for a reference case:

$$c_{ref} = c\left(t, \vec{par}\right) \tag{2.130}$$

Upon variation of one parameter par_i in the parameter vector $\vec{par}$ by a value of Δpar_i, a new solution for c is obtained:

$$c_{var} = c\left(t, par_i + \Delta par_i\right) \tag{2.131}$$

where for clarity only the varied parameter is listed. All other parameters remain unchanged. A Taylor series in the form of

$$\begin{aligned} c\left(t, par_i + \Delta par_i\right) = c\left(t, par_i\right) + \frac{\partial c\left(t, par_i\right)}{\partial par_i} \cdot \Delta par_i \\ + \frac{\partial^2 c\left(t, par_i\right)}{\partial par_i^2} \cdot \frac{\Delta par_i^2}{2!} + \ldots \end{aligned} \tag{2.132}$$

can approximate the new solution of c, as c is a continuous function of par_i [90]. For very small changes of Δpar_i this series can be terminated after the second term [90].

Finally, the definition of the first-order sensitivity s for infinitesimal small changes of par_i reads:

$$s\left(c, par_i\right) = \frac{\partial c\left(t, par_i\right)}{\partial par_i} = \lim_{\Delta par_i \to 0} \frac{c\left(t, par_i + \Delta par_i\right) - c\left(t, par_i\right)}{\Delta par_i} \tag{2.133}$$

This absolute index can further be normalized by $par_i / c\left(t, par_i\right)$ to yield a relative dimensionless sensitivity, S [90]:

$$S\left(c, par_i\right) = \frac{\partial c\left(t, par_i\right)}{\partial par_i} \cdot \frac{par_i}{c\left(t, par_i\right)} \tag{2.134}$$

As mentioned before, several methods to calculate the local sensitivity can be applied. A very common way to calculate the derivative $\partial c\left(t, par_i\right) / \partial \vec{par}$ is the finite difference approximation. First, the model equation is solved for the reference case. Afterwards each parameter par_i is varied one by one and the variation in c is calculated:

$$\Delta c_{var} = c\left(t, par_i + \Delta par_i\right) - c\left(t, par_i\right) \tag{2.135}$$

The respective sensitivity is then given by:

$$s\left(c, par_i\right) = \frac{\partial c\left(t, par_i\right)}{\partial par_i} \approx \frac{\Delta c\left(t, par_i\right)}{\Delta par_i} = \frac{c_{var} - c_{ref}}{par_{i,var} - par_{i,ref}} \tag{2.136}$$

In order to calculate the sensitivity index of all parameters m for all model cases n, $n \times m$ model equation have to be solved, when only one species is considered. Using finite differences, two important conditions should be met [88]. The smaller the change in par_i, the smaller the error in the calculated sensitivity. However, Δpar_i should hold the condition:

$$\Delta par_i \geq \frac{f_c \cdot c\left(t\right)}{f_s \cdot s\left(c, par_i\right)} \tag{2.137}$$

where f_i is the respective error in c or s, respectively. Practically, the variation of par_i should be big enough to change the result of c more than the specified tolerance in the calculation of c. On the other hand, Δpar_i should be chosen as small as possible, to minimize the error from the termination after the second term of the Taylor series [88, 90]. Especially when high sensitivities are obtained, small values of Δpar_i should be chosen. For analyzing reaction mechanisms, Campbell [91] suggested a variation of 1%, however linearity in the response of Δc should be checked in each case. Using the suggested variaton of par_i, each parameter can be calculated to:

$$par_{i,var} = par_{i,ref} + par_{i,ref} \cdot 1\% = (1 + 1\%) \cdot par_{i,ref} \tag{2.138}$$

In order to check for linearity, each parameter should also be varied by -1% and the modulus of the resulting change in c_{ref} should be equal for both cases.

The relative local sensitivity is then given by:

$$S(c, par_i) = \frac{\Delta c}{\Delta par_i} \cdot \frac{p_{i,ref}}{c_{ref}} = \frac{c_{var} - c_{ref}}{1\% \cdot c_{ref}} \tag{2.139}$$

A positive S indicates a limiting parameter, which means when the parameter is increased an increase in c can be observed, whereas a negative relative sensitivity defines an inhibiting parameter, which lowers c with an increase in the respective parameter. Campbell [91] introduced this nomenclature in terms of the influence of the rate constants of an elementary step in a reaction mechanism on the overall reaction rate. All steps with nonzero sensitivities are herein called rate controlling or slow steps [91].

3 Detailed kinetic modeling of methanol synthesis over a ternary copper catalyst

3.1 Abstract

Three differently detailed kinetic models for methanol synthesis are derived for experimental data measured over a ternary copper catalyst. Two global reactor models for reaction design, including a power law and a Langmuir-Hinshelwood-Hougen-Watson approach, are presented. In addition a microkinetic model is adapted to describe the whole experimental data and is used to discuss dynamical changes occurring during methanol synthesis. The first global model based on power law kinetics is very precisely in predicting the integral rates of methanol production. The power law requires the inclusion of a water inhibition term to be applicable over the whole range of experiments. A semi-empirical Langmuir-Hinshelwood-Hougen-Watson model, taken from the literature, gives essentially the same results, even upon extrapolation. The third model, a microkinetic model, was successfully fitted with only two variables and is in reasonable agreement with the experimental data. For all models a sensitivity analysis shows the influencing parameters on the methanol production rate. The valid microkinetic model, however, can give qualitative estimations of the structure sensitivity and dynamic behavior of methanol synthesis. The dynamic change of active sites and site distribution of different copper low-index planes along the reactor length is given and the inhibiting role of water, indicated by the power law and microkinetic model, is analyzed.

3.2 Introduction

Methanol counts among the most important basic chemicals in industry and becomes more and more important as a chemical energy carrier, i.e. as fuel for fuel cells [19, 92]. Moreover, it is a promising energy carrier, which can easily be handled by the existing gasoline infrastructure. Nowadays, methanol is commercially synthesized over $Cu/ZnO/Al_2O_3$ catalysts in a low-pressure (50 - 100 bar) and low-temperature (473.15 - 573.15 K) process. Three overall reactions describe the formation of methanol when a feed of CO_2, CO and H_2 is employed. Methanol can be formed *via* the highly exothermic hydrogenation of carbon monoxide and carbon dioxide [19].

$$CO + 2\,H_2 \rightleftharpoons CH_3OH \qquad \Delta H_{298\,K} = -90.85\,kJ \cdot mol^{-1} \tag{3.1}$$

$$CO_2 + 3\,H_2 \rightleftharpoons CH_3OH + H_2O \qquad \Delta H_{298\,K} = -49.82\,kJ \cdot mol^{-1} \tag{3.2}$$

In addition, carbon monoxide can be converted *via* the water-gas shift reaction, which is under the mentioned conditions also exothermic and equilibrium-limited.

$$CO + H_2O \rightleftharpoons CO_2 + H_2 \qquad \Delta H_{298\,K} = -41.03\,kJ \cdot mol^{-1} \tag{3.3}$$

It is generally accepted that methanol is primarily formed *via* the hydrogenation of carbon dioxide [32–34]. However, there is still a debate about the active site and the synergy effect of the different catalysts components. Generally, the activity in methanol synthesis is somehow proportional to the area of the metallic copper [39–41]. The different effects of each component are discussed controversially in current literature. While aluminum oxide is believed to act as a structural promoter and reduces sintering effects, the interaction of zinc oxide and copper are still to be investigated. A significantly higher activity for a ternary copper zinc alumina catalyst is exhibited than for copper on alumina [44]. Several theories exist how ZnO and Cu interact. Zinc oxide microcrystallites could stabilize a strain in the copper particles, leading to higher methanol production rates [47, 93]. Another attempt to explain the synergy effect of ZnO and Cu is a Cu-Zn alloy formation [26, 27, 50]. Nakamura et al. [23, 49] describe the hydrogenation of carbon monoxide and dioxide over two different active sites, depending on the gas applied. Methanol from carbon dioxide proceeds over copper zinc alloys, which are formed by zinc dissolved into the copper particles, whereas carbon monoxide hydrogenation is catalyzed by Cu-O-Zn species [23, 49]. Gas-dependent morphology changes of Cu on ZnO have been found using *in-situ* extended X-ray adsorption fine structure (EXAFS) measurements [24, 25]. This was also referred as wetting/non-wetting behavior [25]. Depending on the reduction potential of the gas phase, the copper particles are spherical (oxidizing) or disk like (reducing), which was also visualized by *in-situ* TEM measurements [28, 29]. Under reducing conditions a stronger metal surface interaction is found, which exhibits higher activity for methanol synthesis [29, 41]. Recently, a microkinetic model was developed by Grabow and Mavrikakis [31], based on density functional theory calculations on Cu(111). After fitting the data to experimental values, they found that possibly a more open and partially oxidized Cu facet might be more suitable to represent the active site for methanol synthesis [31]. In their work only the exposed copper (111) facets are responsible for the catalytic activity, but according to the authors the synergetic effect cannot be excluded by their findings.

Kinetic modeling is always a great subject in heterogeneous catalysis [2, 94]. Depending on the level of understanding for the catalytic reaction, different approaches in engineering multiscale kinetic modeling can be applied [4, 11, 13, 58, 59]. Global kinetic models, i.e. in the simplest case power laws or Langmuir-Hinshelwood-Hougen-Watson models (LHHW) are mainly used for reactor design and operation of chemical reactors [95]. On the other side, by introducing the surface chemistry modeling based on elementary steps leads to microkinetic models [2, 4, 94]. In case of methanol synthesis, a variety of global kinetic models were postulated during the last decades. In the

simplest case, power laws or Langmuir-Hinshelwood-Hougen-Watson models (LHHW) were used to describe the synthesis reaction. First, carbon monoxide was believed to be the only carbon source to form methanol. Later on, also carbon dioxide was also considered [53, 58]. However, ^{14}C-labeling experiments showed that carbon dioxide is the main carbon source in methanol synthesis, carbon monoxide is primarily converted by the water-gas shift reaction [32]. Vanden Bussche and Froment [59] developed a kinetic model based on this knowledge, also on pseudo-mechanistical basis, which will be discussed later in more detail.

The first microkinetic model for methanol synthesis based on elementary steps was developed by Askgaard et al. [10]. It was developed from results obtained in surface science studies, proposing metallic copper as the active site. The microkinetic model for the water-gas shift reaction by Ovesen et al. [11, 12, 14] was incorporated. Table 3.1 shows the proposed elementary reactions.

Table 3.1: Elementary steps in methanol synthesis, according to ref. [10].

Step	**Surface reactions**		
1	$H_2O_{(g)} + *$	$\rightleftharpoons$	H_2O*
2	$H_2O* + *$	$\rightleftharpoons$	$OH* + H*$
3	$2\,OH*$	$\rightleftharpoons$	$H_2O* + O*$
4	$OH* + *$	$\rightleftharpoons$	$O* + H*$
5	$2\,H*$	$\rightleftharpoons$	$H_{2(g)} + 2*$
6	$CO_{(g)} + *$	$\rightleftharpoons$	$CO*$
7	$CO* + O*$	$\rightleftharpoons$	$CO_2* + *$
8	CO_2*	$\rightleftharpoons$	$CO_{2(g)} + *$
9	$CO_2* + H*$	$\rightleftharpoons$	$HCOO* + *$
10	$HCOO* + H*$	$\rightleftharpoons$	$H_2COO* + *$
11	$H_2COO* + H*$	$\rightleftharpoons$	$H_3CO* + O*$
12	$H_3CO* + H*$	$\rightleftharpoons$	$CH_3OH* + *$
13	CH_3OH*	$\rightleftharpoons$	$CH_3OH_{(g)} + *$

The first eight steps describe the water-gas-shift reaction *via* a redox mechanism. Subsequently, methanol is formed *via* the successive hydrogenation of adsorbed carbon dioxide. Thereby, the hydrogenation of H_2COO_{ads} is considered as the rate-determining step for methanol synthesis. The microkinetic model was successfully extrapolated to industrial conditions [10]. However, Askgaard et al. [10] found a systematic deviation from measured data at high or low ratio of p_{CO}/p_{CO_2}. Ovesen et al. [13] eliminated most of the deviations of the model by Askgaard et al. [10] allowing the total copper area to depend on the reduction potential of the gas phase. The *via* reduction formed oxygen vacancies in the Cu-O-Zn interface influence the particle shape and increase the total number of active sites. The flatter the copper particles are, the higher the exposed

surface area and therefore the number of active sites is. Structure sensitivity on the different exposed copper low-index planes (111), (110), (100) was introduced. The gas atmosphere-dependent ratio of facets can be derived using the Wulff construction. The model morphology changes were incorporated into the microkinetic model by Ovesen et al. [13].

This work compares three approaches at different theoretical input to model the methanol synthesis under industrial conditions with respect to their applicability and validity. These approaches are namely a power law, a LHHW model and the dynamic microkinetic model by Ovesen et al. [13].

3.3 Experimental and computational section

The experiments were performed over an industrial ternary $Cu/ZnO/Al_2O_3$ catalyst. The dry syngas consisted of carbon monoxide, carbon dioxide, hydrogen and nitrogen as an inert. It was dosed *via* mass flow controllers (Brooks, model 5850TRG). The following gases of high purity were used: 20% CO_2 (99.997%) in H_2 (99.9999%), H_2 (99.9999%), N_2 (99.9999%), CO (99.998%). The experimental setup (figure 3.1) consists of four independent dosing lines, allowing a variation of the feed gas composition.

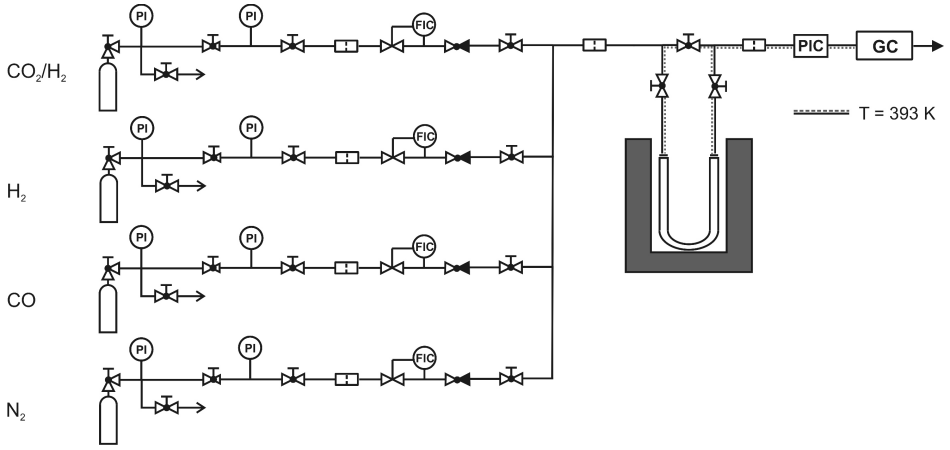

Figure 3.1: Experimental setup.

Gas analysis is carried out by two isotherm operating gas chromatographs (Shimadzu 14A, Shimadzu 8A) with different columns. A Porapak N column (Supelco) was used to determine the concentrations of carbon dioxide, water and methanol, whereas a Molsieve 5 Å column (Supelco) was incorporated to measure the effluent of carbon monoxide and nitrogen. Hydrogen was determined by the material balance to yield 100%. The whole set-up was heated to 393 K in order to avoid unwanted condensation of water or methanol. In order to operate the reactor in an isothermal way and to avoid hot spots, about 0.2 g of the catalyst were mixed with 0.8 g SiC, which by itself did not exhibit any catalytic activity. The catalyst was ground into a sieve fraction of 250–355 μm to ensure an uniform distribution over the catalyst bed and to avoid diffusion limitations.

Severe aging of the catalyst was performed before the kinetic investigation in order to circumvent the initial formation period [44]. The following kinetic measurements exhibited further slightly deactivation, which were carefully observed and as a good approximation assumed to be linear [44]. After the experiments the specific copper metal surface area was measured *ex-situ* to yield 14.4 $m^2 \cdot g_{cat}^{-1}$ by the N_2O frontal chromatography method under mild reaction conditions, using a N_2O/He mixture (1% N_2O in He (99,9999%)) [96–98]. Experimental conditions ranged from 5 to 60 bar and 463.15 - 523.15 K, also varying the composition of the dry synthesis gas, yielding CO_x conversions of about 0.2 - 14%. The experimental conditions are summarized in table 3.2. Experiments were carried out in three periods. In the first period, the residence time was varied at a total pressure of 60 bar in the whole temperature range at standard feed conditions, yielding a set of 28 experimental values. Second, the feed was varied in the range of 59.5 ± 10% H_2, 8 ± 3% CO_2, 6 ± 3% CO and balance N_2. This led to a set of seven different synthesis gas compositions at a total pressure of 60 bar and temperatures ranging from 463.15 to 523.15 K (28 data points). Finally, the total pressure of two feed gas compositions (59.5% H_2, 8% CO_2, 6% CO, balance N_2 as well as 72% H_2, 4% CO_2, 10% CO, balance N_2) was varied at different temperatures. This yielded additional 47 experimental data points, evaluated for the kinetic study. In each period, the standard feed was studied at a total pressure of 60 bar and 100 $Nml \cdot min^{-1}$ while varying the temperature, in order to obtain reliable data for taking into account the deactivation of the calalyst as a function of time on stream.

Table 3.2: Experimental conditions.

Bed length	0.017 m
Bed diameter	0.008 m
Temperature	463.15 – 523.15 K
Volume flow	100 – 500 $Nml \cdot min^{-1}$
Pressure	5 – 60 bar
Catalyst	$Cu/ZnO/Al_2O_3$
Catalyst weight	0.2003 g
SiC dilution	0.7995 g
Synthesis gas composition	59.5 ± 10% H_2, 8 ± 3% CO_2, 6 ± 3% CO, balance N_2
	72% H_2, 4% CO_2, 10% CO, balance N_2
Standard feed	59.5% H_2, 8% CO_2, 6% CO, balance N_2

In this work the fixed-bed reactor is modeled as an isothermal plug flow reactor:

$$\frac{\partial \dot{n}_i}{\partial z} = \sum_{j=1}^{2} \left(\lambda_{ij} r_j\right) \omega_{cat} \qquad i = 1, ..., 5 \tag{3.4}$$

Hereby, $\dot{n}_i$ is the molar flow of a specific species along the dimensionless reactor coordinate z, λ the respective stoichiometric coefficient, r_j the rate of methanol formation (reaction 3.2) or reverse water-gas shift reaction (reaction 3.3) and ω_{cat} the mass of

the catalyst (for global models) or the number of active sites (microkinetic model) in g_{cat} or mol, respectively. It is assumed that methanol is formed *via* carbon dioxide hydrogenation (j = 1), whereas carbon monoxide can form carbon dioxide *via* the water-gas shift reaction (j = 2):

$$CO + H_2O \longleftrightarrow CO_2 + H_2 \underset{\pm 2\,H_2}{\longleftrightarrow} CH_3OH + H_2O \tag{3.5}$$

This yields a set of five ordinary differential equations for the reactive gas species in an isothermal plug flow reactor. Thorough parameter estimations were performed based on the experimental data. The presented values were found using the Athena Visual Studio engineering software [73], with a build-in solver and fitting routine. Weighted nonlinear least square routines, with a trust region method, were selected to optimize the model parameters. The objective function included the integral rate of methanol and for the global models also the rate of water formation, being derived from a closed carbon balance. Gradients were calculated using a forward difference scheme; the objective function tolerance was set to 10^{-10}. In case of Arrhenius constants, the parameters were parameterized in the form of:

$$k_i = A^* \cdot \exp\left(\frac{E_i}{R} \cdot \left(\frac{1}{T} - \frac{1}{T_{av}}\right)\right) \tag{3.6}$$

with

$$A^* = A \cdot \exp\left(\frac{E_i}{R \cdot T_{av}}\right) \tag{3.7}$$

This parameterization was done at an average temperature T_{av} of 493.15 K. Thus, all parameters are reported in parameterized and re-parameterized form. The goodness of the respective model was evaluated by the parity of the integral rate of methanol formation and the coefficient of determination (R^2). A local sensitivity analysis [88] for all parameters was conducted by finite differences in the form of a relative sensitivity coefficient:

$$S = \frac{par_i}{R_{MeOH}} \cdot \frac{\partial R_{MeOH}}{\partial par_i} = \lim_{\Delta par_i \to 0} \frac{R_{MeOH,var} - R_{MeOH,ref}}{R_{MeOH,ref} \cdot var} \tag{3.8}$$

Hereby par_i represents the evaluated parameter, R_{MeOH} the integral rate of methanol synthesis and var the variation of the respective parameter. Unless otherwise stated, the variation was chosen to be 1% as suggested by Campbell et al. [91]. For the microkinetic model, the reverse reaction rate constant is related to the forward reaction rate constant as follows:

$$k_i^- = \frac{k_i^+}{K_i} \tag{3.9}$$

where K_i is the equilibrium constant of a specific elementary reaction as well as k_i^+ and k_i^- denote the reaction rate constants in the forward or reverse direction of each

elementary step, respectively. Hence, a change of k_i^+ does not change the equilibrium constant, assuring microscopic reversibility. Each parameter is varied one by one. For significant sensitivities linearity for the change in R_{MeOH} was checked. Sensitivities are also cross-checked using MATLAB® R2010b (Mathworks Inc.).

In global models, the chemical equilibrium is often accounted for using an equilibrium term $(1-\beta_i)$. Hereby β_i represents the approach to the chemical equilibrium for methanol synthesis or the reverse water-gas shift reaction, respectively:

$$\beta_1 = \beta_{MeOH} = K_{MeOH}^{-1} p_0^2 f_{H_2O} f_{CH_3OH} / \left(f_{H_2}^3 f_{CO_2} \right) \tag{3.10}$$

$$\beta_2 = \beta_{RWGS} = K_{WGS} f_{H_2O} f_{CO} / \left(f_{H_2} f_{CO_2} \right) \tag{3.11}$$

The equilibrium term becomes zero at the chemical equilibrium. The equilibrium constants K_{MeOH} and K_{WGS} are calculated by the means of statistical thermodynamics, explained by Ovesen et al. [11, 14] and are used for all models discussed later. For global models, the statistical thermodynamics of the gas phase are transformed into the following form:

$$K_i = 10^{\frac{PK_{i,1}}{T} - PK_{i,2}} \tag{3.12}$$

The values are given in table 3.3 and for the WGS comparable to the parameters found experimentally by Graaf et al. [99]. In case of methanol synthesis from CO_2 the overall equilibrium constant differs up to 17% compared to the results by Graaf et al. [99]. The species are represented by their fugacities, calculated by an Athena built-in subroutine. A calculation according to Soave-Redlich-Kwong [100, 101] showed essentially the same results.

Table 3.3: Parameters for equilibrium constants.

	PK_1	PK_2
MeOH	2980.8	10.346
WGS	2083.3	2.043

3.4 Results and discussion

Depending on the level of understanding of a catalytic process, differently detailed models can be used to describe the chemical apparent kinetics.

3.4.1 Power law model

Usually, when there is little information on the mechanism of a chemical reaction, power laws are used to describe reactive systems [12], i.e.

$$r_{MeOH} = A_{MeOH} \cdot \exp\left(E_{a,MeOH}/\left(RT\right)\right) f_{H_2}^{\alpha_{H_2}} f_{CO_2}^{\alpha_{CO_2}} \cdot \left(\xi + f_{H_2O}\right)^{\alpha_{H_2O}} \left(\xi + f_{CH_3OH}\right)^{\alpha_{CH_3OH}} \left(1 - \beta_{MeOH}\right) \tag{3.13}$$

$$r_{RWGS} = A_{RWGS} \cdot \exp\left(E_{a,RWGS}/\left(RT\right)\right) f_{H_2}^{\varphi_{H_2}} f_{CO_2}^{\varphi_{CO_2}} \cdot \left(\xi + f_{H_2O}\right)^{\varphi_{H_2O}} f_{CO}^{\varphi_{CO}} \left(1 - \beta_{RWGS}\right) \tag{3.14}$$

The reaction rates are reported in $\mathrm{mol \cdot s^{-1} \cdot kg_{cat}^{-1}}$. In these equations, all gaseous species are represented by their fugacity f (in Pa) and a reaction order α or φ, respectively. Since the feed gases used (see also table 3.2), representing typical feed compositions for methanol synthesis, neither contained water nor methanol in measurable amounts, a term ξ (in Pa) was introduced to account for a possible inhibition by the products formed. This allows the reaction rate to be finite in the absence of methanol or water, respectively. An analysis without an inhibition of water showed unsatisfying results. In total, the set of 13 adjustable parameters comprise of A_i, $E_{a,i}$, ξ and the reaction orders for the particular species in the respective reaction. Figure 3.2 shows the respective parity plot for the integral rate of methanol formation.

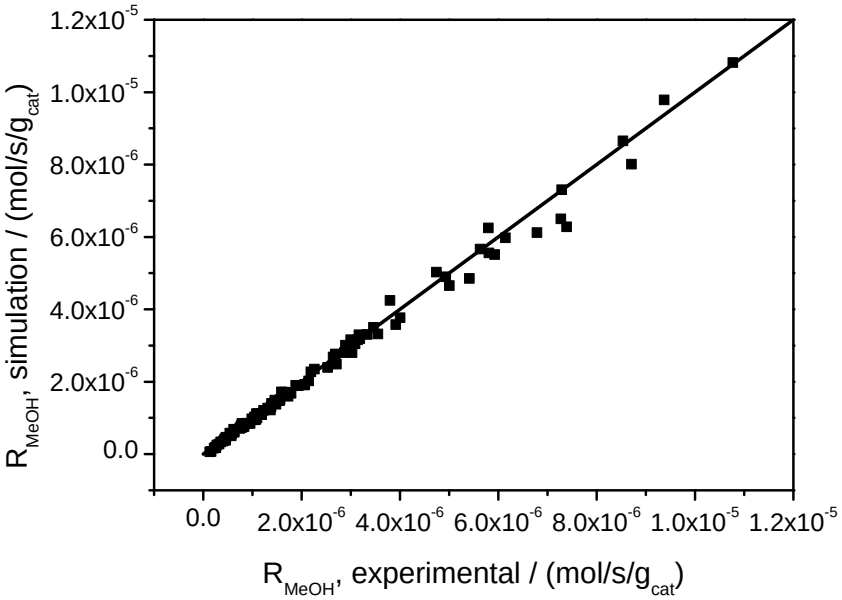

Figure 3.2: Parity plot of the power law model.

A good agreement between measurement and experiment is obtained, also indicated by an R^2 value greater than 0.99. The parameters are listed in table 3.4. The number of parameter is reduced to nine, which is sufficient to describe the reaction rates. The reaction orders of methanol, carbon monoxide and water in the reverse water-gas shift reaction tend towards zero and were subsequently omitted.

Table 3.4: Estimated parameters of the power law model: *represents parameterized form.

Parameter*	Value	Asymptotic 95% confidence intervals	Re-parameterized
$\ln(A_{MeOH})$	-25.29	± 1.40	10.04
$E_{a,MeOH}$	-113.13	± 4.42	-113130
$\ln(A_{RWGS})$	-15.90	± 3.30	$7.36{\cdot}10^{9}$
$E_{a,RWGS}$	-158.36	± $1.94{\cdot}10^{1}$	-158360
α_{CO_2}	0.55	± $7.19{\cdot}10^{-2}$	-
α_{H_2}	1.25	± $1.26{\cdot}10^{-1}$	-
α_{H_2O}	-0.70	± $6.36{\cdot}10^{-2}$	-
φ_{H_2}	0.57	± $2.22{\cdot}10^{-1}$	-
ξ	316.75	± $1.99{\cdot}10^{2}$	-

A sensitivity analysis shows that the most influencing parameters on the methanol rate are the order of hydrogen, the order of water and the order of carbon dioxide (figure 3.3). The variation of α_{H_2}, α_{H_2O} and α_{CO_2} was set to 0.1% to ensure linearity in the change of R_{MeOH}. The sensitivity of ξ scales with α_{H_2O}, which is mathematically induced. The order of hydrogen in the reverse water-gas shift rate and ξ have a relatively high confidence interval, however their impact on the rate of methanol formation is relative low (see also figure 3.3).

The equilibrium terms in the methanol synthesis (1-β_{MeOH}) and reverse water-gas shift (1-β_{RWGS}) were evaluated for all reaction conditions at the reactor outlet. While (1-β_{MeOH}) is always close to one (minimum 0.8, average 0.97, standard deviation 0.05), the reverse water-gas shift term mostly lies between -0.5 and +0.5 (average -0.04, standard deviation 0.53). This means the reverse water-gas shift reaction is closer to equilibrium. From a power law kinetic approach, it is hard to distinguish between the driving forces in the reverse water-gas shift reaction. In our approach we implemented the full equation for the reverse water-gas shift reaction, comprising all fugacities of the components in reaction 3.3. Upon such a procedure, the exponents of the fugacities of carbon dioxide, water and carbon monoxide become essentially zero. However, an implementation of just f_{CO_2} instead of f_{H_2} yields essentially the same results, being slightly more inaccurate. Finally, an implementation without f_{CO_2} and f_{H_2} gives also good quantitative agreement between model and simulation, resulting in a R^2 slightly less than for either f_{CO_2} or f_{H_2}. It has to be pointed out that hydrogen and carbon dioxide are almost identically treated *via* the equilibrium term and this term being far away from one under our experimental conditions. Closer to equilibrium the additional

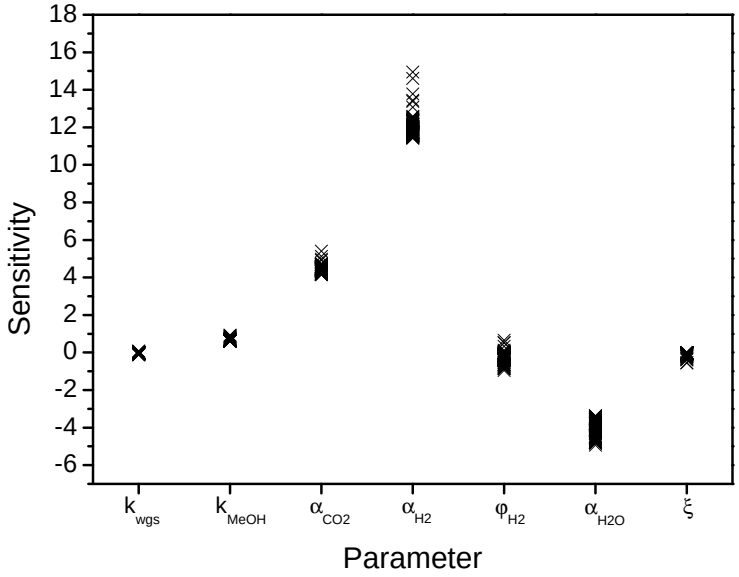

Figure 3.3: Sensitivity plot of the power law model.

influence of a driving force term becomes less important, which makes the determination tough. However, in our modeling f_{H_2} turns out to optimally describe the experimental data.

3.4.2 Langmuir-Hinshelwood-Hougen-Watson model

Vanden Bussche and Froment [59] developed a kinetic model where CO_2 is assumed to be the main carbon source in methanol synthesis. The water-gas shift reaction proceeds *via* a redox mechanism. In contrast to a widely used model by Graaf et al. [58], both hydrogen and carbon dioxide adsorb on the same type of active site. Adsorption of carbon dioxide further leads to carbonate structures, which are hydrogenated *via* intermediates, i.e. formate or methoxy species, yielding methanol in a final step. Under steady state conditions they derived the following kinetic expressions:

$$r_{MeOH} = k'_{MeOH} f_{CO_2} f_{H_2} \left(1 - \beta_{MeOH}\right) / DEN^3 \tag{3.15}$$

$$r_{RWGS} = k_{RWGS} f_{CO_2} \left(1 - \beta_{RWGS}\right) / DEN \tag{3.16}$$

$$DEN = 1 + \frac{K_{H_2O}}{K_8 K_9 K_{H_2}} \frac{f_{H_2O}}{f_{H_2}} + \sqrt{K_{H_2} f_{H_2}} + K_{H_2O} f_{H_2O} \tag{3.17}$$

where k'_{MeOH} is the lumped rate constant for methanol synthesis, k_{RWGS} the rate constant for the reverse water-gas shift reaction and the denominator DEN represents a typical adsorption term in LHHW models, being a function of fugacities and adsorption constants. The rates are reported in $\mathrm{mol \cdot s^{-1} \cdot kg_{cat}^{-1}}$. The driving forces for the methanol synthesis are the fugacities of hydrogen and carbon dioxide, respectively. For the reverse water-gas shift reaction, f_{CO_2} is the driving force, which is based on the theoretical

mechanism. All parameter groups are calculated in Arrhenius form, yielding a set of ten variables:

$$K_i = A_i \cdot \exp\left(\frac{E_i}{RT}\right) \tag{3.18}$$

The values for the kinetic parameters underlay several pseudo-chemical constraints, formulated by Boudart and Djega-Mariadassou [94]: all frequency factors as well as E_i for the adsorption constants have to be positive. For the equilibrium adsorption constants, the frequency factor represents $e^{\Delta S^0/R}$, thus $(-\Delta S^0)$ has to remain positive and should not exceed the entropy of the gas [59]. For the kinetic constants, E_i should be negative within the definition above. However, as k'_{MeOH} and $\frac{K_{H_2O}}{K_8 K_9 K_{H_2}}$ are lumped parameters, they do not underlay these restrictions. Table 3.5 shows the obtained parameters. As can be seen the activation energies satisfy the pseudo-chemical rules by Boudart. The negative changes in entropy of hydrogen and water adsorption $(-\Delta S^0)$ are 13.7 and 99.4 J·mol^{-1}K^{-1}, respectively. The corresponding gas entropies (S^0) are 145 and 207 J·mol^{-1}K^{-1} [59]. The parity between simulation and experiment is comparable to the power law model (figure 3.4). The R^2 value exceeds 0.98.

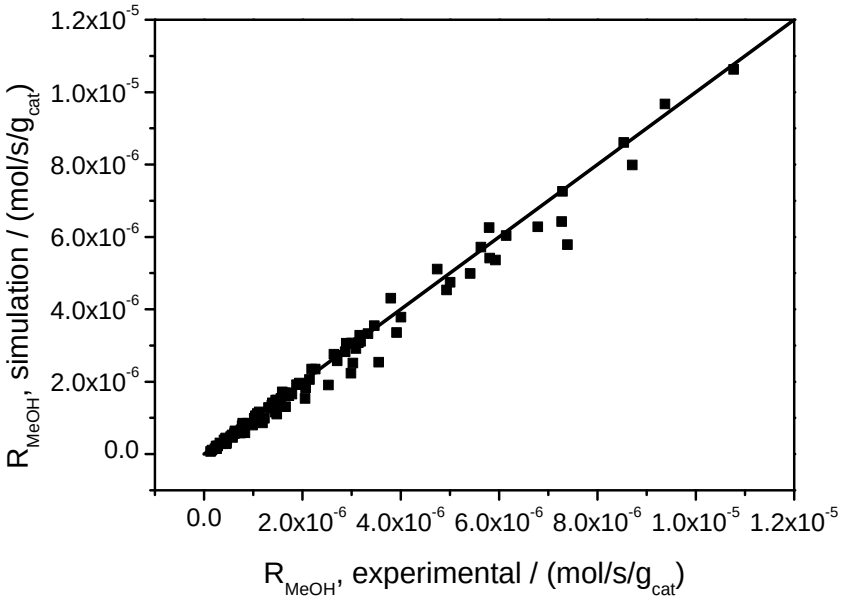

Figure 3.4: Parity plot of the LHHW model.

Figure 3.5 shows the result of the local sensitivity analysis. It can be seen that the highest sensitivity is obtained for the squared hydrogen adsorption constant, followed by the rate constant of methanol synthesis. The adsorption constant of water has the highest relative confidence interval, but its relevance for the rate of methanol formation is very weak.

Table 3.5: Estimated parameters of the LHHW model: *represents parameterized form.

Parameter*	Value	Asymptotic 95% confidence intervals	Re-parameterized
$\ln(A_{MeOH})$	-6.17	± $7.38 \cdot 10^{-1}$	91944
$E_{a,MeOH}$	-72.16	± $1.13 \cdot 10^{1}$	-72161
$\ln(A_{RWGS})$	-7.27	± $4.04 \cdot 10^{-1}$	$4.70 \cdot 10^{14}$
$E_{a,RWGS}$	-168.31	± $2.94 \cdot 10^{1}$	-168310
$\ln(\sqrt{A_{K_{H_2}}})$	-0.82	± $3.61 \cdot 10^{-1}$	0.44
$E_{K_{H_2}}$	-	-	-
$\ln(A_{K_{H_2O}})$	0.35	± 1.50	$6.46 \cdot 10^{-6}$
$E_{K_{H_2O}}$	50.41	± $1.36 \cdot 10^{2}$	50412
$\ln(A_{K_{H_2O}/K_8/K_9/K_{H_2}})$	5.46	± $5.54 \cdot 10^{-1}$	$4.38 \cdot 10^{-5}$
$E_{K_{H_2O}/K_8/K_9/K_{H_2}}$	63.55	± $3.61 \cdot 10^{1}$	63549

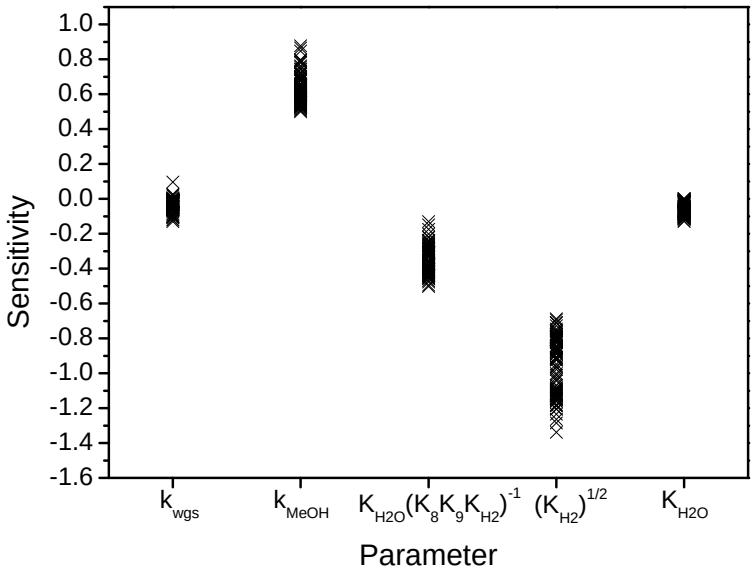

Figure 3.5: Sensitivity plot of the LHHW model.

3.4.3 Microkinetic model

In order to examine the detailed microkinetics, the surface science based model of Ovesen was implemented [13]. Based on their model for the water-gas shift reaction [14], a model for methanol synthesis was explored. Following a redox mechanism, where the educts adsorb on the copper active sites and carbon dioxide is formed by oxidation of adsorbed carbon monoxide, a successive hydrogenation of carbon dioxide leads to methanol. Askgaard et al. [10] presented a model based on single crystal studies, where only Cu(111) facets are considered to be the active surface sites. Ovesen et al. [13] implemented the structure sensitivity of the reaction. The ratio of the exposed copper low-index planes depends dynamically on the gaseous atmosphere, following the Wulff

construction [13]. The gaseous species interact with the Zn-O-Cu interface, leading to oxygen vacancies which have an influence on the particle morphology.

$$H_{2(g)} + Zn{-}O{-}Cu \rightleftharpoons H_2O_{(g)} + Zn - [\ ] - Cu \tag{3.19}$$

$$CO_{(g)} + Zn{-}O{-}Cu \rightleftharpoons CO_{2(g)} + Zn - [\ ] - Cu \tag{3.20}$$

In this work, the Wulff construction is represented using the software package WinX-Morph [70, 71]. Values for the free energy of a free surface from Hansen et al. [28] under hydrogen atmosphere were used, likely being more accurate for syngas conditions with a high ratio of hydrogen. The results are depicted in figure 3.6. They are very similar to the published results by Ovesen et al. [13], where one of the (110) planes of the particle is attached to the substrate. Differences are caused by the choice of the value for the free energy of a free surface, which changes the surface plane distribution of the copper crystal. According to Ovesen et al. [13], the reduction potential and the relative surface contact free energy are related in the following way:

$$\frac{\gamma}{\gamma_0} = \frac{1 - \sqrt{(K_1 \cdot \frac{p_{H_2}}{p_{H_2 0}}) \cdot (K_2 \cdot \frac{p_{CO}}{p_{CO_2}})}}{1 + \sqrt{(K_1 \cdot \frac{p_{H_2}}{p_{H_2 0}}) \cdot (K_2 \cdot \frac{p_{CO}}{p_{CO_2}})}} \tag{3.21}$$

where K_1 and K_2 are the equilibrium constants of the reactions 3.19 and 3.20, respectively.

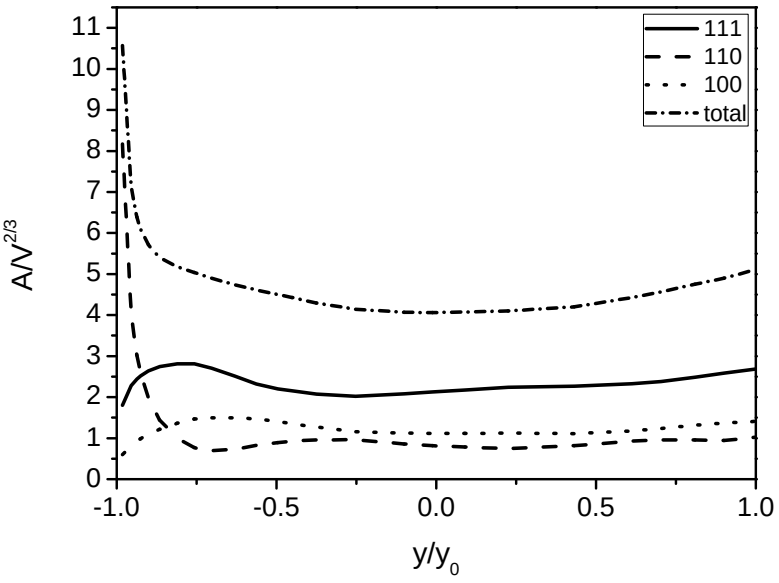

Figure 3.6: Dimensionless surface area, calculated from Wulff construction, Cu(110) attached to the ZnO.

The number of active sites N on the catalysts can then be calculated to be:

$$N = N_0 \frac{\sum_i f_i \, (\gamma/\gamma_0) \cdot D_i}{\sum_j f_j \left((\gamma/\gamma_0)_{fix} \right) \cdot D_j} \tag{3.22}$$

where $f_i(\gamma/\gamma_0)$ is the surface area for (hkl) planes taken from figure 3.6 and D_i is the site density of that plane. N_0 is the number of active sites at fixed conditions, i.e. derived from N_2O frontal chromatography or hydrogen temperature-programmed flow experiments. The ratio of an actual plane compared to the others can be calculated straightforward [13].

When comparing the published thermodynamic data [10–14] for the different species in table 3.1 of the published water-gas shift and the methanol synthesis models, minor differences of the data for the adsorbed species can be found. We analyzed the data in some detail, especially the hydrogen ad- and desorption in temperature-programmed flow experiments [102, 103]. For those reactions, the data taken from the water-gas shift publications [11, 12, 14] were found to be more accurate. However, for the overall methanol synthesis reaction, both data sets yielded good results. Thus, we implemented them in terms of a better description for our (additional) experiments. The rate for methanol synthesis and reverse water-gas shift reaction were implemented according to Askgaard et al. [10]:

$$r_{MeOH,hkl} = k_{11}K_{10}\theta_{HCOO}\theta_H^2/\theta^* - k_{11}/K_{11}\theta_{H_3CO}\theta_O \tag{3.23}$$

$$r_{RWGS,hkl} = k_7/K_7\theta_{CO_2}\theta^* - k_7\theta_{CO}\theta_O \tag{3.24}$$

Hereby k_i represents the kinetic rate constant of the specific reaction and K_i the equilibrium constant of a specific elementary step (see also table 3.1), which can be calculated by the means of statistical thermodynamics. These calculations were discussed in great detail [11, 12, 14]. θ_i is the fractional coverage of a specific species, whereas θ^* is the fractional coverage of free active surface sites. All coverages can be calculated directly by relating the reaction rates of the slow steps (steps 2, 4, 7, 11 in table 3.1) *via* a steady state site balance for adsorbed hydroxyl groups and oxygen and the active site conservation law [10] (see also Appendix). According to Ovesen et al. [13], the overall reaction rate comprises the sum of contributions from the net rate over a specific surface, i.e. Cu(111), Cu(110) or Cu(100):

$$r_{MeOH} = \eta \cdot r_{MeOH,100} + \epsilon \cdot r_{MeOH,110} + (1 - \eta - \epsilon) \cdot r_{MeOH,111} \tag{3.25}$$

$$r_{RWGS} = \eta \cdot r_{RWGS,100} + \epsilon \cdot r_{RWGS,110} + (1 - \eta - \epsilon) \cdot r_{RWGS,111} \tag{3.26}$$

where η is the ratio of sites on Cu(100) relative to the overall active sites and ϵ is the ratio of sites on Cu(110) relative to the overall active sites. From a site balance, the ratio of Cu(111) can be calculated. Expressions for the calculation of η and ϵ are given in the literature [13]. The product of the equilibrium constants for reactions 3.19 and 3.20, and therefore the change in Gibbs free energy is taken from Vesborg et al. [29], being $3.8\,\mathrm{kJ{\cdot}mol^{-1}}$. As mentioned before, the examined catalyst exhibited a specific copper metal surface area of $14.4\,\mathrm{m^2{\cdot}g_{cat}^{-1}}$, which corresponds to 176 $\mu\mathrm{mol{\cdot}g_{cat}^{-1}}$ N_2O consumed. This value was fixed at $\gamma/\gamma_0 = 0.09$, indicated by *in-situ* TEM measurements by Hansen et al. [28] for pure hydrogen atmospheres. This value seems reasonable since similar surface areas were measured by conducting N_2O frontal chromatography and

hydrogen temperature-programmed desorption [77, 97]. For the parameter fitting, the only varying parameter is the rate constant of the slow step during methanol synthesis, namely the hydrogenation of H_2COO_{ads} (step 11 in table 3.1). Ovesen et al. [13] found the rate constants for the rate-determining step on the different surface planes to be related by:

$$k_{MeOH,110} : k_{MeOH,100} : k_{MeOH,111} = 125 : 4.875 : 1 \tag{3.27}$$

In our approach, these ratios have not been changed. As a result, this yields only two variables for the microkinetic model to describe our experimental data, the Arrhenius factor and the activation energy of step 11 in table 3.1, being the rate-determining step. Hereby two Cu sites represent one active site [10]. When considering each Cu site as an active site essentially the same model fit can be derived, with a corresponding difference in k_{11}. Microscopic reversibility was achieved by modeling the reverse rate constant k^- in terms of k^+/K. The result of the parameter fitting, where one of the copper (110) planes of the particle is attached to the substrate, is displayed in figure 3.7, indicating a good qualitative agreement between measured and calculated data. This is also confirmed by a $R^2 > 0.95$. We would like to point out that considering either exclusively Cu(111), Cu(110) or Cu(100) as active sites does not lead to a sufficient model fit. The inclusion of the different exposed surface sites is absolutely necessary for the model to predict the reaction rates adequately.

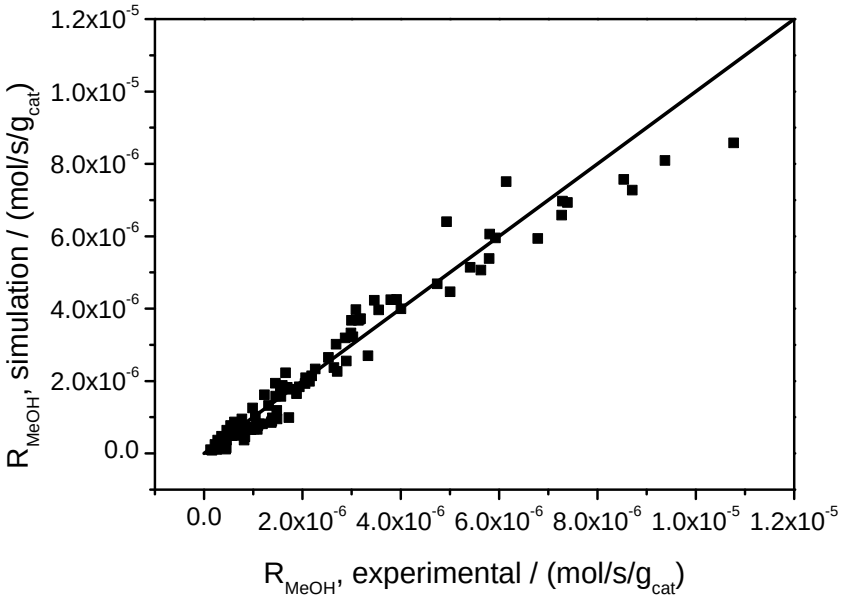

Figure 3.7: Parity plot of the microkinetic model.

The rate constant of methanol synthesis (table 3.6) at the parameterization temperature differs by a factor of 3 between the data deduced from modeling single crystal experiments by Ovesen et al. [13]. However, the deviation is quite reasonable, considering the huge set of input data for the thermodynamic constants, the choice of $(\gamma/\gamma_0)_{fix}$ and the uncertainty of the single crystal experiments [13]. Also, the coverage of intermediates may lead to a shift in the Arrhenius parameters, as the model does not comprise

any coverage-dependence. Modeling single steps of methanol synthesis under ambient pressure suggest coverage-dependencies, i.e. hydrogen desorption or the reaction of carbon monoxide with pre-adsorbed oxygen [103, 104]. The extracted parameters from our high pressure experiments can be seen as effective values at higher coverages compared to the UHV studies.

Table 3.6: Estimated parameters of the microkinetic model: *represents parameterized form.

Parameter*	Value	Asymptotic 95% confidence intervals	Re-parameterized
$\ln(A_{MeOH,111})$	6.03	± $3.59 \cdot 10^{-2}$	$1.93 \cdot 10^{13}$
$E_{a,MeOH,111}$	-100.71	± 3.58	-100710

First, a sensitivity analysis of the static microkinetic model with exclusively Cu(111), Cu(110) or Cu(100) being exposed, after a separate fitting to the experimental data, was conducted. When analyzing all slow steps proposed, i.e. steps 2, 4, 7 and 11, only a few are found to be rate-controlling at the given conditions. For all low-index planes, the hydrogenation of H_2COO_{ads} (step 11) is the rate-limiting step. Step 7 exhibits very slight sensitivities over Cu(111) and Cu(110). This can also be observed when the ratio of the different surfaces is varied depending on the reduction potential of the reactive gas. The result is depicted in figure 3.8.

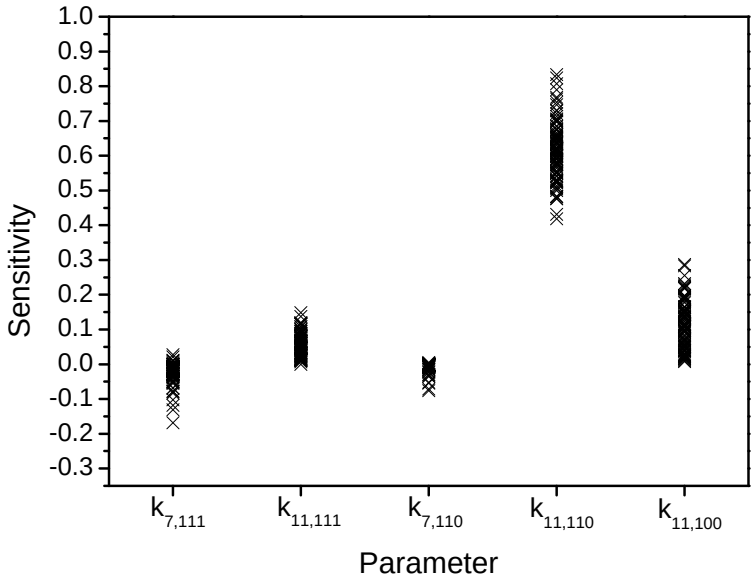

Figure 3.8: Sensitivity plot of the microkinetic model.

As can be seen, step 11 is rate-limiting over Cu(111), Cu(110) and Cu(100). Over Cu(111) and Cu(110) step 7, i.e. the conversion of adsorbed carbon monoxide and oxygen to carbon dioxide, may slightly inhibit the integral reaction rate to methanol. The other investigated steps (step 2 and 4) do not exhibit any sensitivity on the integral rate of methanol formation. The Cu(110) plane has the highest impact on the overall rate, followed by Cu(100). This can be explained by the Wulff construction (figure 3.6).

Under typical reaction conditions, the ratio of exposed facets follows Cu(110) ≤ Cu(100) < Cu(111) (see also fig. 3.11, described later). From single crystal studies it is known that Cu(111) shows the lowest rate constant for the hydrogenation of H_2COO_{ads} (step 11). The reaction rate constant over Cu(110) is approximately 125 times higher than the one over Cu(111) and 26 times higher than over Cu(100) [13]. Although the fraction of exposed Cu(110) is the lowest of all three low-index planes of the catalyst, it turns out to display the highest influence on the overall reaction rate. Particularly step 7 over Cu(111) may be inhibiting. This behavior is always exhibited at low pressures, as the water-gas shift reaction will proceed in the reverse direction, forming water and carbon monoxide. At a high CO-to-CO_2 ratio and pressure, i.e. 2.4 and ≥ 50 bar, the methanol production rate may (slightly) be limited by the CO oxidation to CO_2 over Cu(111) (figure 3.8), indicating that this reaction will preferably proceed over this surface plane. This behavior will be more pronounced at higher conversions . The higher sensitivities for step 7 over Cu(111) can be explained by the rate constant being one magnitude higher than for the other surface planes.

In the following the sensitivities are examined in more detail. Figure 3.9 shows that $S_{k_{11,110}}$ drops significantly with increasing total pressure, whereas $S_{k_{11,100}}$ and $S_{k_{11,111}}$ have the opposite tendency. The sensitivity of $S_{k_{11,111}}$ and $S_{k_{11,100}}$ increase with increasing total pressure. This can again be explained by the Wulff construction, where the ratio of Cu(110) drops with increasing water content (see also figures 3.10 and 3.11, described later). The ratio of Cu(110) becomes less along with the sensitivity of this plane. The inhibiting effect of $k_{7,111}$ and $k_{7,110}$ becomes less at higher total pressures. While at lower total pressure the water-gas shift reaction proceeds in the reverse direction, competing for the methanol synthesis reaction, at higher total pressure the inhibiting effect diminishes, as the water–gas shift reaction tends towards equilibrium or even proceeds in the forward direction to form carbon dioxide and hydrogen.

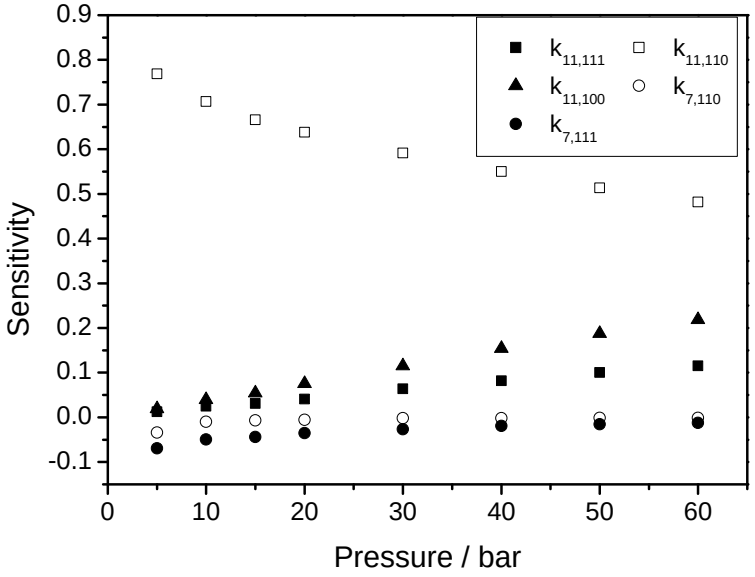

Figure 3.9: Pressure-dependence on sensitivity, T = 463.15 K, standard feed, Q = 100 Nml·min^{-1}.

The valid microkinetic model is used to calculate the change in the Cu surface area during the reaction. The drop in the Cu surface area is mainly attributed to the amount of water produced in the reactor (figure 3.10).

Furthermore, the morphology changes of the copper particles can now be calculated using the microkinetic model (figure 3.11). The relative amount ϵ of Cu(110) sites drops instantaneously when the reaction proceeds and water is produced. Cu(111) becomes the dominant facet and the amount η of Cu(100) sites rises along the reactor length.

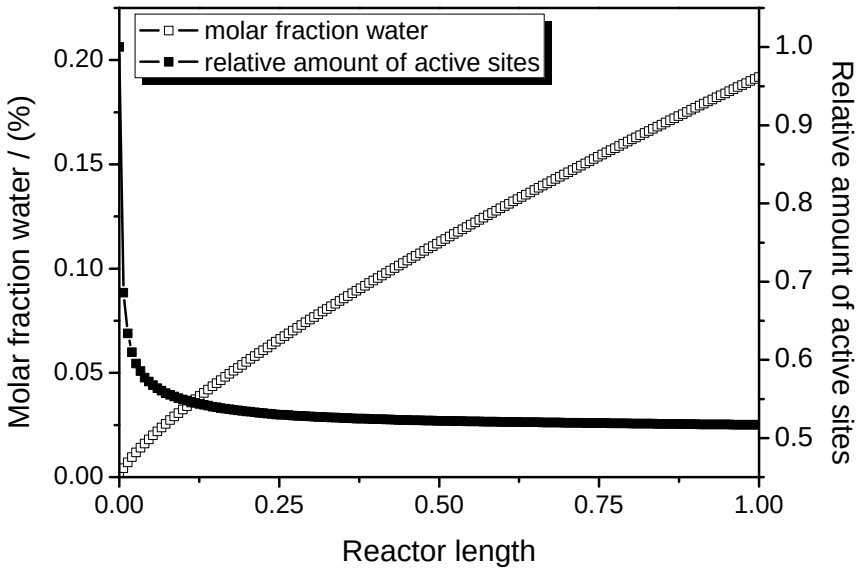

Figure 3.10: Change in Cu surface area along the reactor length, accompanied by the gas-phase water formation, standard feed, T = 463.15 K, p = 50 bar, Q = 100 Nml·min^{-1}.

3.4.4 Comparison of derived models

When comparing the three reaction models, it is obvious that the power law and LHHW models describe the methanol synthesis rate more accurately than the microkinetic model. However, nine (almost) freely varying parameters are fitted to describe the data. The microkinetic model has a lot of restrictions, but two adapted parameters are sufficient to qualitatively describe our data and the data derived by Graaf et al. [10, 13, 58]. The power law and LHHW models are comparable in their predictions, nevertheless the LHHW model has some restrictions which lead to a slight shift for some data points.

The LHHW model has temperature-dependent adsorption terms and follows a redox mechanism [59], comparable to the one proposed by Ovesen et al. [11, 12, 14], which works quite well for both models. Alternatively, the power law model without an inhibiting term for water cannot be fitted to the experimental reaction rates, but performs well using the temperature-independent empirical inhibition factor, which can be explained by the microkinetic model. As water evolves in the reaction, the number of

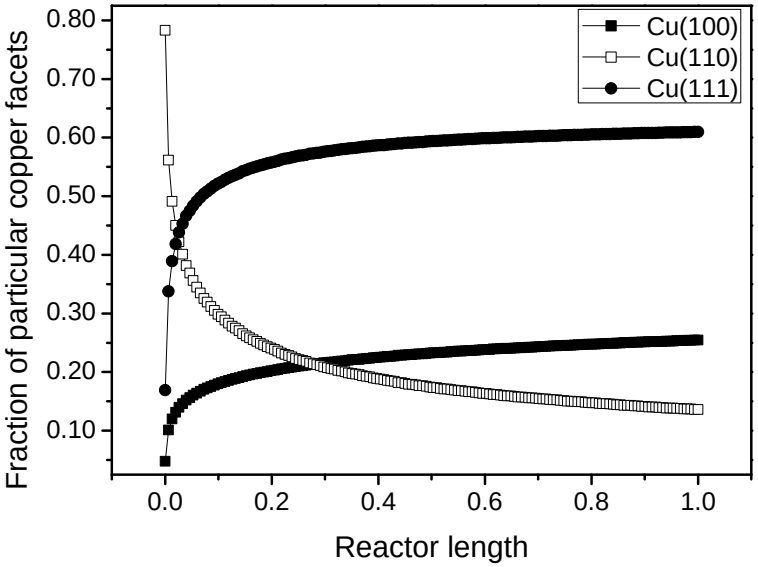

Figure 3.11: Morphology change along the reactor length, standard feed, T = 463.15 K, p = 50 bar, Q = 100 Nml·min^{-1}.

active sites drops significantly and the reaction slows down remarkably (see also figure 3.10). This inhibiting effect of water was also explained by Ovesen et al. [13]. Without such an inhibition term the methanol synthesis cannot be described adequately.

Figure 3.12 shows an extrapolation over a wide temperature range. The calculations have been performed until chemical equilibrium was reached. Also upon extrapolation, the power law and LHHW model predictions are essentially equal. All three models exhibit the highest reaction rate at about 553 K. Due to the thermodynamic influence at higher temperatures all models show a loss in catalytic activity. Besides quantitative reliability of the extrapolation, the microkinetic model proposes lower reaction rates at higher temperatures compared to the global models. Moreover, the change in the total amount of active sites is calculated (figure 3.12, denoted by stars). Particularly the implementation of dynamic morphology changes leads to a more pronounced difference between the microkinetic and global models. Further comparisons are given in the Appendix.

Interestingly the driving force for the reverse water-gas shift reaction is different for both global models. The LHHW model, however, promotes carbon dioxide to be more critical than hydrogen [59]. This may be more accurate for model extrapolations way outside our experimental window, i.e. at completely different reaction conditions. It was already stated that the power law works quite well with either the partial pressure of carbon dioxide or hydrogen as driving force. The presented modeling approach did not yield a reliable distinction, possibly due to the influence of the equilibrium. Hence, for the best model fit the partial pressure of hydrogen was chosen.

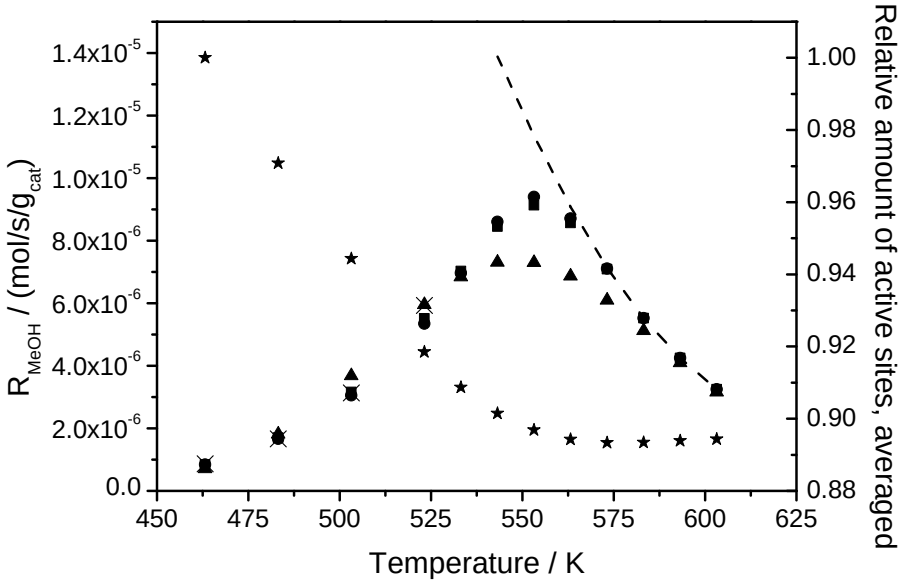

Figure 3.12: Extrapolation of the kinetic models; (x) experimental, ■ power law model, • LHHW model, ▲ microkinetic model, ⋆ averaged relative amount of active sites along the reactor (second axis), dashed line represents integral rate of methanol formation at thermodynamic equilibrium; standard feed, $p = 60\,\text{bar}$, $Q = 100\,\text{Nml}\cdot\text{min}^{-1}$.

3.5 Conclusions

Three different models for describing data for the methanol synthesis were presented. All models are found to be valid in the experimental window and predict the rate of methanol synthesis correctly. The power law model, which has no restrictions concerning the model parameters and the pseudo-mechanistically Langmuir-Hinshelwood-Hougen-Watson model yield a good fit to the respective data. Care should be taken when a power law is used to describe the measurements, as there are several possibilities to fit the data. The explicit microkinetic model can describe the experiments adequately, even by varying only two parameters. The global models are more accurate in predicting the kinetics in the evaluated experimental parameter space and can therefore be used for reactor modeling, i.e. concerning diffusion limitations during methanol synthesis, while the microkinetic model includes morphology changes, which are very important during methanol synthesis and are still subject of further investigations [13, 28, 29]. Morphology changes can also be induced by adsorption of oxidizing or reducing components, which change the surface free energy and may additionally change the strain in the copper particles. Additional high-pressure *in-situ* studies have to be carried out to show further synergy effects of ZnO and copper, i.e. zinc dissolved in the copper particles or Cu-O-Zn species [23, 49], which is presently not included in the microkinetic model. Furthermore, research is recommended regarding the coverage-dependence of the particular intermediates to improve the model and to study a possible inhibition of specific species.

4 Theoretical investigation of catalyst deactivation during methanol synthesis using a microkinetic model

4.1 Abstract

The $Cu/ZnO/Al_2O_3$ catalyst used for industrial methanol synthesis shows remarkable deactivation with increasing time on stream. In this work, the loss in activity is theoretically studied by a microkinetic model. This model considers sintering and furthermore irreversible catalyst morphology changes for catalyst deactivation. These changes in the morphology may be induced by adsorbed species or surface intermediates. It is shown that this may explain the dramatic loss in activity during the first hours of operation. Additionally, the irreversible changes could explain the pronounced difference in deactivation between differently reducing feed gases found in literature.

4.2 Introduction

On industrial scale the catalyst lifetime of a $Cu/ZnO/Al_2O_3$ catalyst is usually several years. Before reaction the catalysts oxides are reduced in a diluted hydrogen atmosphere [18]. After this treatment methanol synthesis is started, however, the catalytic activity drops with time on stream. There exist several studies about catalyst deactivation and its origin [30, 35, 60, 105]. Hereby, deactivation is mainly attributed to catalyst poisoning and sintering effects. Catalyst poisoning is mainly a problem when syngas is made from coal. However, the site blocking effects are mostly suppressed by very low sulfur and chloride concentrations in typical synthesis gas, which are the main catalysts poisons for the ternary catalyst [18]. These low levels of impurities are achieved by today's very efficient gas purifying. Hence, sintering of copper particles may be the main source for catalyst deactivation, leading to a lower dispersion and less active sites due to coarsening of copper crystallites. This was particularly reported by several research groups [35, 52, 106], also for temperatures below the Tammann temperature. The Tammann temperature is taken as a general approximation at which agglomerates may start migrating. It is defined as half of the melting temperature, hence copper should not significantly sinter as its Tammann temperature is 670 K [30]. Besides, the other components like alumina and zinc oxide should further enhance the thermal stability of the catalyst. The extent of sintering was also attributed to the feed gas employed in the synthesis reaction [35, 105]. Water can be formed *via* the hydrogenation of carbon dioxide or the reverse water-gas shift reaction and may

enhance sintering effects [35]. Furthermore, CO-rich feeds were found to underlay a severe activity loss [105]. This was suggested to be related to an over-reduction of copper and zinc oxide, which increases the mobility of copper crystallites. Finally, it was proposed that highly reducing gases may lead to alloy formation [26, 27, 50]. Structural changes were found using *in-situ* methods such as FTIR, EXAFS or TEM [24–29]. However, these effects were further related to the synthesis activity and should enhance the methanol formation rate due to these SMSI effects [13, 29, 41]. The reversible changes were usually determined under very low pressure and only for model systems, thus one may suspect that adsorption of reducing or oxidizing components under high pressure may lead to further (irreversible) changes of the particle morphology. In this chapter a theoretical approach is presented for the deactivation of a copper zinc oxide catalyst for methanol synthesis using a microkinetic model [13, 107]. First, the effect of a decrease in the number of active sites on the methanol and water formation rate is studied. Furthermore, a deactivation mechanism based on sintering effects as well as on irreversible morphology changes due to adsorption of educts and surface intermediates is introduced. Hereby, irreversible changes in the catalysts morphology are considered as an additional deactivation mechanism, which may further enhance the decrease in catalytic activity.

4.3 Modeling

Similar to a previous study [107], the species model equations were implemented as an ideal plug flow reactor model:

$$\frac{\partial n_i}{\partial t} = \sum_{j=1}^{2} \left(\lambda_{ij} r_j\right) N_{cat} - \frac{\partial \dot{n}_i}{\partial z} \qquad i = 1, ..., 5 \tag{4.1}$$

where $\dot{n}_i$ is the molar flow of a gas-phase species in mol·s^{-1}, $\lambda_{ij} r_j$ the product of the stoichiometric coefficient and the reaction rate in s^{-1} and N_{cat} the amount of active sites in mol. Hereby, it is assumed that methanol is formed *via* the hydrogenation of carbon dioxide ($j = 1$) and the latter can also react *via* the reverse water-gas shift reaction ($j = 2$), respectively:

$$CO_2 + 3\,H_2 \rightleftharpoons CH_3OH + H_2O \qquad j = 1 \tag{4.2}$$

$$CO_2 + H_2 \rightleftharpoons CO + H_2O \qquad j = 2 \tag{4.3}$$

The microkinetic model by Ovesen et al. [13] is implemented, which captures the general kinetics of the methanol synthesis under industrial conditions [13, 107]. This model is based on 13 elementary steps over the three different copper low-index planes 111, 110 and 100. Furthermore, the model comprises morphology changes [24, 25, 28, 29], with a gas dependent number of active sites and copper plane distribution. Hence, it is possible to relate deactivation effects directly to the catalytically active copper surface. According to Ovesen et al. [13], the dynamic morphology changes of the catalyst are a

function of the reduction potential of the reactive gas atmosphere. In order to account for possible (irreversible) effects of adsorbates and intermediates on the morphology of the catalyst, additionally a reduction potential dependent term is introduced:

$$\begin{aligned}\frac{\gamma}{\gamma_0} &= \frac{1-\sqrt{(K_1\cdot\frac{p_{H_2}}{p_{H_20}})\cdot(K_2\cdot\frac{p_{CO}}{p_{CO_2}})}}{1+\sqrt{(K_1\cdot\frac{p_{H_2}}{p_{H_20}})\cdot(K_2\cdot\frac{p_{CO}}{p_{CO_2}})}} \\ &+\psi\cdot\frac{p_{CO_2}p_{H_2O}}{p_{H_2}p_{CO}}\left(\frac{p_{H_2}p_{CO}}{p_{CO_2}p_{H_2O}}\right)_{fix(z=1,t=t_{end})}\cdot\left[1-\exp\left(-\tilde{t}\right)\right]\end{aligned} \tag{4.4}$$

In here, $\frac{\gamma}{\gamma_0}$ is the relative surface free energy between the copper crystallite and the substrate and K_i the equilibrium constant for the reduction of the Zn-O-Cu interface by hydrogen and carbon monoxide, respectively [13]:

$$\mathrm{H_{2(g)}} + \mathrm{Zn{-}O{-}Cu} \rightleftharpoons \mathrm{H_2O_{(g)}} + \mathrm{Zn-[\ ]-Cu} \tag{4.5}$$

$$\mathrm{CO_{(g)}} + \mathrm{Zn{-}O{-}Cu} \rightleftharpoons \mathrm{CO_{2(g)}} + \mathrm{Zn-[\ ]-Cu} \tag{4.6}$$

Besides, ψ represents the total change in $\frac{\gamma}{\gamma_0}$ at an oxidation potential of $\frac{p_{CO_2}p_{H_2O}}{p_{H_2}p_{CO}}$ at fixed conditions ($z=1, t=t_{end}$) and a dimensionless time $\tilde{t}$ (see also table 4.1). As a result, the irreversible changes in the catalyst morphology rise with increasing oxidation potential in the gas phase and time, until the final value, ψ, is reached. In order to model the deactivation of the copper catalyst, sintering is considered analogous to Løvik [30]:

$$\frac{\partial s}{\partial t} = -A_d\cdot\exp\left[\frac{-E_d}{R}\cdot\left(\frac{1}{T}-\frac{1}{T_0}\right)\right]\cdot s(t)^5 \tag{4.7}$$

where s describes the change in activity of the catalyst caused by sintering and A_d and E_d are the Arrhenius factor and the activation energy of deactivation. This formula was based on a model presented by Skrzypek et al. [51] and extended by the temperature-dependence, as a higher temperature may enhance agglomeration effects [30]. As sintering induces a reduction of active sites, the activity s is directly related to the number of active sites. The relative surface free energy can further be based on the equilibrium shape of a copper crystal, obtained by the Wulff construction [13]. This yields an extended equation for the number of active sites, which is directly related to sintering:

$$N_{cat} = N_0\cdot s\cdot\frac{\sum f_{hkl}\left(\gamma/\gamma_0\right)\cdot D_{hkl}}{\sum f_{hkl}\left(\left(\gamma/\gamma_0\right)_{fixed}\right)\cdot D_{hkl}} \tag{4.8}$$

where N_0 is the number of active sites in mol at fixed conditions, $f_i\left(\gamma/\gamma_0\right)$ the dimensionless area for a specific copper low-index plane, Cu(111), Cu(110) or Cu(100), taken from figure 4.1 and D the site density of such a specific plane. Furthermore, the proportion of each surface plane on the overall amount of active sites can be calculated

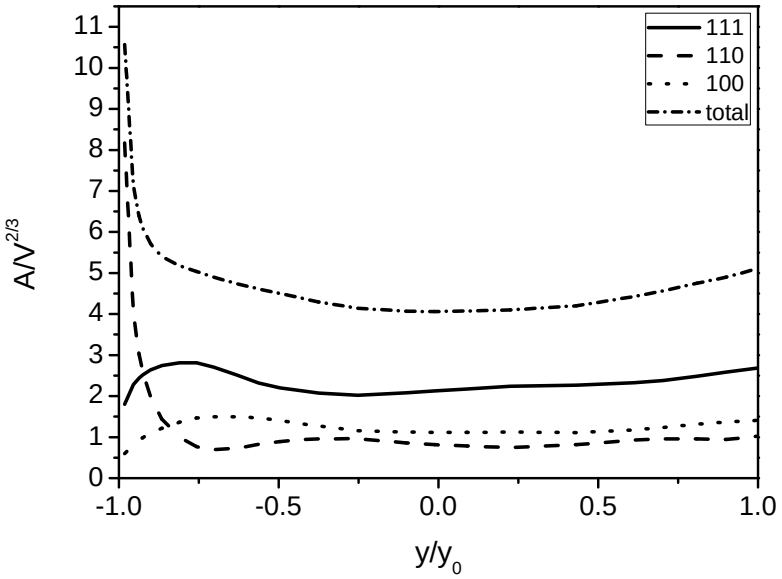

Figure 4.1: Dimensionless surface area $A/V^{2/3}$ vs. γ/γ_0, assuming that one of the Cu(110) planes is attached to the substrate [107].

straightforward and depends on the gas atmosphere [13]. Løvik [30] introduced a relative activity $\left[1 - \frac{s_0 - s}{s_0}\right]$ for $s\,(t = 0\,\mathrm{s}) = s_0 = 0.4$ in order to exclude the initial fast deactivation. Closer analysis shows that this expression directly scales with A_d and does not influence the results of this study and is hence omitted in our calculations.

The system of partial differential equations was solved using the Athena Visual Studio engineering software [73]. The reactor coordinate was discretized by finite differences using a central difference scheme with 200 grid points. Time-dependent differential equations were solved by the Athena built-in differential equation solver. Tolerances were set to a value of 10^{-8}. Furthermore, when it is assumed that the kinetics is way faster than the deactivation, equation 4.1 can safely assumed to be in steady state $\left(\frac{\partial n_i}{\partial t} = 0\right)$ and hence is only a function of time according to $N_{cat} = N_{cat}\,(t)$.

A pressure of 60 bar and a temperature of 463 or 523 K were chosen as standard reaction conditions. In addition, two feed gas compositions were selected for the model discussion, i.e. a feed with a high CO-to-CO_2 ratio of 2.5 and an intermediate ratio of 0.75. Important process parameters are listed in table 4.1. A reduction in methanol activity of 40% within 28 days for feed 1 is considered. The initial surface area of 28 $m^2 \cdot g_{cat}^{-1}$ (342 $\mu mol \cdot g_{cat}^{-1}$) was fixed at $\frac{\gamma}{\gamma_0} = 0.09$ (see reference [107]). The proposed deactivation was achieved by adjusting the factor A_d in equation 4.7, as suggested by Løvik [30]. The respective reactor dimensions and reaction rate equations and respective input data are analogous to a previous study [107].

Table 4.1: Deactivation model parameter.

Feed 1	10% CO, 4% CO_2, 72% H_2, 14% inert
Feed 2	6% CO, 8% CO_2, 72% H_2, 14% inert
T / K	463, 523
T_0 / K [30]	513
Pressure / bar	60
Initial surface area / $m^2 \cdot g_{cat}^{-1}$	28*
Loss in methanol activity (feed 1) / %	40
Deactivation time (t_{end}) / h	670
A_d (according to model case) / s^{-1}	$2.5 \cdot 10^{-7}$, $1.3 \cdot 10^{-6}$
E_d / $J \cdot mol^{-1}$ [30]	91270
ψ	0.3
$\tilde{t}$	t / 100 h

* measured by Reactive Frontal Chromatography (N_2O RFC).

4.4 Results and discussion

The effect of a possible decrease in initial copper surface area is displayed in figure 4.2. The feed comprises a CO-to-CO_2 ratio of 2.5. In here, the Cu surface area is decreased in steps of 10% until 40% of the initial value is reached.

It can be seen that the methanol activity almost linearly depends on the copper surface area (inset of figure 4.2). This is consistent with experimental results [39–42]. Furthermore, it is quite interesting that the loss in the rate of methanol formation is less than the respective change in Cu surface area, even for the kinetically controlled regime considered here. Thus, this behavior is also observed for very low conversions, but not exhibited for a static microkinetic model with only Cu(111) planes as active sites. Hence, this effect can be attributed in the present model to the structure sensitivity of different copper low-index planes, Cu(100), Cu(110) and Cu(111). When the Cu surface area is decreased, less water is produced and hence the relative surface free energy $\frac{\gamma}{\gamma_0}$ is shifted to lower values (see also figure 4.1). This increases the active surface area in the reactor and also the relative amount of the crystal planes attached to the substrate, being Cu(110) in our example ([107]). As Cu(110) comprises the highest rate for methanol formation [13] the loss in active sites can be compensated to some extent. The activity of water formation is somehow less affected by the decrease in copper atoms, since this rate is not only dependent on the methanol synthesis (reaction 4.2), but also on the reverse water-gas shift reaction (reaction 4.3). Under our conditions the water-gas shift reaction proceeds in the forward direction and hence lowers the amount of water formed. A decrease in active sites will therefore also lead to less water

removed through the CO conversion. At higher temperatures (not shown in figure 4.2), the relative change in water formation is even less, since at those temperatures the integral rate of water formation is close to equilibrium.

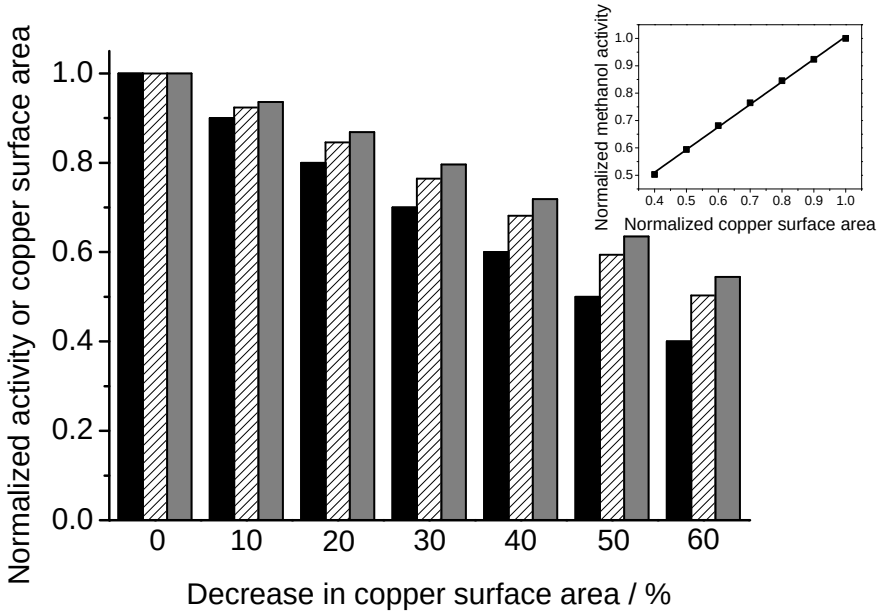

Figure 4.2: Effect of a decrease in copper surface area (black) on the activity of methanol (shaded) and water (grey) formation. Simulations at $T = 463\,\mathrm{K}$ and $p = 60\,\mathrm{bar}$, CO-rich feed.

The effect of sintering and possible irreversible morphology changes is depicted in figure 4.3. Hereby, feed gas compositions of high and intermediate CO-to-CO_2 ratios are considered. From experimental results it is expected that during the first hours the decrease in activity follows an exponential behavior and levels off after some hours on stream [35, 44, 105, 108]. Furthermore, for a CO-rich feed a more pronounced deactivation was observed [105].

The dashed line displays the trend of deactivation for a feed gas comprising a ratio of $\frac{p_{CO}}{p_{CO_2}} = 2.5$, when only sintering of the copper particles is considered. To reach a decrease in methanol activity of 40%, A_d was set to a value of $1.3{\cdot}10^{-6}\,\mathrm{s^{-1}}$. It can be seen that the progress of deactivation in the beginning is incremental and levels off towards 670 h. However, steeper slopes at the beginning of the deactivation are expected [44]. Here, a possible explanation could be the change of the relative surface free energy due to adsorbates or formed intermediates during reaction, which might compensate the proposed over-reduction of the catalyst [105]. To account for the possible morphology changes an increase of $\psi = 0.3$ in the relative surface free energy is assumed. This is approximately the difference in the average of $\frac{\gamma}{\gamma_0}$ along the reactor coordinate between the two feeds considered here (table 4.1). It is further assumed that these changes are a function of the oxidation potential. Moreover, these changes are considered as fully achieved at the reactor outlet after 670 h:

$$\frac{p_{CO_2} p_{H_2O}}{p_{H_2} p_{CO}} = \left(\frac{p_{CO_2} p_{H_2O}}{p_{H_2} p_{CO}} \right)_{fix(z=1, t=t_{end})} \tag{4.9}$$

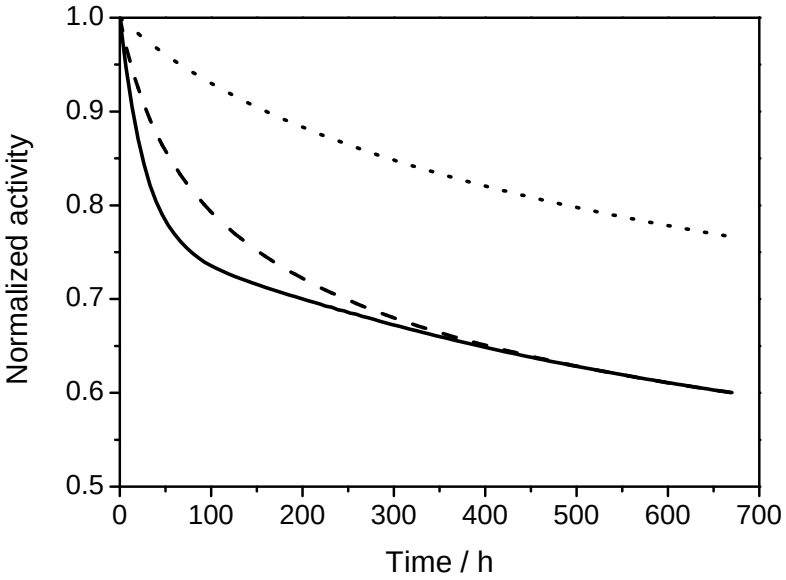

Figure 4.3: Deactivation behavior of the CO-rich feed solely sintering (dashed line) and sintering including irreversible morphology changes (solid line), as well as calculated deactivation behavior for the CO_2-rich feed (dotted line). Simulations performed for standard conditions, i.e. at $T = 523\,\mathrm{K}$ and $p = 60\,\mathrm{bar}$.

The exponential term, $\left[1 - \exp\left(-\tilde{t}\right)\right]$, is included to account for a higher driving force of morphology changes in the first few hours, when the catalyst is fresh. The Arrhenius factor of deactivation yields $2.5{\cdot}10^{-7}\,\mathrm{s}^{-1}$. The inclusion of such an approach (figure 4.3, solid line) reflects the experimental results from Kurtz et al. [44] better. The activity drops faster at the beginning and becomes more stable after the first hours. From then on it is assumed that the catalyst is stabilized and hence both resulting slopes from solely sintering and sintering including morphology changes level off. Deactivation regarding irreversible changes is also possible when other Cu surfaces are attached to the substrate. When it is further assumed that the irreversible changes are negligible for a feed with a low CO-to-CO_2 ratio and only sintering processes occur (figure 4.3, dotted line), quite a good agreement with the results from Sun et al. [105] is obtained. This might be the case when the increased amount of CO_2 stabilizes the catalysts morphology. A pronounced deactivation of feeds containing a large amount of carbon monoxide was observed, which was dedicated to over-reduction of the catalyst and further related to enhance sintering of the copper particles. In figure 4.3, the deactivation of the CO_2-rich feed gas shows a less pronounced loss in activity compared to the CO-rich feed, as the latter induces irreversible catalyst morphology changes.

The deactivation approach including irreversible morphology changes may be explained as follows: Methanol is formed through CO_2 hydrogenation. This means for feeds with low CO-to-CO_2 ratios that higher rates for methanol formation in comparison with high CO-to-CO_2 ratios are expected. However, a positive reaction order for CO has been found, which was later explained as a promotional effect [13, 58, 60]. As a result it induces a higher active surface area and an increased amount of the most active

copper planes, namely Cu(110) [13]. This over-reduction of the catalyst is not stable when oxidizing species adsorb on the surface or surface intermediates evolve. Hence, the promoting effect of CO becomes less, leading to a pronounced initial deactivation. A catalyst treated with a feed gas comprising a high amount of CO_2 on the other hand may be stable or less dependent on such effects, which leads to sintering as the most probable deactivation phenomenon. It should be pointed out that this explanation does not include a possible influence on high water or CO_2 content on the sintering mechanism, since sintering is decoupled from the irreversible morphology changes in this work.

4.5 Conclusions

The effect of a possible decrease in active sites was studied using a microkinetic model. For a typical feed gas, comprising a CO-to-CO_2 ratio of 2.5 methanol formation is more affected by changes in the copper surface area than the rate of water formation as the water is removed *via* the simultaneously occurring water-gas shift reaction. Additionally, the activity for methanol is linear dependent on the decrease in copper surface area, however, the proportionality factor does not equal one, since the catalyst underlies dynamical changes which are able to compensate some deactivation.

The qualitative agreement between model and experiment in the first few hours on stream was significantly improved by introducing catalyst irreversible morphology changes, which may be induced by adsorbates or surface intermediates. The inclusion of a gas-dependent factor for such processes clearly improves the model description. Additionally, when comparing a CO-rich and a feed with an intermediate CO-to-CO_2 ratio, the differences in deactivation could be explained in that manner, as the over-reduction of the catalyst by employing CO-rich feeds may be irreversibly decreased by oxidizing adsorbates and surface intermediates. However, the influencing parameters are only approximated and furthermore not directly related to specific surface species but only to the oxidation potential of the reaction gas. Further research concerning adsorption and re-structuring under high pressures is highly recommended, which also includes sintering mechanisms and the density of lattice defects and strain [21, 22]. The effects of the different gas atmospheres also need to be investigated, especially relating to their impact on sintering.

5 Modeling of temperature-programmed desorption (TPD) flow experiments from $Cu/ZnO/Al_2O_3$ catalysts

5.1 Abstract

Different procedures to extract the kinetics of hydrogen desorption from a $Cu/ZnO/Al_2O_3$ catalyst for methanol synthesis were studied by performing temperature-programmed desorption (TPD) experiments under atmospheric pressure. The four methods include i) heating rate variation, ii) analysis using a fixed pre-exponential factor, iii) lineshape analysis and iv) full analysis. Before extracting the parameters, transport limitations could be excluded for all experiments and a criterion for inner particle mass transfer limitations could be extended in the case of activated re-adsorption. All methods could be valid in the whole range of experiments, with only one exception for the lineshape analysis at full coverage of hydrogen. However, each method requires different input to extract physically meaningful parameters. The best modeling results were obtained when repulsive interactions of adsorbed species were accounted for. This led to a $k_{des} = 3.75{\cdot}10^{10}\,\mathrm{s^{-1}}{\cdot}\exp(-(75\,\mathrm{kJ{\cdot}mol^{-1}} - 5.5\,\mathrm{kJ{\cdot}mol^{-1}} \cdot \theta_H^{2.6})/RT)$ in good agreement with the literature. Moreover, it was found that there is no difference, when extracting the kinetic parameters from a fresh or deactivated catalyst at full coverage.

5.2 Introduction

Temperature-programmed techniques are widely used in surface science studies in order to extract kinetic parameters. Routinely, thermal desorption spectroscopy (TDS) under ultra-high vacuum (UHV) conditions is applied to determine kinetic information from well-defined single crystals. This is a straightforward way to analyze the kinetic properties, since effects like re-adsorption or mass transfer limitations are negligible [109]. However, such well-defined surfaces and ideal conditions may have a lack of applicability to working conditions due to the big *pressure* and *material gaps*. Modern flow set-ups work under ambient pressure and are suited for studying microkinetics (in terms of elementary steps) on porous catalysts close to reaction conditions [2, 80]. In particular, concentration-programmed experiments, e.g. pulse and step function or switch experiments, and temperature-programmed flow experiments, e.g. performed

as TP desorption (TPD) or adsorption (TPA) experiment, are frequently used in microkinetic studies of heterogeneously catalyzed gas-phase reactions [78, 79, 110].

In general, several mathematical procedures exist for the evaluation of kinetic parameters of temperature-programmed experiments, resulting in terms of Arrhenius parameters for the rate constants, i.e. A_{ads}, A_{des}, E_{ads}, E_{des}. In general, the methods can be divided into two groups: (a) the integral approach which relates the kinetic parameters to desorption characteristics such as full width at half maximum (FWHM) and temperatures at peak maximum; (b) differential analyses of the desorption spectra resulting in pairs of desorption rate/temperature. While the integral approach is applied to extract coverage-independent kinetic parameters, differential techniques are used to obtain a coverage-dependence of the kinetic parameters.

In order to test different approaches to extract kinetic parameters, hydrogen desorption from Cu-based ternary ($Cu/ZnO/Al_2O_3$) catalysts employed in methanol synthesis was studied. This has been a subject of great interest during the last decade [41, 77, 102, 111–114]. It was clearly demonstrated that hydrogen recombinatively desorbs from copper surface sites. Furthermore, these metallic copper sites have been identified as the active sites for methanol synthesis [39, 40]. From UHV studies it is known that hydrogen adsorption on copper single crystals proceeds *via* dissociation and is regarded to be highly activated. Similarly, this was demonstrated also for ternary copper catalyst [102, 113, 115–118]. Since re-adsorption is less or even negligible when adsorption is a highly activated process, interpretation of the flow TP desorption data are less demanding and desorption can be studied separately. Simple transient experiments such as the variation of the heating rate at constant initial coverage have been carried out to determine the desorption kinetics in detail followed also by a simple evaluation method to describe the desorption process in term of Arrhenius parameters [102, 112]. However, more advanced methods can be applied, which, in turn, require experimental TPD spectra obtained with different initial coverages at the same heating rate [111, 113]. The determination of the kinetic parameters was not the only subject of interest. Muhler et al. [77] developed a method to determine the copper surface area of binary Cu/Al_2O_3 and ternary $Cu/ZnO/Al_2O_3$ catalysts *via* H_2 TPD flow experiments, which is, compared to the widely used N_2O frontal chromatography [96, 98], non destructive. Wilmer et al. [41, 102] studied the interaction of hydrogen with ZnO-containing copper and Cu/Al_2O_3 catalysts in detail. They found that a pre-treatment in a mild atmosphere (He) prior to hydrogen desorption experiments leads to almost similar kinetic values for the catalysts, indicating that there is only a slight influence by ZnO on the copper sites and Al_2O_3 mainly acting as a structural promoter. However, when changing the pre-treatment procedure to more severe conditions, in particular to a pre-treatment with carbon monoxide, hydrogen desorption spectra change in shape and peak positions. Experiments indicate morphology changes or even surface alloying under highly reducing conditions [41, 102].

In previous flow TPD studies, only coverage-independent desorption parameters assuming ideal Langmuirian behavior were extracted for modeling the interaction of hydrogen with Cu-based catalysts employed in methanol synthesis [102, 112]. In

general, this approach results in modeled signals being too narrow at full coverage. The reason for that is mainly due to neglecting adsorbate-adsorbate and adsorbate-substrate interactions [102]. Moreover, diffusion limitations could possibly broaden the signals measured at the reactor outlet flow. In this study a valuable criterion for diffusion limitations was adapted and reconsidered in the case of activated re-adsorption [81]. This work compares different methods to receive kinetic parameters from TPD experiments. It is shown that numerical methods such as non linear least-squares fitting can describe TPD experiments more adequately than the present evaluation of heating rate variation, while using physical meaningful input parameters from experimental analysis. A coverage-dependent activation energy leads to even better results than previously extracted ones neglecting a coverage-dependence.

5.3 Experimental and computational section

In our study, the H_2 TPD experiments were carried out in a completely glass-coated stainless steel set-up. Only gases of high purity ($> 99.9995\%$) were used. Fast on-line analysis of the gas components was achieved by a calibrated quadrupole mass spectrometer (Balzers GAM 422). The H_2 TPD experiments were measured using an industrial $Cu/ZnO/Al_2O_3$ catalyst, of which 200 mg (sieve fraction 250 - 355 μm) were filled into a single-pass fixed-bed reactor. Details on the set-up can be found elsewhere [82, 112].

In order to achieve different hydrogen coverages θ_H, on the one hand the dosing temperature can be varied; on the other hand the dosing duration might be varied. In addition to these two experimental procedures the H_2 TPD experiments can be stopped at different temperatures to achieve the desired hydrogen coverage. This was achieved by quenching the outside of the reactor with liquid N_2. Subsequently a second temperature ramp was initialized. Using this method, the desired coverages can be obtained very exactly. Comparison of this procedure with the ones mentioned before showed only negligible differences [82, 112].

The results for the heating rate variations were taken from previous work by Wilmer et al. [102]. Prior to the TPD experiments methanol synthesis was performed over night. This procedure led to a reduced number of active sites. This evidence will be discussed later in more detail.

The fixed-bed reactor was modeled as a continuously stirred-tank reactor (CSTR), a plug flow reactor (PFR) and a convection-axial dispersion reactor model (C-ADR), respectively. Also intraparticle mass transfer was investigated. The governing equations for the CSTR, PFR and C-ADR are given as [81]:

$$\frac{\partial c_{H_2}}{\partial t} = -\frac{1}{\tau(t)}\, c_{H_2} + \gamma \tag{5.1}$$

$$\frac{\partial c_{H_2}}{\partial t} = -\frac{u(t)}{L\epsilon_b}\, \frac{\partial c_{H_2}}{\partial x} + \gamma \tag{5.2}$$

$$\frac{\partial c_{H_2}}{\partial t} = \frac{D_{ax}}{L^2\ \epsilon_b}\ \frac{\partial^2 c_{H_2}}{\partial x^2} -\ \frac{u(t)}{L\epsilon_b}\ \frac{\partial c_{H_2}}{\partial x} + \gamma \tag{5.3}$$

where γ without intraparticle particle mass transfer is defined as:

$$\gamma = \frac{(1-\epsilon_b)\rho_p N_{H_2,sat}}{\epsilon_b}\left(-\ \frac{\partial \theta_H}{\partial t}\right) \tag{5.4}$$

and

$$\gamma_{IPMT} = -\ \frac{3D_e(1-\epsilon_b)}{r_p^2\epsilon_b}\frac{\partial c_{H_2}}{\partial z}\Big|_{z=1} \tag{5.5}$$

when considering intraparticle mass transfer. The corresponding particle balance is given by:

$$\frac{\partial c_{H_2}}{\partial t} = \frac{D_e}{r_p^2\epsilon_p}\left(\frac{\partial^2 c_{H_2}}{\partial z^2} + \frac{2}{z}\frac{\partial c_{H_2}}{\partial z}\right) + \frac{\rho_p N_{H_2,sat}}{\epsilon_p}\left(-\ \frac{\partial \theta_H}{\partial t}\right) \tag{5.6}$$

A time-dependent balance for adsorbed species was used, assuming a one-step mechanism, as there is no evidence for molecularly adsorbed hydrogen from experiments on Cu surfaces:

$$\mathrm{H_2}\ +\ 2\,^* \rightleftharpoons 2\,\mathrm{H}^* \tag{5.7}$$

The corresponding differential equation yields:

$$\frac{\partial \theta_H}{\partial t} = 2\cdot\left(k_{ads}p_{H_2}(1-\theta_H)^2 - k_{des}\theta_H^2\right) \tag{5.8}$$

Differential equations were solved with a sparse system adaptive ODE solver “ode15s”, using Mathworks Inc. MATLAB® R2009b. Tolerances were set to a value of 10^{-8}. Partial differential equations were discretized by the method of lines [74]. For the models without inner particle mass transfer at least 100 equidistant grid points and for all other models 40 grid points in reactor and particle coordinate were used. Backward differences were used to describe the reactor system. Second order derivatives, i.e. diffusion related, were calculated by a central difference scheme. All spectra were tested against numerical convergence and mass conservation. For fittings, the MATLAB® non linear least-squares fitting function “lsqnonlin” was implemented. The termination tolerance on the function value was chosen to be 10^{-15}. Detection by a quadrupole mass spectrometer provides very sensitive data analysis. Consequently, a thorough data reduction was applied for further modeling aspects. A well defined temperature interval was chosen, containing all relevant information, i.e. from the onset to the ending of the signal of hydrogen. In order to reduce the experimental noise the number of data points was decreased by a factor of 20. Besides this, the position of the signal maxima is also included to the objective function. An alternative way of data reduction is a fit around the desorption maximum.

The rate constants k_i were modeled in Arrhenius form. For rate constants concerning the recombinative desorption of hydrogen, both a coverage-dependent and coverage-independent approach was used. In our notation k_{des} is reported in s^{-1}, including the condition that one active site is represented by two copper surface atoms [102, 112, 119]. The coverage-dependent form can account for repulsive and attractive interactions of adsorbed molecules, since the assumption of Langmuirian desorption may be not adequate at high or low coverage.

In order to compare different spectra, a dimensionless scaled root mean square error between the experimental value f_1 and the modeling result f_2 is used:

$$\mathrm{SRMSE} = \frac{1}{X_{ref}} \sqrt{\frac{1}{No} \sum_{j=1}^{No} \left(f_1(j) - f_2(j)\right)^2} \tag{5.9}$$

The root mean square error is divided by a reference value X_{ref}. The reference value was chosen in the following way: when comparing two simulations the higher mole fraction of hydrogen at the temperature maximum was used, while the experimental value was chosen when comparing simulation with experiment. For SRMSE values below 0.045 two responses are considered to be equal, within experimental uncertainty [81].

5.4 Results

5.4.1 Mass transfer limitations

Most of the common techniques to determine kinetic parameters are only applicable when transfer limitations such as inner particle mass transfer or re-adsorption as a specific phenomenon occurring in porous systems can be excluded. Wilmer et al. [102] analyzed the dissociative adsorption of hydrogen *via* temperature-programmed adsorption experiments. They found an activation energy of E_{ads} = 48 kJ·mol^{-1} and an Arrhenius factor of A_{ads} = 6·10^2 (Pa·s)$^{-1}$. Comparing modeling results with this set of kinetic parameters with respect to results of a model without re-adsorption leads to a SRMSE value of about 4·10^{-3}. When adsorption is chosen to be less activated re-adsorption becomes evidently significant. Figure 5.1 shows the modeled traces of hydrogen desorption for different values of A_{ads} and E_{ads}. Changing the activation energy of adsorption to a value of 40 kJ·mol^{-1} significantly broadens the signal behind the temperature of the signal maximum (T_{max}). For values below 41 kJ·mol^{-1} re-adsorption becomes relevant (SRMSE $>$ 0.045). Lowering the activation energy to 35 kJ·mol^{-1} makes the signal highly asymmetric. The less activated re-adsorption is, the higher is the shift of T_{max} towards lower temperatures. Changes in A_{ads} have a lower influence on the significance of re-adsorption. A value of A_{ads} = 6·10^3 (Pa·s)$^{-1}$, which is one magnitude higher than the initial value, has still an SRMSE value below 3·10^{-2}. However raising the Arrhenius factor by another magnitude makes re-adsorption significant and the shift of T_{max} is about 4K. Since there is no broadening of the measured TPD signals

observed re-adsorption can be excluded, which is also indicated by the low SRMSE value.

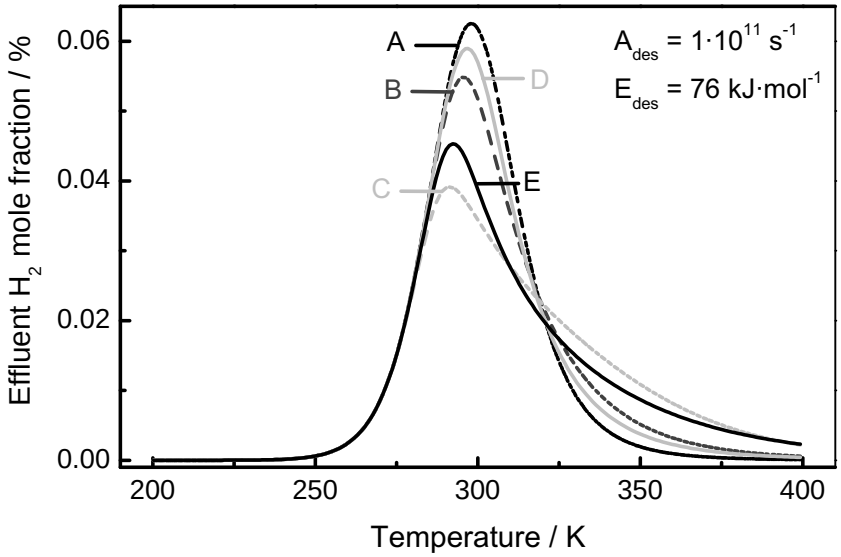

Figure 5.1: Modeled H_2 TPD spectra with different Arrhenius adsorption parameters: (A) A_{ads} = $6{\cdot}10^2$ $(Pa{\cdot}s)^{-1}$, E_{ads} = 48 $kJ{\cdot}mol^{-1}$, (B) A_{ads} = $6{\cdot}10^2$ $(Pa{\cdot}s)^{-1}$, E_{ads} = 40 $kJ{\cdot}mol^{-1}$, (C) A_{ads} = $6{\cdot}10^2$ $(Pa{\cdot}s)^{-1}$, E_{ads} = 35 $kJ{\cdot}mol^{-1}$, (D) A_{ads} = $6{\cdot}10^3$ $(Pa{\cdot}s)^{-1}$, E_{ads} = 48 $kJ{\cdot}mol^{-1}$, (E) A_{ads} = $6{\cdot}10^4$ $(Pa{\cdot}s)^{-1}$, E_{ads} = 48 $kJ{\cdot}mol^{-1}$. Experimental conditions: Q_{He} = 100 $Nml{\cdot}min^{-1}$, β = 6 $K{\cdot}min^{-1}$, ω_{cat} = 0.2 g, θ_H = 1.

Besides re-adsorption, intraparticle diffusion limitations always have to be considered for porous catalysts. However, H_2 TPD experiments are usually performed under conditions where heat and mass transport limitations are negligible [102, 112]. A lot of criteria exist for testing for intraparticle mass transfer limitations, mainly dealing with simplifications [86, 120–122]. Recently, Kanervo et al. [81] established a criterion, which is easily accessible by applying the following formula:

$$\frac{1/\tau}{D_e/r_p^2} = \frac{Qr_p^2\rho_p(1-\epsilon_b)}{D_e\omega_{cat}\epsilon_b} < S_{critical} \tag{5.10}$$

This criterion can be interpreted as the ratio of convective to diffusive flow. High flow rates have to be compensated by a high catalyst mass or by a low particle radius in order to avoid intraparticle mass transfer limitations. Kanervo et al. [81] gave an overview of relevant parameters for TPD flow reactor models. Their criterion was tested against these parameters by relaxing one of the controllable parameters, namely Q, ω_{cat} or r_p, at a time, keeping the rest constant. When $S_{critical}$ is below 0.16 a TPD experiment can safely be described by a plug flow reactor.

However, testing our experimental values against this criterion within the range of Knudsen and effective molecular diffusion led to values that should show significant

intraparticle mass transfer limitations. For our set of parameters, values for $S_{critical}$ were obtained in the range from 0.03 to 0.76. This would imply that one has to account for mass transfer phenomena. Nevertheless, no significant differences between a model with and without intraparticle mass transfer can be observed, when modeling these regimes in case of the hydrogen desorption and using the kinetic values taken from Wilmer et al. [102] (figure 5.2), with E_{ads} = 48 kJ·mol^{-1}, E_{des} = 76 kJ·mol^{-1} and Arrhenius factors of A_{ads} = 6·10^2 (Pa·s)$^{-1}$ and A_{des} = 10^{11} s^{-1}. Comparing a model with and without intraparticle mass transfer, a SRMSE value of 5·10^{-3} is obtained, which means intraparticle mass transfer limitation can be neglected. Furthermore, comparing the two diffusion regimes, Knudsen and effective molecular diffusion, yields an SRMSE value below 3·10^{-4} (not shown in figure 5.2). As being derived for our set of parameters intraparticle mass transfer can be excluded. Consequently, the criterion can be enlarged to $S_{critical} < 40$ when re-adsorption is a significantly activated process. This is achieved by varying the parameters of the criterion equation appropriately until the SRMSE value reaches the critical value of 0.045, when comparing the models.

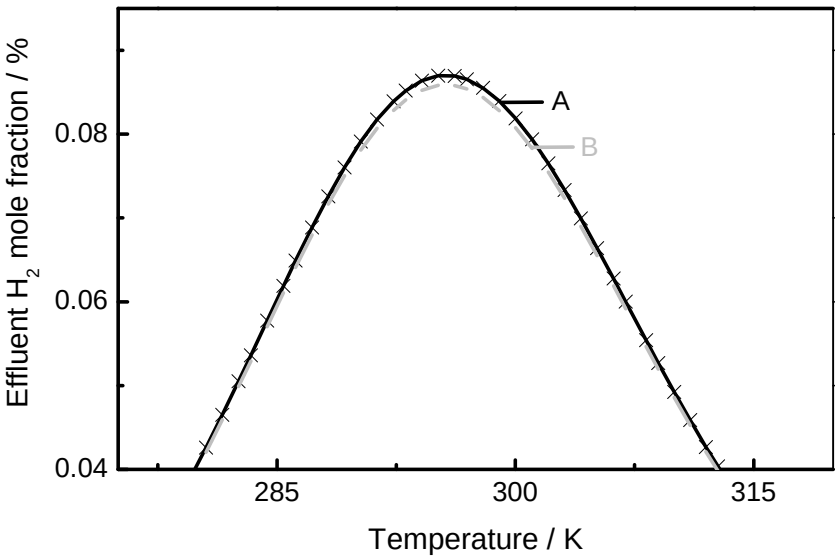

Figure 5.2: Modeled H_2 TPD spectra with different reactor models: (A) Plug flow reactor, (B) Plug flow reactor with intraparticle mass transfer, (x) represents results for a plug flow reactor with axial dispersion, enlarged excerpt around the desorption maxima. Experimental conditions: Q_{He} = 100 Nml·min^{-1}, β = 6 K·min^{-1}, ω_{cat} = 0.2 g, θ_H = 1.

Axial dispersion accounts for back mixing in a fixed-bed reactor. Additionally, figure 5.2 shows the influence of axial dispersion using an axial dispersion coefficient calculated from the given criterion equation with a reasonable value of 2 for the Peclet number [83]. The limiting cases for $Pe \to 0$ and $Pe \to \infty$ are considered by using a CSTR or PFR model, respectively. Comparing a PFR with and without axial dispersion, one obtains completely negligible deviations, as being displayed in figure 5.2 and validated by an SRMSE value below 5·10^{-5}. Furthermore, modeling the TPD using a CSTR reactor

model, the respective signal of hydrogen in the outlet flow is mathematically identical to the models mentioned before, leading to SRMSE $< 5{\cdot}10^{-3}$.

5.4.2 Determination of kinetic parameters

In order to determine the kinetic parameters of the H_2 desorption from Cu surface sites, four mathematical procedures were applied. The results were taken to model the flow temperature-programmed desorption experiments at different initial coverages of hydrogen. These methods comprise of i) heating rate variation, ii) analysis using a fixed pre-exponential factor, iii) lineshape analysis and iv) full model fitting. In general, all methods require different experimental input. The use of the heating rate variation needs data obtained from experimental TPD flow response curves using several heating rates [78, 79, 102, 112]. Typically, the experiments are performed for the initial coverage of a monolayer. Mathematical analysis leads to one pair of corresponding values for A_{des} and E_{des}. According to the method of Redhead [123] the pre-exponential factor A_{des} is kept constant at $10^{13}\,s^{-1}$, yielding an overall value for the activation energy of desorption E_{des} for every spectrum. Each evaluated spectrum can yield a different activation energy of desorption at a single heating rate or initial coverage. Although the Redhead's peak maximum method was derived for evaluation of first order desorption kinetics under UHV conditions, it is straightforward to apply an analogous approach for second order desorption (recombinative desorption) using a model fit with a pre-exponential factor fixed at $1{\cdot}10^{13}\,s^{-1}$. Additionally, a lineshape analysis method was used to fit the TPD spectra [113]. This procedure was also referred as "Arrhenius plots" [78] and can be applied to a single TPD spectrum. It results in pairs of values for A_{des} and E_{des} for every experiment. Finally, a nonlinear least-squares fit to a single TPD response is used to find the desired parameters, including a coverage-dependence. This approach promises to find kinetic parameters valid for the whole spectrum of recorded TPD experiments. In the following all methods are presented in more detail.

In an earlier publication [102], the kinetic parameters of the hydrogen desorption from Cu-based catalysts were determined from the experimental TPD flow experiments applying different heating rates at full coverage. Full coverage (θ_H = 1) is thereby considered as a monolayer of adsorbed hydrogen. The maximum of the desorption signal is shifted to higher temperatures with rising heating rate, while the onset of the signals remains at the same temperature of approximately 240 K. Using Langmuirian second order desorption kinetics with negligible re-adsorption, the signal shift could be analyzed quantitatively. A plot of $\ln\left(T_{max}^2/\beta\right)$ against $1/T_{max}$ yielded the activation energy of the desorption E_{des} of $76 \pm 2\,kJ{\cdot}mol^{-1}$ and a pre-exponential factor A_{des} of $1{\cdot}10^{11} \pm 2{\cdot}10^{11}\,s^{-1}$ [102]. The modeling results for each heating rate, displayed in figure 5.3, showed that the heating rate variation is a reliable tool that fits the experimental data comparatively well, however, with deviations at high coverage. As mentioned before, this is due to the fact that the assumption of a Langmuirian desorption is not adequate for high coverages.

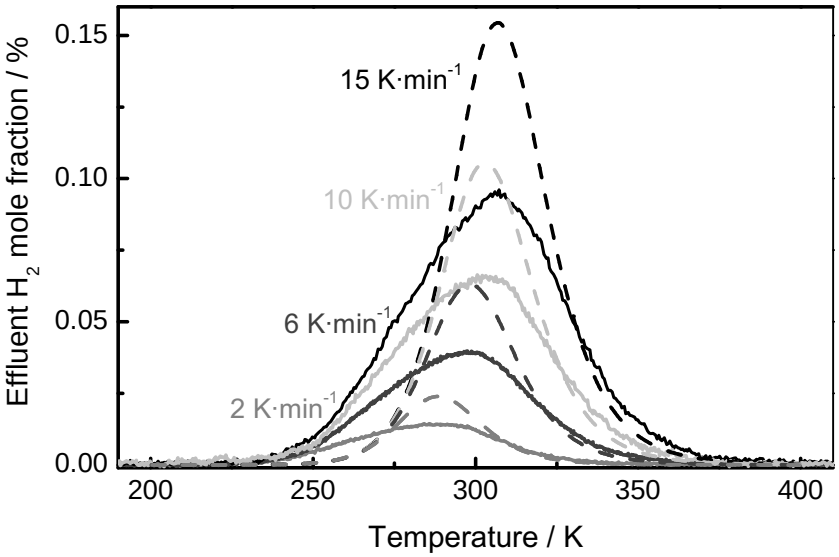

Figure 5.3: Heating rate variation, A_{des} = $1{\cdot}10^{11}\,s^{-1}$, E_{des} = $76\,kJ{\cdot}mol^{-1}$, kinetic values taken from [102]: Experimental H_2 TPD spectra (solid lines) and simulated curves (dashed lines). Experimental conditions: Q_{He} = $100\,Nml{\cdot}min^{-1}$, ω_{cat} = 0.2 g, θ_H = 1.

Figure 5.4 shows the experimental data and simulation results for different hydrogen coverages obtained with a fresh catalyst (not deactivated). Simulated spectra are generated with kinetic parameters extracted from the heating rate variation experiments [102]. For smaller coverages a shift in T_{max} towards higher temperatures can be observed, whereby the descending signal curves approximate. This is due to the fact that adsorbed molecules have fewer neighbors at lower coverages. For the associative desorption a reactive collision has to take place. For lower coverages such a collision is less probable. Furthermore, the onsets of the signals are at different temperatures. Only at full coverage the repulsive interaction of the hydrogen atoms becomes important, which can clearly be seen by the widening of the signal. At full coverage of hydrogen, the simulated signal is too narrow again (see also Figure 5.3), whereas at lower coverages the shapes of the signals can be reproduced sufficiently exact. However the shift in the onset and of maximum temperature is underestimated by the kinetic parameters obtained from the heating rate experiments.

Modeling results based on a model fit with a fixed pre-exponential factor at $1{\cdot}10^{13}\,s^{-1}$ are shown in figure 5.5. Values for E_{des} of 86.5, 88.7, 89.8 and $90.2 \pm 1\,kJ{\cdot}mol^{-1}$ have been extracted for coverages of θ_H = 1, 0.43, 0.16 and 0.08, respectively. By this procedure the activation energy is independent from the Arrhenius factor and no compensation effects between the pre-exponential factor and the energy of desorption are possible. The activation energy depends on the temperature at peak maximum and the initial coverage. That means the activation energy increases with lower coverages, as the signals shift to higher temperatures. Interestingly, an analysis according to Redhead [123], assuming the same pre-exponential factor of $1{\cdot}10^{13}\,s^{-1}$, leads to very similar values for

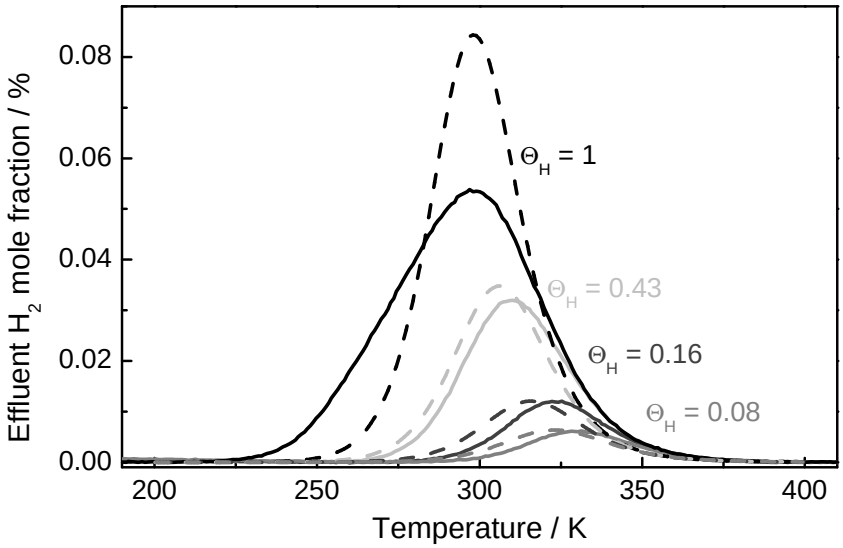

Figure 5.4: Hydrogen coverage variation, A_{des} = $1{\cdot}10^{11}\,s^{-1}$, E_{des} = $76\,kJ{\cdot}mol^{-1}$, kinetic values taken from [102]: Experimental H_2 TPD spectra (solid lines) and simulated curves (dashed lines). Experimental conditions: Q_{He} = $100\,Nml{\cdot}min^{-1}$, ω_{cat} = 0.2 g, β = $6\,K{\cdot}min^{-1}$.

the activation energies ($\pm\,0.5\,kJ{\cdot}mol^{-1}$), even for the second order desorption considered here. When comparing the modeled signals, the results are comparable to the ones of the heating rate variation with less deviation at lower coverages (figure 5.5) according to the SRMSE values. The T_{max} values are reproduced better though.

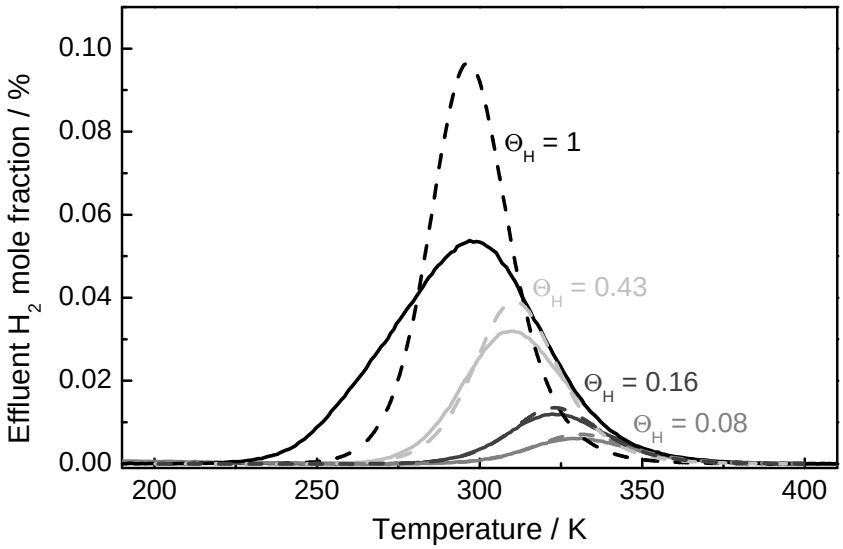

Figure 5.5: Hydrogen coverage variation, modeling according to fixed pre-exponential factor analysis, A_{des} = $1{\cdot}10^{13}\,s^{-1}$, E_{des} = 86 - $90\,kJ{\cdot}mol^{-1}$: Experimental H_2 TPD spectra (solid lines) and simulated curves (dashed lines). Experimental conditions: Q_{He} = $100\,Nml{\cdot}min^{-1}$, ω_{cat} = 0.2 g, β = $6\,K{\cdot}min^{-1}$.

Furthermore, a particularly good fit of the respective experimental spectra (figure 5.6) is achieved by the lineshape analysis method [78, 113], resulting in pairs of A_{des} and

E_{des} for each spectrum (table 5.1). Plots of $\ln(r_{des}/\theta_H^2)$ against $1/T$ for different initial coverages leads to a straight line. The rate of desorption is proportional to the height of the peak at that temperature, whereas the area behind that peak is equivalent to the coverage of hydrogen at that rate. Intercept and slope yield the desired parameters, A_{des} and E_{des}, respectively. However, this method results in unreasonable physical values, i.e. A_{des} ranging from $1.8{\cdot}10^7 \pm 2{\cdot}10^7\,\mathrm{s^{-1}}$ to $6{\cdot}10^{13} \pm 6{\cdot}10^{13}\,\mathrm{s^{-1}}$ and E_{des} ranging from 54 to $95 \pm 3\,\mathrm{kJ{\cdot}mol^{-1}}$.

Table 5.1: Parameters derived from different methods, *Results for the heating rate variation are taken from Wilmer et al. [102].

Figure	Method	θ_H	β	A_{des}	E_{des}	SRMSE
		-	$\mathrm{K{\cdot}min^{-1}}$	$\mathrm{s^{-1}}$	$\mathrm{kJ{\cdot}mol^{-1}}$	-
5.3	Heating rate variation*	1	2	$1.00{\cdot}10^{11}$	76.00	0.228
5.3	Heating rate variation*	1	6	$1.00{\cdot}10^{11}$	76.00	0.214
5.3	Heating rate variation*	1	10	$1.00{\cdot}10^{11}$	76.00	0.219
5.3	Heating rate variation*	1	15	$1.00{\cdot}10^{11}$	76.00	0.210
5.4	Heating rate variation*	1	6	$1.00{\cdot}10^{11}$	76.00	0.200
5.4	Heating rate variation*	0.43	6	$1.00{\cdot}10^{11}$	76.00	0.082
5.4	Heating rate variation*	0.16	6	$1.00{\cdot}10^{11}$	76.00	0.128
5.4	Heating rate variation*	0.08	6	$1.00{\cdot}10^{11}$	76.00	0.127
5.5	Fixed prefactor	1	6	$1.00{\cdot}10^{13}$	86.54	0.255
5.5	Fixed prefactor	0.43	6	$1.00{\cdot}10^{13}$	88.72	0.067
5.5	Fixed prefactor	0.16	6	$1.00{\cdot}10^{13}$	89.75	0.040
5.5	Fixed prefactor	0.08	6	$1.00{\cdot}10^{13}$	90.16	0.061
5.6	Lineshape analysis	1	6	$1.80{\cdot}10^{7}$	53.60	0.139
5.6	Lineshape analysis	0.43	6	$3.00{\cdot}10^{11}$	80.30	0.044
5.6	Lineshape analysis	0.16	6	$2.20{\cdot}10^{12}$	86.30	0.036
5.6	Lineshape analysis	0.08	6	$6.00{\cdot}10^{13}$	95.40	0.084
5.7	Full analysis	1	6	$3.75{\cdot}10^{10}$	$74.95 - 5.51 \cdot \theta^{2.59}$	0.024
5.7	Full analysis	1	6	$3.75{\cdot}10^{10}$	$74.95 - 5.51 \cdot \theta^{2.59}$	0.031
5.7	Full analysis	0.43	6	$3.75{\cdot}10^{10}$	$74.95 - 5.51 \cdot \theta^{2.59}$	0.013
5.7	Full analysis	0.16	6	$3.75{\cdot}10^{10}$	$74.95 - 5.51 \cdot \theta^{2.59}$	0.035
5.7	Full analysis	0.08	6	$3.75{\cdot}10^{10}$	$74.95 - 5.51 \cdot \theta^{2.59}$	0.042

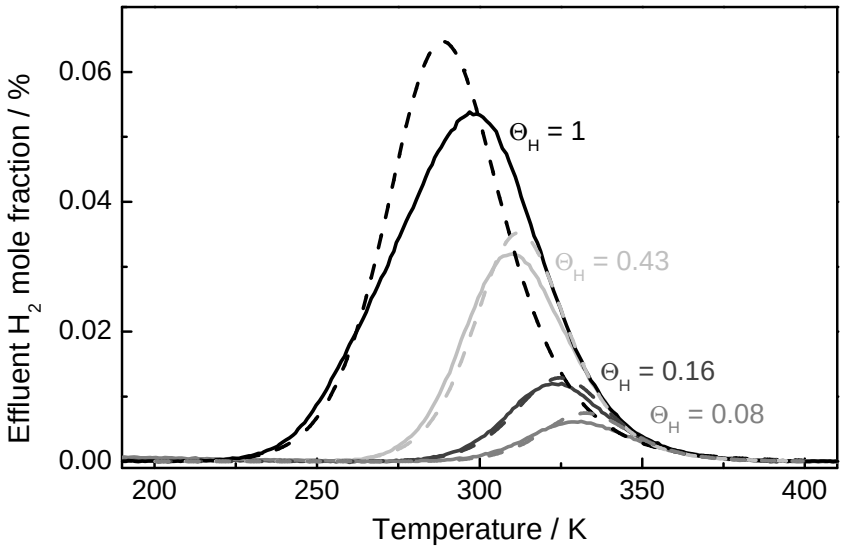

Figure 5.6: Lineshape analysis A_{des} = $1.8{\cdot}10^{7}$-$6{\cdot}10^{13}\,s^{-1}$, E_{des} = 54 - $95\,kJ{\cdot}mol^{-1}$: Experimental H_2 TPD spectra (solid lines) and simulated curves (dashed lines). Experimental conditions: Q_{He} = $100\,Nml{\cdot}min^{-1}$, ω_{cat} = 0.2 g, β = $6\,K{\cdot}min^{-1}$.

Since transport limitations could be excluded and all simulated signals at high coverage are narrower than the corresponding experimental ones, a fourth approach was introduced in order to reproduce the experimental data more adequately. The Langmuirian assumption seems to be not adequately enough, the coverage-dependence was introduced into the energy of desorption as follows:

$$E_{des}\,(\theta_H) = E_{des}\,(\theta_H = 0) - K \cdot \theta_H^n \tag{5.11}$$

The models are fitted to the experimental results using a nonlinear least-squares fit, which requires an initial guess. As a starting point, the physically meaningful results of the heating rate variation were chosen, which can be interpreted as mean values. One experimental response was chosen (θ_H = 1, β = $6\,K{\cdot}min^{-1}$, fresh catalyst), all other spectra were simulated using the derived kinetic parameters. First, a fixed linear coverage-dependence was considered (n = 1), yielding K = $5.5\,kJ{\cdot}mol^{-1}$. The model description of the experiments improves significantly, however, the onset and the ending of the signal were not reproduced sufficiently, yielding a SRMSE value around 0.13. Nevertheless, a second order dependence further improves the description of the experiment. When the order of coverage-dependence n is finally relaxed, parameters are obtained which reproduce the experiments very accurately. The results of the kinetic parameters are well in the range of reference values [102, 111–113, 119], i.e. the best fit for a heating rate of $6\,K{\cdot}min^{-1}$ is obtained for A_{des} = $3.75{\cdot}10^{10} \pm 4{\cdot}10^{10}\,s^{-1}$ and E_{des} = $75 \pm 3\,kJ{\cdot}mol^{-1}$ - $5.5 \pm 1.5\,kJ{\cdot}mol^{-1} \cdot \theta_H^{2.6 \pm 0.4}$. Again, it has to be pointed out that the fitting was performed with the data taken from one specific TPD experiment, where both ways of data reduction yielded essentially the same results. The validity of the

model parameters is indicated by the means that only one experimental spectrum is sufficient to extract the desired parameters. This approach allows to easily implement a coverage-dependent activation energy for desorption. Figure 5.7 shows the results for the fit when considering coverage-dependence (fresh catalyst at full coverage). The corresponding simulations at different hydrogen coverages as well as for a deactivated catalyst at full coverage (θ_H = 1, smaller peak height) are included here. It can clearly be seen that the coverage-dependence improves the mathematical model. It fits the data from other experiments in an excellent way with respect to the shape of the signal and to the position of T_{max}. Regarding all evaluation methods, the coverage-dependence becomes less important at lower coverages. For clarity, the spectra for the other heating rates (2, 10 and 15 K·min^{-1}) are not shown in figure 5.7. The agreement between experimental and modeled spectra is also very good, leading to SRMSE values below 0.034.

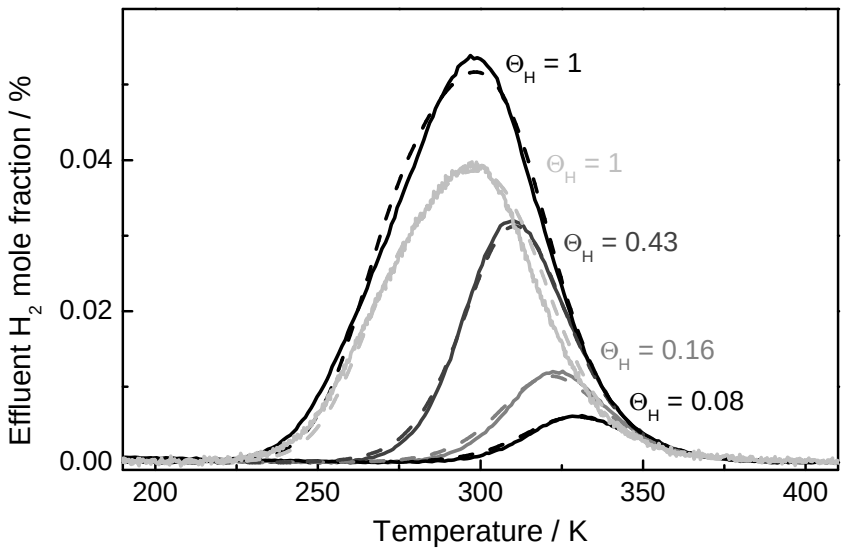

Figure 5.7: Results for A_{des} = 3.75·10^{10} s^{-1} and E_{des} = 75 kJ·mol^{-1} - 5.5 kJ·mol^{-1} $\cdot \theta_H^{2.6}$: Experimental H_2 TPD spectra (solid lines) and simulated curves (dashed lines). Experimental conditions: Q_{He} = 100 Nml·min^{-1}, ω_{cat} = 0.2 g, β = 6 K·min^{-1}.

5.5 Discussion

When interpreting temperature-programmed desorption flow experiments under ambient pressure care should be taken. Common techniques for UHV conditions are only valid when re-adsorption processes and transport limitations during the TPD flow experiments can be excluded. During those experiments, the concentration of the desorbing molecules is reduced by the dilution of the carrier gas. Thereby the re-adsorption probability is decreased. In our case, the absence of re-adsorption processes is confirmed by comparative simulations. However, it is clearly demonstrated that

re-adsorption processes are highly sensitive on the desorption signal. Compared to the findings of Kanervo et al. [81], the absence of re-adsorption also enhances the mass transfer inside the particle and therefore minimizes the effect of intraparticle mass transfer, since re-adsorption becomes less when activated. For the criterion of Kanervo et al. [81], only extremely low activated re-adsorption (up to $E_{ads} = 10\,\mathrm{kJ \cdot mol^{-1}}$) was taken into account, resulting in a more rigorous value. When adsorption is a highly activated process only slight differences in the reactor models are observable (see also figure 5.2).

Since no transfer limitations are observable in our experiments, the determination of the desorption kinetics is straightforward. Table 5.1 summarizes all kinetic parameters determined by the different procedures, together with the calculated SRMSE values. The highest SRMSE values are obtained when modeling traces at full coverage. This is attributed to significant broadening of the experimental H_2 TPD spectra due to non-Langmuirian behavior for θ_H towards 1. The results obtained by an analysis with a fixed pre-exponential factor demonstrate that the activation energy increases with lower coverage and desorption becomes more activated. The energy of desorption increases about $4\,\mathrm{kJ{\cdot}mol^{-1}}$ for a coverage from 1 to 0.08. Care should be taken when the data are discussed with a physical background and the pre-exponential factor is unknown and therefore chosen to be $1{\cdot}10^{13}\,\mathrm{s^{-1}}$. While Roberts and Griffin [124] found a comparable energy of desorption of about $86\,\mathrm{kJ{\cdot}mol^{-1}}$ utilizing the Redhead's peak maximum method, different methods, which also yield a pre-exponential factor, led to activation energies around $70\,\mathrm{kJ{\cdot}mol^{-1}}$ [102, 112, 113]. An appropriate choice of the pre-exponential factor is essential for the extraction of a physically meaningful value for E_{des}, i.e. choosing a pre-exponential factor of $1{\cdot}10^{11}\,\mathrm{s^{-1}}$ leads to an E_{des} around $75\,\mathrm{kJ{\cdot}mol^{-1}}$ for $\theta_H = 1$. While heating rate variation yields mean values, this method covers the full range of coverage, assuring physically meaningful parameters for A_{des} and E_{des}. This can also be seen when comparing the results to those obtained by the lineshape analysis method, which are comparable at an intermediate coverage of $\theta_H = 0.43$. However, the lineshape analysis method failed at full coverage, resulting in kinetic parameters which are not physically meaningful and in a position of T_{max} being completely wrong. For lower coverages, the compensation effect of A_{des} and E_{des} led to higher values for the respective parameter. Though, the agreement between experiment and simulation is high. For all methods the error becomes less when the coverage is lowered, except for the model fitting where all values are below 0.045. Accounting for the repulsive interaction of the hydrogen atoms by a factor of $5.5 \cdot \theta_H^{2.6}\,\mathrm{kJ{\cdot}mol^{-1}}$ fits the experiments best. A full analysis yields $k_{des} = 3.75{\cdot}10^{10}\,\mathrm{s^{-1}}{\cdot}\exp(-(75\,\mathrm{kJ{\cdot}mol^{-1}} - 5.5\,\mathrm{kJ{\cdot}mol^{-1}} \cdot \theta_H^{2.6})/RT)$, which is comparable for the results by Anger et al. [111] for Cu(111), suggesting that the catalysts predominantly exposes Cu(111) facets. This is in perfect agreement with results published in previous studies [102, 112, 113]. A coverage-dependent Arrhenius factor of $3.4{\cdot}10^{10}\,\mathrm{s^{-1}}$ to $1.5{\cdot}10^{11}\,\mathrm{s^{-1}}$ and an activation energy of $63\,\mathrm{kJ{\cdot}mol^{-1}}$ to $77\,\mathrm{kJ{\cdot}mol^{-1}}$ was found based on the assumption that one active site consists of two copper surface atoms ($\theta_{H,max} = 1$) [119]. On Cu(111), Anger et al. [7] extracted a coverage-dependent factor of the activation energy of $K = 14.6\,\mathrm{kJ{\cdot}mol^{-1}}$. However, in a previous work [119] it

was already shown that this value was too high, overestimating the coverage-dependence. An analysis using a fixed pre-exponential factor led to an increase of about $4\,\mathrm{kJ{\cdot}mol^{-1}}$, indicating that a value of $K = 5.5\,\mathrm{kJ{\cdot}mol^{-1}}$ is in an absolutely reasonable magnitude. The factor of 2.6 is contributed to the shape of the signal and can therefore be interpreted as the magnitude of repulsive interactions of the adsorbed species. It should be pointed out that care should be taken when evaluating TPD data with model fits. An approach with a more rigorous and straightforward procedure comprises the following steps: simultaneously fitting of all parameters, searching for a global minimum and therefore the best mathematical description of the experiments. This procedure yields even a better fit (SRMSE of about 0.01). However, quite physically unlikely values of $A_{des} = 7 \cdot 10^8\,\mathrm{s^{-1}}$ and E_{des} ranging from 57 to $62\,\mathrm{kJ{\cdot}mol^{-1}}$ were obtained. It is highly recommended to evaluate TPD experiments with common techniques, i.e. heating rate variation, before the model fitting.

An accurate explanation of hydrogen desorption is very relevant for microkinetic modeling in industrial processes, in particular, for the water-gas shift and methanol synthesis reaction. Both reactions comprise of several hydrogenation steps over Cu-based catalysts. Microkinetic models have been introduced based on the *surface-science approach* [10, 12–17]. In particular, the change in morphology has been included using Wulff's construction, leading to a description of the rate of methanol formation in terms of the contributions of different Cu facets as a function of the atmosphere applied. With respect to our results for the deactivated and non-deactivated state of the catalyst, a comparison indicates that the morphology reversibly changes, since the obtained kinetic data are equal for both catalysts. For the results taken from Wilmer et al. [102] the ternary catalyst was deactivated by performing methanol synthesis at very mild conditions. Then, the catalyst was reduced and flushed with helium to achieve an adsorbate-free copper surface before the TPD experiment. It is remarkable that the experimental TPD traces of the deactivated and not deactivated catalyst (i.e. figure 5.7, $\theta_H = 1$) do not show any differences in the onset or peak maximum temperature. This clearly means that deactivation of the catalyst only decrease the number of active sites, i.e. in our experiment by about 25%. Obviously, the parameters can be determined using a fresh or deactivated catalyst in the same way.

5.6 Conclusions

A criterion by Kanervo et al. [81] was revised and enlarged in order to be applicable for highly activated adsorption processes during second order desorption experiments. When re-adsorption and transport limitations can be neglected within the experimental range, different analysis methods can be applied in order to extract kinetic parameters from TPD flow experiments.

In the case of hydrogen desorption from a ternary Cu-based catalyst, parameters obtained by the heating rate variation and the lineshape analysis at an intermediate coverage of θ_H are in a physically meaningful range. Care should be particularly taken

for the lineshape analysis at full coverage, which could not even reproduce the position of T_{max}. An analysis with a fixed pre-exponential factor results in comparable values when the pre-exponential factor A_{des} is known. All methods are generally applicable to extract kinetic parameters from temperature-programmed flow desorption experiments, but care should be taken when repulsive interactions are not negligible. Nonetheless, sufficient experimental data should be used. Parameters from a single experiment, i.e. extracted by an analysis method using a fixed pre-exponential factor or the lineshape analysis, might not be significant or even physically unreasonable. A full analysis showed that the best results are obtained when the activation energy varies with coverage. The analysis led to $k_{des} = 3.75{\cdot}10^{10}\,\mathrm{s^{-1}}{\cdot}\exp(-(75\,\mathrm{kJ{\cdot}mol^{-1}} - 5.5\,\mathrm{kJ{\cdot}mol^{-1}} \cdot \theta_H^{2.6})/RT)$. It is in a range, which is comparable to the values found before [102, 111–113], but describes all experiments more precisely.

For the simulations, the desorption spectra for the methods based on Langmuirian assumptions are essentially the same, however when this assumption is relaxed, a better agreement between experiment and simulation can be achieved. Hence, an exact description of the coverage-dependence on ternary catalysts enhances the detailed understanding of those reaction mechanisms at industrially more relevant conditions.

6 On the interaction of carbon monoxide with ternary $Cu/ZnO/Al_2O_3$ catalysts: Modeling of dynamic morphology changes and the influence on elementary step kinetics

6.1 Abstract

This paper focuses on gas-phase induced dynamical catalyst morphology changes, in particular by carbon monoxide. Those structural changes are studied in terms of hydrogen temperature-programmed desorption (TPD) from carbon monoxide pre-treated surfaces. Modeling the hydrogen TPD from the pre-treated catalyst shows an activation of Cu(110) and Cu(100) planes. This is in good agreement with previously shown morphology changes in different gas atmospheres observed from *in-situ* EXAFS and TEM measurements and observed transient maxima of methanol synthesis upon CO pre-treatment which has been reported in literature. The obtained hydrogen desorption energies for the respective copper surfaces are physically reasonable. This surface heterogeneity is further implemented in a microkinetic model to describe the temperature-programmed surface reaction (TPSR) between carbon monoxide and adsorbed oxygen. It is found that a logarithmic coverage-dependence for adsorbed oxygen is essential for obtaining good agreement between simulation and experiment. For high oxygen loadings the apparent activation energy is essentially constant, which is in good agreement with literature results.

6.2 Introduction

Nowadays, methanol counts among the top ten basic chemical and becomes even more important as a chemical energy carrier [18, 125]. With receding coal and gas reserves methanol can act as an alternative way for energy storage and directly as a fuel [125]. Methanol is commercially produced *via* synthesis gas (CO_2, CO and hydrogen) over $Cu/ZnO/Al_2O_3$ catalysts. Hereby, methanol is mainly produced by the hydrogenation of carbon dioxide [32–34]. However, typically carbon monoxide is not separated from carbon dioxide, but can be converted to carbon dioxide by the

water-gas shift reaction. This suppresses the formation of water, which is known to inhibit the methanol production and to enhance deactivation of the catalyst [35, 36]. Copper particles have been identified as active sites [39, 40] and are known to underlay dynamical morphology changes, depending on the gas atmosphere [24, 25, 28, 29, 41]. Wilmer and Hinrichsen [41] and later Vesborg et al. [29] found, that the methanol production rate strongly depends on the pre-treatment conditions. A treatment with carbon monoxide before methanol synthesis leads to a transient maximum in methanol production. This dynamic effect was also observed by the development of highly sensitive *in-situ* methods, such as Extended X-ray Absorption Fine Structure (EXAFS) and Transmission Electron Microscopy (TEM) measurements [24, 25, 28, 29]. From these experiments it was proposed that the metallic copper morphology changes are mainly attributed to the Cu/ZnO interface energy. Clausen et al. [25] used the Wulff construction to relate the equilibrium shape of the *fcc* particles to the contact surface free energy. This concept was later incorporated into a microkinetic model for the methanol synthesis [10, 13]. Subsequently, Hansen et al. [28] and Vesborg et al. [29] quantified these effects by calculating the energy changes with data extracted from *in-situ* TEM measurements. The gas environment is not only responsible for changes in surface area but also for changes in the ratio of different surface facets. The microkinetic model by Ovesen et al. [13] has incorporated different rates for methanol synthesis over the three low-index planes Cu(111), Cu(110) and Cu(100). It is assumed that a change in the ratio of those planes may also enhance the methanol productivity.

Besides EXAFS and TEM measurements temperature-programmed (TP) experiments, i.e. TP adsorption and TP desorption, have always been a subject of great interest for catalyst characterization and also for extraction of parameters for elementary step kinetics [2, 78–80, 109, 110]. A profound survey can be found in case of copper catalysts in the literature [77, 102, 103, 111–113]. First, UHV methods were applied to extract the kinetics of the sorption processes, later flow set-ups under ambient pressure were used to quantify the energies of ad- and desorption. However, this was not the only subject of interest, as Muhler et al. [77, 97] established the hydrogen temperature-programmed desorption as a tool to quantify the active copper surface area. This method was attributed to be more mild and less destructive, compared to the widely used N_2O frontal chromatography [96, 98]. Wilmer and Hinrichsen [41] used the hydrogen desorption from the copper catalyst to study dynamical changes in the catalyst. The catalyst was pre-treated by flushing it with either synthesis gas or carbon monoxide before dosing the hydrogen. With synthesis gas a symmetrical TPD signal was observed, whereas for different CO/He pre-treatment the signal became asymmetrical in shape, being more significant for longer pre-treatment times. A second shoulder was assigned to a different surface site evolving with a severe reducing pre-treatment [41].

This paper studies the interaction of carbon monoxide with the ternary copper catalyst. Numerical procedures are used to quantitatively evaluate the effect of a catalyst pre-treatment with carbon monoxide. Simple kinetics and the ratio of exposed copper facets are extracted from those experiments, which supplies interesting information in addition to the *in-situ* measurements by Hansen et al. [28] and Vesborg et al. [29].

In a second part, the kinetics of carbon monoxide oxidation to carbon dioxide, an important elementary step for the methanol synthesis or water-gas shift reaction [10–14], is studied in great detail, giving a relation for the coverage-dependence of carbon monoxide oxidation.

6.3 Experimental and computational details

The fixed-bed reactor can either be modeled as a continuously stirred-tank reactor (CSTR) or as a plug flow reactor (PFR), within the limits of total and negligible back-mixing in the catalytic bed. The corresponding equations for the CSTR and PFR are given as [81, 103]:

$$\frac{\partial c_i}{\partial t} = -\frac{1}{\tau(t)}\left(c_i - c_{i,inlet}\right) + \frac{\left(1-\epsilon_b\right)\rho_p N}{\epsilon_b} r_{total,i} \tag{6.1}$$

$$\frac{\partial c_i}{\partial t} = -\frac{u(t)}{L\epsilon_b}\frac{\partial c_i}{\partial x} + \frac{\left(1-\epsilon_b\right)\rho_p N}{\epsilon_b} r_{total,i} \tag{6.2}$$

The overall rate $r_{total,i}$ for a specific compound describes the averaged rate over different catalytic active surface planes.

In a previous study we already showed that the hydrogen TPD experiments from the copper catalyst under the evaluated conditions can safely be treated using a CSTR reactor model [103]. The calculations concerning the TPSR of carbon monoxide and adsorbed oxygen to yield carbon dioxide were performed with both reactor models, to rule out a reactor model limitation.

Surface species are further calculated by an ordinary differential equation:

$$\frac{\partial \theta_{i,hkl}}{\partial t} = \sum \nu_{i,j} r_{j,hkl} \tag{6.3}$$

MATLAB® R2010b was used to solve the governing equations. MATLAB® comprises a built-in sparse system ODE solver (ode15s). The absolute tolerances were set to a value of 10^{-10}. For the PFR reactor model partial differential equations were discretized by the methods of lines [74], using a backward differences scheme. Numerical convergence and mass conservation was tested for all models. For fittings, either the MATLAB® nonlinear least-squares fitting “lsqnonlin” or the constrained nonlinear optimization “fmincon” was implemented. The “fmincon” routine can solve optimization problems including both linear and nonlinear bound constraints. The termination tolerance on the function value was chosen to be 10^{-15}. For each experiment a well defined temperature interval was chosen. For the hydrogen desorption experiments, experimental data from the onset to the ending of the signal was included into the objective function, as the signals became highly unsymmetrical upon a treatment in CO/He [41]. However, for the TPSR experiments a fit around the maximum of the mole fraction of CO_2 in the

outlet flow was used in order to avoid limitations by the tailing of the experimental signal [103, 126].

The quality of a respective model fit was evaluated by introducing a dimensionless scaled root mean square error between the experimental value f_1 and the modeling result f_2:

$$\text{SRMSE} = \frac{1}{X_{ref}} \sqrt{\frac{1}{No} \sum_{j=1}^{No} (f_1(j) - f_2(j))^2} \tag{6.4}$$

Here, the root mean square error is divided by the maximum experimental concentration in the outlet flow of the respective experiment, X_{ref}. For SRMSE values below 0.045 two responses are considered to be equal, corresponding to a deviation below experimental certainty [81].

The results for the pre-treated hydrogen temperature-programmed desorption experiments were taken from Wilmer and Hinrichsen [41]. Before dosing the hydrogen, the catalyst was either pre-treated with methanol synthesis gas or CO/He at 493 K. An adsorbate-free surface was achieved by flushing the catalyst with He at 493 K. Subsequently, saturation coverage of hydrogen was achieved by dosing the hydrogen at 240 K and 15 bar for half an hour [112]. The pressure was reduced to atmospheric pressure and the reactor was cooled to 78 K. Subsequent to an additional He treatment for 30 minutes, desorption flow experiments were initialized by changing the temperature linearly up to 493 K in the He flow [41].

For the CO temperature-programmed surface reaction, experimental results were taken from Hinrichsen et al. [126]. Before each experimental run methanol synthesis was carried out over night. Subsequently, the catalyst was flushed with He at 493 K to achieve an adsorbate-free surface. Saturation coverage of adsorbed oxygen ($\theta_O = 0.5$) was then achieved by switching to N_2O/He. Consequently, the temperature was lowered to 78 K and the gas flow was changed to CO/He, followed by starting a linear temperature ramp to 300 K [126].

6.4 Results

6.4.1 Dynamic behavior of the $Cu/ZnO/Al_2O_3$ catalyst

Figure 6.1 shows the results for a hydrogen TPD obtained by Wilmer and Hinrichsen [41] (solid lines) subsequent to pre-treating the copper catalyst either with methanol synthesis gas or carbon monoxide in helium. Trace A shows the results for the catalyst pre-treated in methanol synthesis gas. This signal is very symmetrical and is equal in shape and T_{max} position compared to experiments at full coverage, already presented elsewhere [103]. Traces B, C and D were recorded after different times of CO/He pre-treatment. After one hour the amount of adsorbed hydrogen drops by about 13% and the shape becomes slightly asymmetrical (trace B). After 18 hours the amount further decreases

and a second shoulder evolves (trace C). Finally after a severe treatment of 64 hours in CO/He, a second maximum can clearly be observed. These changes in symmetry were proven to be reversible [41]. Hence, no irreversible surface reconstruction was observed. The unsymmetrical peaks suggest that desorption takes place from different active sites, comprising different desorption parameters. While the symmetric peak in trace A was often referred to desorption from mainly Cu(111) [103, 112, 113], the low temperature shoulder (traces B-D) can be explained by a second crystal facet. Furthermore the second maximum is shifted to higher temperatures at saturation coverage, which suggests that a third kind of active site is activated during such a pre-treatment.

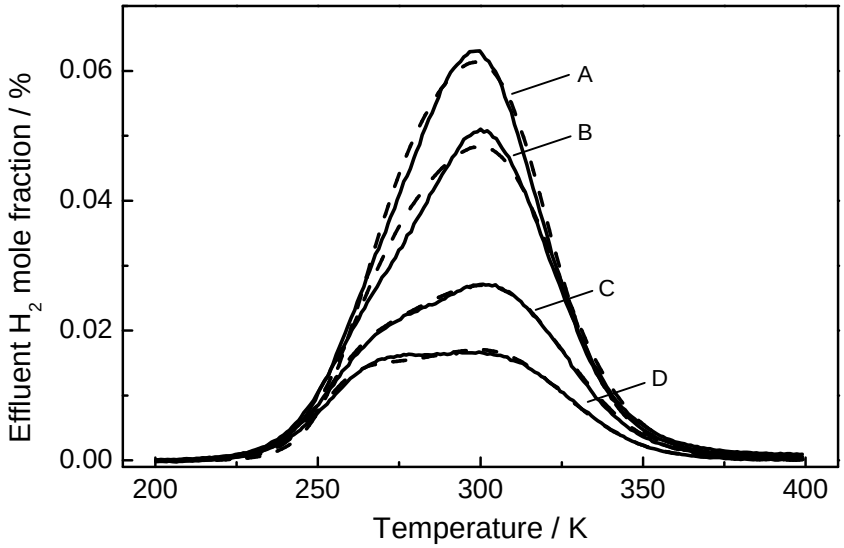

Figure 6.1: Experimental H_2 TPD spectra (solid lines) and simulated curves (dashed lines), after pre-treatment of the catalyst with CO/He for: (A) 0 h (SRMSE = 0.022), (B) 1 h (SRMSE = 0.027), (C) 18 h (SRMSE = 0.014), (D) 64 h (SRMSE = 0.019). Experimental conditions: Q_{He} = 100 Nml·min^{-1}, β = 6 K·min^{-1}, ω_{cat} = 0.2 g, θ_H = 1.

Three different active sites were considered, for the Cu(111) facets kinetic values were taken from reference [103] (see also table 6.1). Hereby $N \cdot r_{total}$ is given by:

$$\begin{aligned} N \cdot r_{total} = N_{H_2,sat,111} \cdot \left(-\frac{\partial \theta_{H,111}}{\partial t}\right) + N_{H_2,sat,110} \cdot \left(-\frac{\partial \theta_{H,110}}{\partial t}\right) \\ + N_{H_2,sat,100} \cdot \left(-\frac{\partial \theta_{H,100}}{\partial t}\right) \end{aligned} \tag{6.5}$$

and

$$N_{H_2,sat} = \frac{\sum n_{H_2,des,hkl}}{\theta_{H,ini}\omega_{cat}} \tag{6.6}$$

Since it was already shown that re-adsorption is negligible under the evaluated experimental conditions [103], only desorption of hydrogen has to be considered, thus the rate for surface hydrogen reads in the case of recombinative desorption:

$$\frac{\partial \theta_{H,hkl}}{\partial t} = -r_{H,hkl} = -2 \cdot k_{des,hkl} \theta_{H,hkl}^2 \tag{6.7}$$

The mass conservation is given by:

$$\sum n_{H_2,des,hkl} = n_{H_2,des,experimental} \tag{6.8}$$

Hence, the specific moles $n_{H_2,des,hkl}$ desorbed from one surface plane can be calculated by the conservation law. To avoid unreasonable values the following constraint was implemented, using the "fmincon" fitting routine:

$$n_{H_2,des,hkl} \geq 0 \tag{6.9}$$

A more rigorous approach, using the "lsqnonlin" fitting routine without this constraint leads to imaginary values during the first iterations but results in the same parameters at the end of the model fitting. Figure 6.1 compares the experimental and modeled traces of the hydrogen desorption for different pre-treatments. Kinetic parameters for the unknown surfaces, which we assign to Cu(110) and Cu(100), and the specific mol number of desorbing hydrogen were subject of the model fit, yielding the kinetic parameters of $E_{des,100}$ = 63.7 kJ·mol^{-1} and $E_{des,110}$ = 81.2 kJ·mol^{-1}, respectively. All results are displayed in table 6.1.

Table 6.1: Parameters derived from hydrogen TPD with different CO/He pre-treatment times, *Value taken from reference [103].

Parameter	Value	95% confidence interval	Fraction
$E_{a,111}$ / (kJ·mol^{-1})*	75 - 5.5·$\theta_H^{2.6}$	-	-
$E_{a,110}$ / (kJ·mol^{-1})	81.2	± 0.2	-
$E_{a,100}$ / (kJ·mol^{-1})	63.7	± 0.1	-
$n_{H_2,des,111,1h}$ / μmol	20.7	± 0.2	0.88
$n_{H_2,des,100,1h}$ / μmol	1.0	± 0.1	0.04
$n_{H_2,des,111,18h}$ / μmol	11.3	± 0.1	0.77
$n_{H_2,des,100,18h}$ / μmol	1.8	± 0.1	0.12
$n_{H_2,des,111,64h}$ / μmol	7.1	± 0.1	0.72
$n_{H_2,des,100,64h}$ / μmol	1.9	± 0.04	0.19

Hereby, we kept the Arrhenius factor of desorption constant at 3.75·10^{10} s^{-1} (= $A_{des,111}$), to avoid physical unreasonable values. In a recent paper we could already show that a proper choice of A_{des}, while fitting E_{des}, might lead to reasonable values for the desorption energy [103]. In order to determine which sites are evolving, hydrogen desorption experiments under UHV from different low-index planes by Anger et al. [111]

are analyzed, in particular the T_{max} position of the desorption maxima. In their study the T_{max} positions at full coverage follow the order Cu(100) < Cu(111) < Cu(110). Since the signal for a fresh or syngas treated polycrystalline copper catalyst was previously attributed to show Cu(111) desorption kinetics [103, 112, 113], it can be concluded that the high temperature hydrogen signal is caused by hydrogen desorbing from Cu(110) surface sites. In the study of Anger et al. [111] the evaluation of Cu(100), on the other hand, was not possible due to complex surface reconstruction processes. However, the position of T_{max} at full coverage indicates that Cu(100) planes are most likely responsible for the low temperature maximum in our study. Limitations by surface reconstruction were not observed for the evaluation method presented in this study, since all experiments were reversible and even the spectra under most reducing conditions could be reproduced in good agreement [41]. Therefore, it is straightforward to conclude that the extracted parameters with the higher activation energy should be attributed to Cu(110) surface planes, whereas the low energy maximum is caused by exposed Cu(100) planes. As can be seen modeled and measured spectra are in great agreement. This is also indicated by SRMSE values below 0.03. It should be mentioned, that it was not possible to properly describe all signals with only one new type of crystal planes. Besides Cu(111), two more crystal facets are needed to describe the desorption.

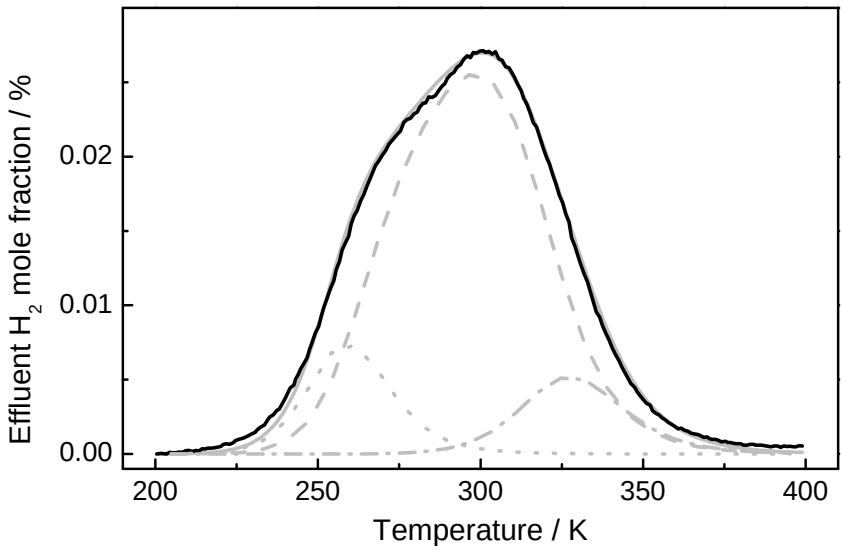

Figure 6.2: Experimental H_2 TPD spectrum (black) and simulated curves (grey), after pre-treatment of the catalyst with CO/He for 18 h, contributions from different copper facets: Cu(111) dashed, Cu(100) dotted and Cu(110) dashed dotted. Experimental conditions: Q_{He} = 100 Nml·min^{-1}, β = 6 K·min^{-1}, ω_{cat} = 0.2 g, θ_H = 1.

As an example, figure 6.2 summarizes the contribution of each surface plane to the overall signal. In here, Cu(110) has the lowest fraction, followed by Cu(100). For all pre-treatments, Cu(111) has the highest fraction. Figure 6.3 shows the trend for the distribution of active sites for the different surface planes, calculated from the amount

of desorbed hydrogen (see also table 6.1). The amount of Cu(111) drops with longer exposure to CO/He, while the amount of Cu(110) first rises and slightly drops after 18 hours. The amount of Cu(100) however, rises steadily for all experiments, with a higher slope at a lower pre-treatment time.

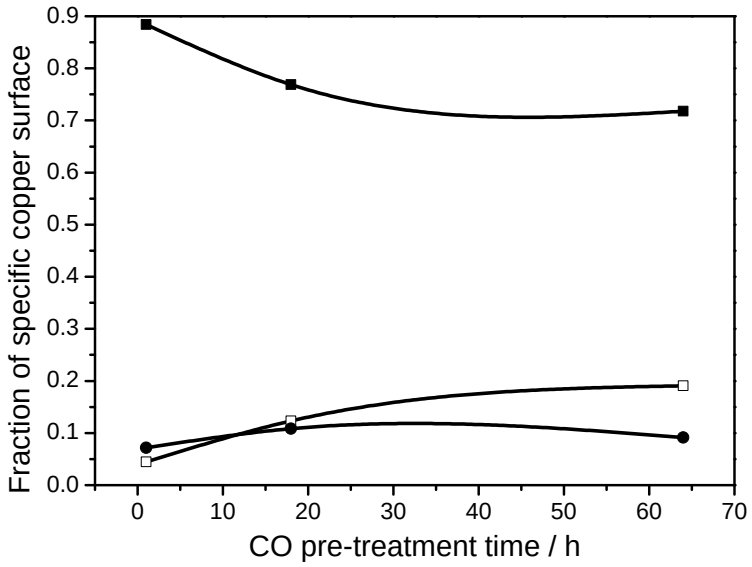

Figure 6.3: Morphology change due to differently long pre-treatments of the catalyst with CO/He, (■) Cu(111), (□) Cu(100) and (•) Cu(110).

6.4.2 Temperature-programmed surface reaction

Hinrichsen et al. [126] investigated the CO oxidation over the ternary copper catalyst. The CO oxidation was determined as rate determining/slow step during the water-gas shift and methanol synthesis reaction [10–14]. The following reaction scheme was implemented to describe the surface reaction:

$$CO_{(g)} + s_{hkl} \rightleftharpoons COs_{hkl} \tag{6.10}$$

$$COs_{hkl} + Os_{hkl} \rightleftharpoons CO_2s_{hkl} + s_{hkl} \tag{6.11}$$

$$CO_2s_{hkl} \rightleftharpoons CO_{2(g)} + s_{hkl} \tag{6.12}$$

All reactions are part of the redox mechanism and equilibrium reactions [10–14]. First, carbon monoxide adsorbs on the surface site s_{hkl}. The oxygenated surface was achieved by the method described before. Subsequently, the surface reaction proceeds *via* a Langmuir-Hinshelwood mechanism [127, 128]. After the reaction, carbon dioxide desorbs and is removed by the purging gas. The kinetics for the sorption steps 1 and 3 (equations 6.10 and 6.12) are calculated by the means of collision theory, assuming non activated adsorption. The site density for the surface atoms is taken from Evans et al. [129]. For the carbon monoxide a sticking coefficient of one was used, also suggested by

Domagala and Campbell [130] and Cox and Schulz [131]. For the molecular adsorption of carbon dioxide a sticking coefficient of one is assumed [15]. However, calculations with varying Arrhenius parameters of several magnitudes did not show any deviations for the resulting TPSR signals, neither for carbon monoxide nor for carbon dioxide. The equilibrium constants couple the rate constants in forward and reverse direction as follows:

$$K = \frac{k^+}{k^-} \tag{6.13}$$

For steps 1-3 (equations 6.10 - 6.12), the equilibrium constants are calculated by the means of statistical thermodynamics [61, 63]. Especially for the water-gas shift and methanol reaction this was explained in great detail elsewhere [10–14]. In our model the respective thermodynamic input for the partition functions was taken from references [11, 13] (see also Appendix).

This yields the following reaction rates for step 1 through 3:

$$r_{1,hkl} = k_{ads,1,hkl} p_{CO} p_0^{-1} \theta_{s,hkl} - k_{ads,1,hkl} / K_{1,hkl} \theta_{CO,hkl} \tag{6.14}$$

$$r_{2,hkl} = k_{2,hkl} \theta_{CO,hkl} \theta_{O,hkl} - k_{2,hkl} / K_{2,hkl} \theta_{CO_2,hkl} \theta_{s,hkl} \tag{6.15}$$

$$r_{3,hkl} = k_{ads,3,hkl} K_{3,hkl} \theta_{CO_2,hkl} - k_{ads,3,hkl} p_{CO_2} p_0^{-1} \theta_{s,hkl} \tag{6.16}$$

Now it is straightforward to define the differential equations for the surface species:

$$\frac{\partial \theta_{CO,hkl}}{\partial t} = r_{1,hkl} - r_{2,hkl} \tag{6.17}$$

$$\frac{\partial \theta_{CO_2,hkl}}{\partial t} = r_{2,hkl} - r_{3,hkl} \tag{6.18}$$

$$\frac{\partial \theta_{O,hkl}}{\partial t} = -r_{2,hkl} \tag{6.19}$$

The corresponding equation for the uncovered sites reads:

$$\frac{\partial \theta_{s,hkl}}{\partial t} = -r_{1,hkl} + r_{2,hkl} + r_{3,hkl} \tag{6.20}$$

which can also be calculated by a site balance according to:

$$\theta_{s,hkl} = 1 - \sum \theta_{i,hkl} \tag{6.21}$$

At high coverages of educts often lower apparent activation energies for reactions are observed. This apparent activation energy $E_{a,app}$ is given by the true activation energy E_a and the adsorption energy of the educts ΔH_{ads}:

$$E_{a,app} = E_a + \Delta H_{ads} \tag{6.22}$$

Usually the adsorption enthalpy is negative, which means the apparent activation energy is lowered by the modulus of ΔH_{ads}. In order to account for a coverage-depending

apparent activation energy between the limits of $E_{a,app}$ and E_a, a function in the form of $E_{a,eff} = f(\theta)$ is implemented. Keskitalo et al. [66] found the following mathematical expression to account for different types of dependencies:

$$f(\theta) = b + \frac{\ln(1+a) - \ln(\theta/\theta_{max} + a)}{\ln(1+a) - \ln(a)} \cdot (1-b) \tag{6.23}$$

Here, b represents the minimum of the function in the range of $0 \leq \theta/\theta_{max} \leq 1$, which is reached when θ equals θ_{max}, as shown in figure 6.4. The factor a describes the type of the dependence. For a higher than one, the dependence is almost linear, i.e. Temkin-like. The smaller the value of a, the greater the range, where the apparent activation energy is almost constant. On the other hand, the transition area is shifted towards smaller coverages and steeper slopes. For $\lim a \to 0$ a constant value of b is obtained, whereas for $b = 1$ always the maximum value is reached. A nonlinear coverage-relationship between the apparent and true activation energy E_a in the form of

$$E_{a,eff} = f(\theta) E_a \tag{6.24}$$

can be formulated.

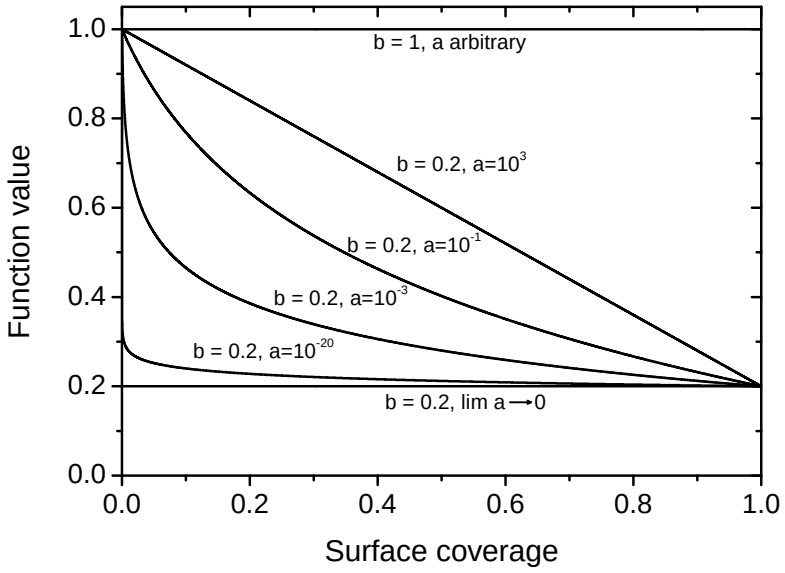

Figure 6.4: Logarithmic coverage-dependence based on information given in [66].

Finally coupling equation 6.23 and 6.24 yields for the effective activation energy:

$$E_{a,eff}(\theta) = E_a + \Delta H_{ads} \cdot \left(1 - \frac{\ln(1+a) - \ln(\theta/\theta_{max} + a)}{\ln(1+a) - \ln(a)}\right) \tag{6.25}$$

with

$$b = \frac{E_{a,2} + \Delta H_{ads}}{E_{a,2}} \tag{6.26}$$

This equation can now be used to describe the behavior of the experimental data. The factor a is, besides the kinetic parameters, subject of the model fit. However, only reasonable initial values for a were chosen, indicated by Habraken et al. [132] who found an almost constant apparent activation energy for wide ranges of θ_O. This means a should be very small to describe the experimental behavior.

As indicated in part one, different types of surface sites are involved in the kinetics when the catalyst is treated with a flow of carbon monoxide in helium. Therefore the contribution to the overall rate for gaseous species, $r_{total,i}$, can be written as:

$$r_{total,i} = \eta \cdot r_{100,i} + \epsilon \cdot r_{110,i} + (1 - \eta - \epsilon) \cdot r_{111,i} \tag{6.27}$$

where η is the ratio of sites on Cu(100) relative to the overall active sites and ϵ is the ratio of sites on Cu(110) relative to the overall active sites and $r_{total,i}$ can be interpreted as the average rate over an active site. Ovesen et al. [13] published the kinetic parameters for the surface reaction (equation 6.11) for the three low-index surface planes Cu(111), Cu(110) and Cu(100). These values were used as a starting point. Keeping the ratio of the Arrhenius parameters for different active sites constant, lowers the number of unknown kinetic parameters to only $A_{2,111}$ and $E_{a,2,111}$. When keeping the ratios of $k_{2,hkl}$ constant, essentially the same results were obtained. Furthermore, the fractions of the different surface sites were chosen to be 0.8 for Cu(111), 0.1 for Cu(110) and 0.1 for Cu(100). These numbers can be regarded as averaged extracted values from the pre-treated hydrogen desorption experiments after exposure to CO/He (see also section 6.4.1). Closer analysis of the kinetic constants found by Ovesen et al. [13] reveals that the Cu(100) structure has a much higher activation energy compared to the other two low-index planes. On the other hand the modulus of the adsorption enthalpy is low compared to the Cu(110) structure, which increases the apparent activation energy (see also equation 6.22). The higher activation energy means that the CO_2 signal is shifted to temperatures around 300 K, which is not related to the signal of the experiments. Hinrichsen et al. [126] and Genger [82] suggested to investigate the first signal; hence, we omitted this plane from our calculations, which could be confirmed by comparative simulations. The number of active sites per catalyst weight, N, was determined by Hinrichsen et al. [126] to yield 236 μmol·g_{cat}^{-1}. This corresponds to a N_2O consumption of 118 μmol·g_{cat}^{-1}. However, only about 30% of the provided oxygen was converted to yield carbon dioxide [126]. Integration for the molar coverage of oxygen was done for each experiment up to 275 K, corresponding to the first maximum of the measurement [126]. Table 6.2 gives an overview for the reactive oxygen and temperature intervals for SRMSE determination used in our computations. As a starting point, the catalyst was initialized by half a monolayer of oxygen, of which the previously mentioned amount was set to be active for CO oxidation. Furthermore at $t = 0$ s the coverage of carbon monoxide was

Table 6.2: Calculated amount of reactive oxygen for CO and O^* TPSR and SRMSE intervals for analysis.

Heating rate	$n_{O,reactive}$	SRMSE – Interval
K·min^{-1}	μmol·g$_{cat}^{-1}$	K
6	35.9	160 - 240
10	29.7	160 - 250
15	26.9	160 - 250

set to a value of $\theta_{CO} = 0.5$, which enhances the computational time significantly. This is physically reasonable as for low starting temperatures, i.e. $T = 160\,\mathrm{K}$, the adsorbed state is highly preferred. Reference calculations show a coverage of 0.5 way before the surface reaction starts, when the flow is switched from pure He to the CO/He mixture.

Figure 6.5 shows the respective simulated and experimental responses, when assuming complete back-mixing (CSTR). The PFR model yields the same signal of CO_2 in the outlet flow, with an SRMSE value below $4{\cdot}10^{-3}$, when comparing the modeled signals. As can be seen, the agreement between simulation and experiment is very high. This can be confirmed by SRMSE values below 0.04. The corresponding kinetic constants are displayed in table 6.3. The factor a results in a low value of $4.4{\cdot}10^{-12}$, which was expected to accurately describe the experiments.

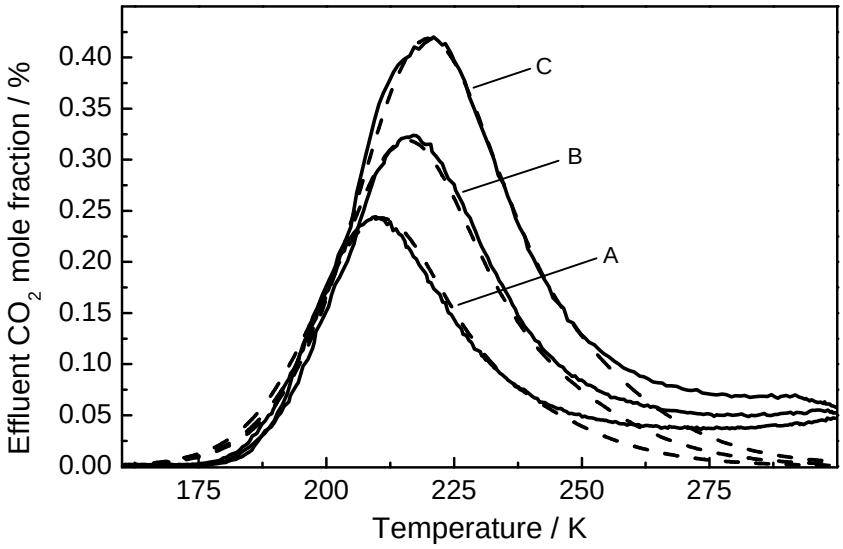

Figure 6.5: Experimental TPSR of CO and O^* spectra (solid) and simulated curves (dashed), using different heating rates, (A) $\beta = 6\,\mathrm{K{\cdot}min^{-1}}$ (SRMSE = 0.038), (B) $\beta = 10\,\mathrm{K{\cdot}min^{-1}}$ (SRMSE = 0.037), (C) $\beta = 15\,\mathrm{K{\cdot}min^{-1}}$ (SRMSE = 0.021). Experimental conditions: $Q_{CO/He} = 10\,\mathrm{Nml{\cdot}min^{-1}}$, $\omega_{cat} = 0.2\,\mathrm{g}$.

Since no reaction takes place, the activation energy is low and constant at the beginning of the experiment (figure 6.6). The simulated CO_2 signal ascends around $T = 170\,\mathrm{K}$ and the activation energy for Cu(111) does not change by more than 10% until 90% of

Table 6.3: Parameters derived from CO and O^* TPSR at different heating rates.

Parameter	Value	95% confidence interval	Re-Parameterized
$E_{a,2,111}$ / (kJ·mol^{-1})	83.4	± 1.6	83.4
$\ln(A_{2,111})$ / s^{-1}	15.4	± 1.0	$4.9{\cdot}10^{6}$
$a = 10^{-parameter}$	11.4	± 1.3	$4.4{\cdot}10^{-12}$
$E_{a,2,110}$ / (kJ·mol^{-1})	-	-	98.6
$A_{2,110}$ / s^{-1}	-	-	$8.0{\cdot}10^{6}$
$E_{a,2,100}$ / (kJ·mol^{-1})	-	-	100.3
$A_{2,100}$ / s^{-1}	-	-	$8.0{\cdot}10^{6}$

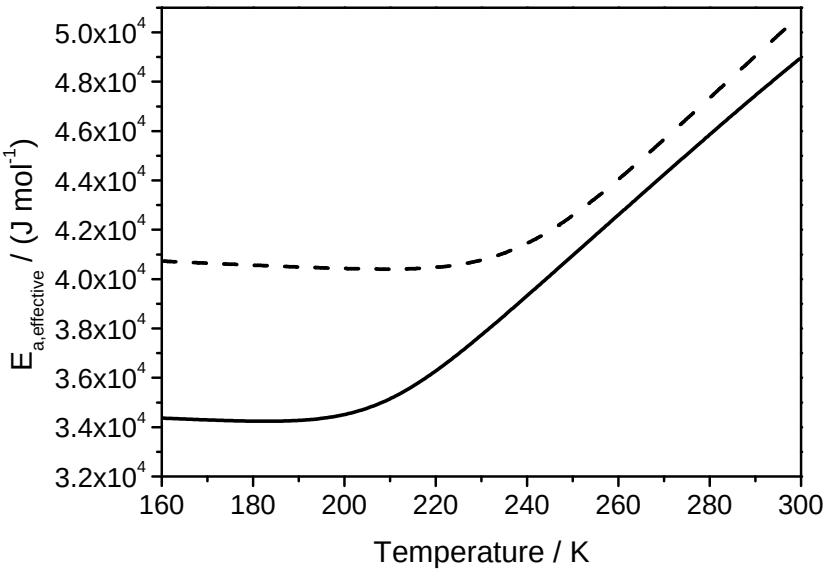

Figure 6.6: Trend of apparent activation energy for Cu(111) (solid) and Cu(110) (dashed). Experimental conditions: $Q_{CO/He}$ = 10 Nml·min^{-1}, ω_{cat} = 0.2 g.

the reactive oxygen is removed *via* the surface reaction. Subsequently, the activation energy is further slightly rising. The remaining (reactive) oxygen coverage is about $5{\cdot}10^{-5}$ on Cu(111), hence the apparent activation energy does not reach the limit E_a in our elevated temperature interval.

The effective activation energy for Cu(111) is smaller than for Cu(110), thus the reaction first proceeds over Cu(111). At the end of the experiment, the signal levels off. This was mainly attributed to the CO oxidation by reduction of the ZnO [82]. Figure 6.7 shows the contributions from Cu(111) and Cu(110) and for completeness also Cu(100) planes, which are omitted in the calculation of the first maximum. It can be seen that the Cu(100) structure is not involved during the evaluated temperature range, but partly responsible for the tail, resulting in a second maximum. However, this effect

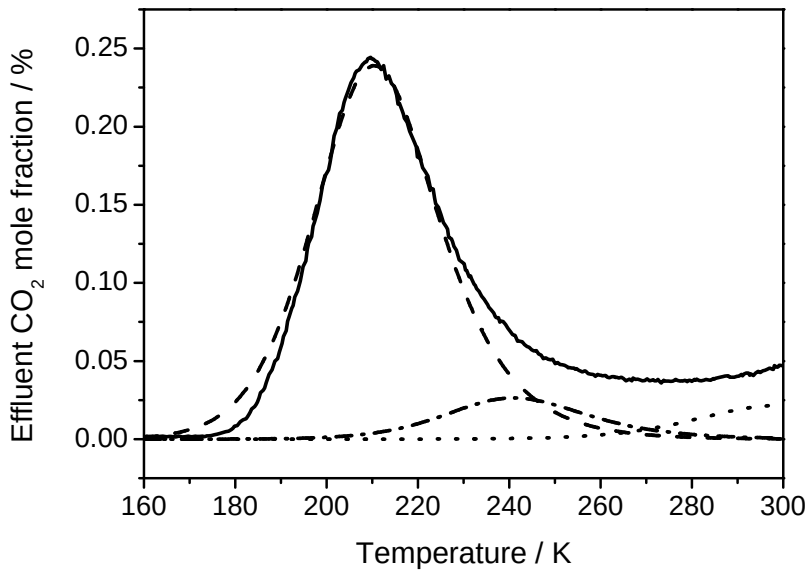

Figure 6.7: Experimental TPSR of CO and O^* spectra (solid) and simulated curves. Contributions from different copper facets: Cu(111) dashed, Cu(100) dotted and Cu(110) dashed dotted. Experimental conditions: $Q_{CO/He} = 10\,\mathrm{Nml{\cdot}min^{-1}}$, $\omega_{cat} = 0.2\,\mathrm{g}$.

cannot be separated from ZnO reduction and therefore a discussion is not reasonable and the exception of this planes seems to be adequate [82].

Figure 6.8 shows the coverage of the surface intermediates as a function of the temperature. It can clearly be seen that the second maximum is not due to re-adsorption of CO_2 as the amount of adsorbed CO_2 is very low, i.e. for $\beta = 6\,\mathrm{K \cdot min^{-1}}$ and Cu(111) below 10^{-7}. This can be explained by the highly competitive adsorption of carbon monoxide and the sorption equilibrium of carbon dioxide, the latter being almost completely on the gas phase for the evaluated temperature interval. The amount of adsorbed (reactive) oxygen drops when the temperature reaches about 170 K and the surface reaction starts. At the same time the coverage of carbon monoxide rises, which corresponds to a strong adsorption at this temperature and the oxygen being irreversibly removed. Subsequently, the coverage of carbon monoxide starts to drop at a temperature around 250 K since at this temperature desorption of carbon monoxide quantitatively takes place.

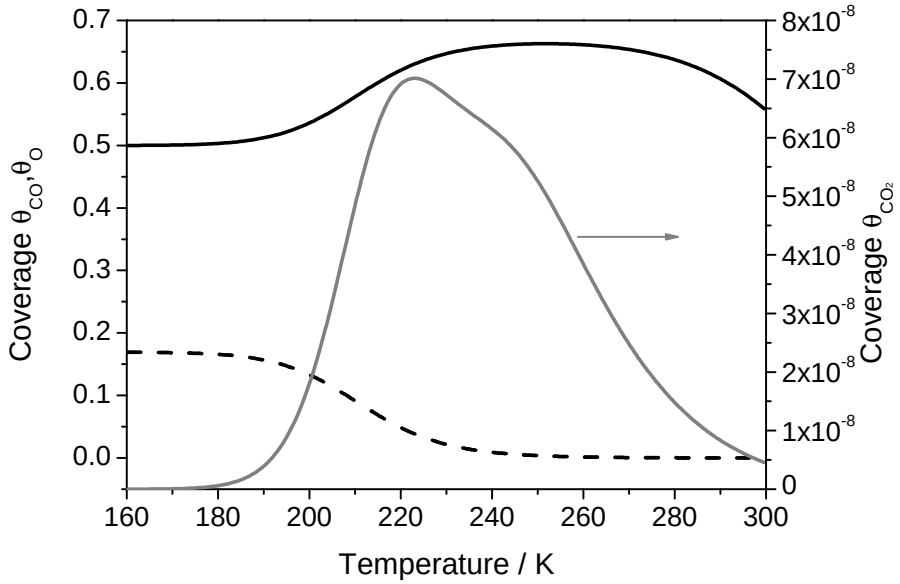

Figure 6.8: Trend of surface coverages, θ_{CO} (solid, black), reactive θ_O (dashed, black) and θ_{CO_2} (solid, grey). Experimental conditions: $Q_{CO/He}$ = 10 Nml·min^{-1}, ω_{cat} = 0.2 g.

6.5 Discussion

In a recent paper the desorption kinetics from a ternary copper catalyst were studied in great detail [103]. Hereby, it was found that the catalyst mainly exposed Cu(111) planes, which is consistent with other literature studies [102, 112, 113]. Furthermore, we could show that a coverage-depending activation energy can give a quantitative good fit for different hydrogen surface coverages as well as for a fresh and an aged catalyst. Hence it is straightforward to conclude that the (reversible) changes in the shape of the desorption spectra observed by Wilmer and Hinrichsen [41] originate from a dynamical change of the copper catalyst. In our modeling approach we implemented two new copper facets to describe the experimental spectra. Upon a carbon monoxide pre-treatment, Sakakini et al. [133] proposed, besides Cu(110), an increasing fraction of Cu(211) being exposed. However, the Topsøe group used *in-situ* methods, such as EXAFS and TEM to study the dynamic changes in the catalyst morphology [24, 25, 28, 29]. They found the most stable surface planes being exposed to be (100), (110) and (111). Under reducing conditions, a reversible change in the exposed low-index copper facets was observed. These results were also described using the Wulff construction [25] and could be implemented into a microkinetic model [13]. Anger et al. [111] studied the temperature-programmed desorption of hydrogen from copper single crystal under UHV conditions. Hereby, only kinetic values for Cu(111) and Cu(110) could be determined since surface reconstruction over Cu(100) limited their analysis. Coverage-dependent activation energies for Cu(111) and Cu(110) were found. In our calculations we did not include coverage-dependencies for the Cu(110) and Cu(100) planes. Therefore, the extracted parameters in table 6.1 can be seen as mean values for the different surface planes and are well in the range of previous reported parameters for Cu(111) [102, 103, 111–113]. The trend

for the exposed surface planes shows that under mild reaction conditions the catalyst mainly exposes Cu(111), while the catalyst underlies morphology changes under strong reducing conditions, with rising amounts of Cu(110) and Cu(100). This is consistent with previously observed transient methanol production rates [29, 41]. Reducing pre-treatments before methanol synthesis showed transient maxima in the methanol production. This can be correlated to our experiments by the findings of Ovesen et al. [13]. The different low-index planes have rising activities in methanol synthesis, in the order Cu(111) < Cu(100) < Cu(110). We could show, that a reducing pre-treatment increases the amount of the highly active 110 and 100 structures, which leads to a higher methanol production rate [13]. This is independent from proposed highly active ZnO_x, which additionally enhances the methanol production rate [24, 41]. The results are also in good qualitative agreement with the surface plane distribution calculated by the Wulff construction [13, 25]. The crystal structure is described in dependence of the contact-surface free energy and the gaseous environment, however, with the limitation that it is always restricted by one copper low-index plane bound to the ZnO interface and the surface free energies of the unbound facets used in the Wulff construction of the crystal. For 64 h pre-treatment almost similar ratios of exposed copper planes for reducing conditions ($\gamma/\gamma_0 < 0$) can be found. Only for extreme low values of γ/γ_0 the ratios are remarkably different. Except for these low values of the contact-surface free energy, the Cu(111) planes always exhibit a higher fraction than Cu(110) and Cu(100), which is consistent with our results. However, Vesborg et al. [29] found that only a mixture of hydrogen and carbon monoxide may lead to extreme low values of γ/γ_0. Under working conditions copper binds to the substrate *via* all kind of planes, suggesting that the real crystal structure is a mixture from all planes being able to bind with the ZnO. Our ratios are extracted under working conditions; therefore one may conclude that they can be interpreted as mean values. Hansen et al. [28] found an activation of Cu(100) for a carbon monoxide atmosphere, which is in good agreement for our experiments with rising pre-treatment time up to 64 h. This long pre-treatment may be assigned to an equilibrated reconstruction, as the shape of a 62 h and 64 h pre-treated catalyst is essentially constant [41].

The parameter estimation of the carbon monoxide pre-treatment shows great agreement between experiment and simulation. The shapes and the position of the temperature maximum are reproduced quite exactly. The assumption of coverage-independent adsorption enthalpies may explain the small deviations at the onset of the signal for all spectra. At the beginning of the experiments, the catalytic active surface is completely covered with oxygen and carbon monoxide. This limiting case leads to a maximum of interaction between the adsorbed molecules, leading to different influences on the binding of the adsorbates, which may also influence the adsorption energy. However, this assumption did not influence the quality of the extracted data. The pre-exponential factor extracted in this study is in reasonable agreement with a factor of $6 \cdot 10^5\,s^{-1}$ to $1 \cdot 10^6\,s^{-1}$, determined by Genger [82], assuming pseudo first-order kinetics and plotting $\ln(T_{max}^2/\beta)$ against $1/T_{max}$. The introduced logarithmic coverage-dependence of the activation energy leads to a behavior described by Habraken et al. [132], where the

apparent activation energy was found to be essentially constant for a large range of θ_O. Figure 6.7 shows the contributions of the different surface planes to the signal in the outlet flow. Only Cu(111) and Cu(110) contribute to the measured signal, the tailing is mainly caused by ZnO reduction and surface reaction over Cu(100). However, as these two effects cannot be separated, they are not taken into account in this study. Besides, the lower reactivity over Cu(100) was already outlined before [15, 132, 134, 135]. The second shoulder could also be caused by re-adsorption effects. However, as seen in figure 6.8, the surface concentration of carbon dioxide is very low ($< 1{\cdot}10^{-7}$). This is caused by a highly competitive adsorption between carbon monoxide and dioxide. The equilibrium of gas-phase and adsorbed carbon dioxide is almost completely on the gas phase for evaluated temperatures. The activation energy of the oxidation step over Cu(111) is with a value of $83.4 \pm 1.6\,\mathrm{kJ{\cdot}mol^{-1}}$ in reasonable agreement with values obtained in previous studies [82, 126, 135–137]. Habraken et al. [135] determined a value of 79 to $84\,\mathrm{kJ{\cdot}mol^{-1}}$, independent from the crystal structure. Gokhale et al. [137] calculated a value of $79\,\mathrm{kJ{\cdot}mol^{-1}}$ for Cu(111), using density functional theory. Nakamura et al. [136], Hinrichsen et al. [126], Genger [82] and Habraken et al. [132] reported apparent activation energies in the range of 28 to $33.5 \pm 2.5\,\mathrm{kJ{\cdot}mol^{-1}}$, which makes it difficult to compare. However, when we use equation 6.22 to calculate the apparent activation energy of Cu(111) for our experiments we obtain a value of $34.4 \pm 1.6\,\mathrm{kJ{\cdot}mol^{-1}}$ in reasonable agreement with previously reported ones. Campbell et al. [138] reported a value of $79\,\mathrm{kJ{\cdot}mol^{-1}}$ for Cu(110) comparable to Cu(111), however Ovesen et al. [13] later introduced structure sensitivity in their microkinetic model of methanol synthesis. They published a very low activation energy for Cu(111) of $72\,\mathrm{kJ{\cdot}mol^{-1}}$ and activation energies being 13 and $15\,\mathrm{kJ{\cdot}mol^{-1}}$ higher for Cu(110) and Cu(100) compared to their value for Cu(111). We used this difference in reactivity as model basis. The activation energies of Cu(100) and Cu(110) presented here are higher than reported in literature, but both signals are subject to tailing effects, which originate from the reduction of zinc oxide, and their fraction on the overall active surface is very low in our calculations. Therefore, we constrained the model only to optimize the Arrhenius parameters with respect to the Cu(111) plane. The results are still reasonable when only Cu(111), corresponding to equal kinetics for all low-index planes, is considered (indicated by figure 6.7). The differences in the resulting Arrhenius parameters are in the range of the parameter confidence intervals.

To summarize, the experimental approach by Wilmer and Hinrichsen [41], combined with the evaluation presented here may act as a simple fingerprint method to investigate the intrinsic activity of different methanol synthesis catalysts. Since methanol synthesis comprises structure sensitive reaction steps [13, 139], e.g. the oxidation of carbon monoxide, the distribution of the different copper surface planes is supposed to have a significant influence on the catalysts activity. Recently, Kaluza et al. [140] studied a novel synthesis route for ternary copper catalysts. Their continuous approach led to a catalyst which showed a 50% higher copper area-related activity than the commercial reference catalyst employed in their study. It would be interesting to study these catalysts by our method in order to understand the differences in the methanol synthesis

activity regarding structure-activity relationship. Moreover, other pre-treatments than CO/He could reveal even further reconstruction effects, i.e. a mixture of CO and H_2, as suggested by Vesborg et al. [29]. Concerning the deactivation behavior of catalysts for methanol synthesis, pre-treatments with oxidizing gases, i.e. carbon dioxide or water, and subsequent evaluation as presented here may further guide experiments to design a more stable catalyst for methanol synthesis.

6.6 Conclusions

Temperature-programmed flow experiments were used to model the interaction of carbon monoxide with a ternary copper catalyst under ambient pressure. CO/He treatment prior to hydrogen temperature-programmed desorption experiments showed that the copper catalyst underlies dynamic morphology changes. Cu(100) and Cu(110) were found to be activated during such a procedure, with slightly different desorption parameters than on Cu(111). The ratio of the exposed surface planes changes during such a pre-treatment, which is in good agreement with the maximum in the methanol production rate. The kinetics of carbon monoxide oxidation over different copper low-index planes, an important step in water-gas shift and methanol synthesis reaction, was studied in some detail and exhibited a logarithmic coverage-dependence on oxygen. The new parameters of hydrogen desorption and the surface reactions could enhance the performance of microkinetic models, especially when experimental conditions are changed and different crystal surfaces are involved. The extracted parameters may help to enhance the bridging of the *pressure* and *material gaps* between UHV and industrially important process conditions.

7 Closing

7.1 Summary

In chemical engineering surface science studies are essential for catalyst design and process development. Hereby, microkinetic analysis can significantly improve the knowledge about these issues. In this thesis microkinetic analysis is applied at a *mesoscopic* scale concerning the methanol synthesis over the industrially applied $Cu/ZnO/Al_2O_3$ catalyst. Methanol becomes increasingly important as a chemical energy carrier and thus improvements of the knowledge about the catalysts morphology, surface reactions and catalyst deactivation are issues of great interest.

This work describes the overall kinetics of methanol synthesis, including the water-gas shift reaction, over a ternary $Cu/ZnO/Al_2O_3$ catalyst with differently detailed models, two global models, a power law and a Langmuir-Hinshelwood-Hougen-Watson model (LHHW), and a *surface-science* based microkinetic approach. Experimental conditions ranged from 5 to 60 bar and temperatures from 463 to 523 K at varying feed gas composition. All models give good qualitative agreement between simulation and experiment. The global models however, can predict the rates of methanol synthesis very precisely, when nine parameters are freely varied. The power law, which is the commonly applied type of model, does not allow physically meaningful conclusions, since there are many different mathematical formulations which may lead to a sufficient model fit. Different driving forces for the water-gas shift reaction and hence reaction orders were found to yield essentially the same results concerning the integral rate of methanol formation. A sensitivity analysis shows high sensitivities on the methanol formation rate for the respective reaction orders of hydrogen, carbon dioxide and water. The adapted LHHW model is based on a specific reaction mechanism and furthermore constrained by physico-chemical restrictions, i.e. resulting from the adsorption of species. This leads to slightly less precise simulation results, however, the mechanism incorporated provides a suggestion for the driving forces of such reactions. The highest sensitivities are observed for the equilibrium constant of hydrogen adsorption. This high sensitivity is somehow consistent with the results of the power law, however, it should be noted that physical conclusions for the power law must be treated with care. Upon model extrapolation both global models are essentially equal. The high model experiment conformability of both models shows why such models are often used in chemical engineering issues, i.e. diffusional investigation or reactor design.

Furthermore, the microkinetic model adapted from literature provides some theoretical insights on the surface chemistry of the methanol synthesis. The model comprises 13 elementary steps, while four reactions are assumed to be rate determining. The water-gas shift reaction is represented by a redox mechanism, similar to the LHHW model, while

methanol is formed by the succesive hydrogenation of carbon dioxide. The reaction is furthermore assumed to be structure sensitive, with increasing reaction rates over Cu(111), Cu(100) and Cu(110). Furthermore, dynamical morphology changes are incorporated in this model, which are suggested from experiments. A good agreement between the experimental results and model predictions is obtained. The microkinetic model comprises parameters obtained in a huge set of independent (ultrahigh vacuum, UHV) experiments, concerning mechanistics, thermodynamic properties and kinetic constants. It is shown that variation of only two parameters, i.e. the pre-exponential factor and the activation energy of the hydrogenation of H_2COO_{ads}, is sufficient to obtain good modeling results, which underlines the robustness of this model. Optimizing these variables on a *mesoscopic* scale gives parameters which are valid over a wide range of experimental conditions. A sensitivity analysis shows that at low pressures the rate of methanol formation may be inhibited by the water-gas shift reaction, as it proceeds in the reverse reaction, forming water and CO. At high CO to CO_2 ratios the water-gas shift reaction limits the methanol formation, since methanol is formed *via* the hydrogenation of carbon dioxide and carbon monoxide only acts as a secondary educt. In these cases, the rate limiting step in terms of the water-gas shift reaction is the conversion of surface CO and oxygen to yield surface carbon dioxide. For all experiments evaluated the highest sensitivity for methanol synthesis is obtained for the hydrogenation of H_2COO_{ads}.

The dynamical changes of the ternary catalyst are further studied using the valid microkinetic model. It is shown that a tremendous change in the amount of active sites is pronounced along the catalytic reactor. The amount of active sites drops significantly when the highly reducing synthesis gas is converted to methanol as water evolves as a side product. Furthermore, the distribution of the different active low-index planes, Cu(111), Cu(110) and Cu(100) is changed, which leads to a less active catalyst, as Cu(111) becomes the dominant facet. From literature it is known that these crystal planes are less active in methanol synthesis. The negative effect of water is outlined by the microkinetic model, and, surprisingly the power law model does not work without the inclusion of the water partial pressure. Again, it has to be noted that from the power law approach alone it is not save to conclude this inhibiting effect. Upon extrapolation the microkinetc model differs from the global reaction models, comprising a lower maximum reaction rate, which is pronounced by the dynamical behavior of the copper containing catalyst. However, the same temperature at the maximum methanol formation rate is observed for all models. Above this temperature the influence of the equilibrium becomes dominant and the rate of methanol formation drops.

The microkinetic model further allows to study the deactivation of the copper catalyst. From literature it is known that the activity for methanol synthesis drops significantly within the first hours of operation, while it only slightly decreases after this period. Hereby, deactivation is mainly attributed to thermal sintering and catalyst poisoning. When gases of high purity or several gas purification steps before the synthesis reaction are used, usually only thermal sintering is assumed. The microkinetic model shows a linear relationship between active copper surface area and activity

for methanol formation, which is consistent with experimental studies. Interestingly, the proportionality factor does not equal one. When the copper surface area is lowered by a specific amount, methanol formation drops less than the respective change in the copper surface area. This can be explained by the dynamical morphology changes, as the synthesis gas becomes more reductive when less methanol is formed and hence less water is produced. The local influence of the gas atmosphere on the catalysts morphology increases the number of active sites and in particular the amount of exposed highly active Cu(110) planes. Therefore, the rate of methanol formation is less inhibited and some of the loss in copper surface area can be compensated. The rate of water formation is even less dependent on the amount of catalytically active sites, since it is not only formed by the methanol formation from carbon dioxide, but also removed *via* the water-gas shift reaction. As both reactions become slower when lowering the amount of active sites the rate of water formation is less affected.

Incorporation of thermal sintering and irreversible morphology changes leads to an initial deactivation behavior which is consistent with the observations presented in literature studies. Those irreversible morphology changes may originate from adsorption of gas-phase molecules or reaction intermediates. It was proposed in literature that methanol feed gas with a high CO content deactivate faster than feed gases with a low CO-to-CO_2 ratio. This effect was related to a possible over-reduction of the copper catalyst. When it is assumed that the irreversible morphology changes are more pronounced for high CO-to-CO_2 ratios, this effect can easily be modeled. Oxidizing species may affect the catalysts morphology more, when the catalyst is over-reduced by a highly reducing feed gas. The results clearly show that this may have a tremendous effect on the deactivation behavior of copper catalysts.

The morphology effects are further studied by modeling hydrogen temperature-programmed desorption experiments from $Cu/ZnO/Al_2O_3$ catalysts under ambient pressure. It is known from literature that CO pre-treatment before hydrogen TPD leads to unsymmetrical signals, whereas for untreated or syngas treated catalysts a very symmetrical signal is obtained, mainly exposing Cu(111) active sites.

In a first step, hydrogen desorption from a fresh catalyst and one deactivated during methanol synthesis is studied. Hereby, different heating rates and initial coverages are considered. Before analyzing the kinetics in terms of A_{des} and E_{des}, it is shown that mass transport limitations are negligible under the evaluated conditions. Possible effects of re-adsorption on the resulting signal are presented, which may shift or broaden the resulting signal. Furthermore, different reactor models, a continuously stirred-tank reactor, a plug flow reactor and a convection-axial dispersion reactor model, also comprising intra-particle mass transfer, are evaluated. It is shown that there is only a negligible effect on the hydrogen signal in the outlet flow. Furthermore, a published criterion for possible intra-particle mass transfer limitations, which relates the convective to the diffusive flow, can safely be enlarged when re-adsorption is a highly activated process.

Different analysis methods for temperature-programmed experiments are applied and compared, namely an analysis using a fixed pre-exponential factor, heating rate variation, lineshape analysis and a full analysis including coverage-dependence. The first three methods can only be applied when transport limitations can be excluded. Furthermore, *ad hoc* it cannot be said whether the obtained parameters are physically meaningful. An analysis with a fixed pre-exponential should not be applied to extract activation energies of desorption, when the pre-exponential factor is unknown and hence fixed at $10^{13}\,s^{-1}$. Heating rate variation and lineshape analysis at an intermediate coverage led to physical reasonable values. Furthermore, from a modeling point of view, all derived parameters show good agreement when modeling the experiments, except for the ones obtained by the lineshape analysis at full coverage of hydrogen. However, the standard techniques are based on Langmuirian assumptions, which leads to too narrow TPD signals. Subsequently, a full analysis with a coverage-dependent activation energy of desorption showed a great agreement between model and experiments. Reasonable initial values should guide such a model fit, i.e. from heating rate variation. The parameters are well in the range of published kinetic values for thermal desorption spectroscopy (TDS) experiments from Cu(111), which was also observed by other research groups for such ternary copper catalysts. Furthermore, the TPD signals from a fresh catalyst and deactivated catalyst do not differ in shape, onset or temperature of the signal maximum, but only in the amount of desorbing hydrogen. Hence it is straightforward to conclude that in this case only the number of active sites is decreased and no morphology changes are present under the evaluated conditions.

As stated above, the shape of the resulting hydrogen signals is changed when the catalyst is flushed with carbon monoxide. Rising pre-treatment times showed a broadening of the resulting signals, until a second maximum evolves after 62 to 64 h of pre-treatment [41]. In this study it is shown that the inclusion of Cu(110) and Cu(100) can explain this deviations from the symmetrical signals obtained for a fresh catalyst. A model fit with a fixed pre-exponential factor and varying activation energy and amount for the respective copper planes, while keeping the kinetic values for Cu(111) fixed from the previous analysis, leads to a good agreement between model and experiment. Physical reasonable values for the desorption kinetics are obtained. It is shown that Cu(110) and Cu(100) get activated upon such a pre-treatment, which can explain the transient maxima in methanol synthesis for CO pre-treated catalysts, as Cu(110) and Cu(100) are more active in methanol synthesis than Cu(111) [13]. Besides, this analysis shows reasonable agreement with results from *in-situ* EXAFS and TEM experiments for binary Cu/ZnO model catalysts and may therefore suggest that the morphology changes are also present for a high copper loading and hence closer to working conditions.

Finally, the CO induced changes in the catalysts morphology are further used for modeling the temperature-programmed surface reaction of CO with pre-adsorbed oxygen over a ternary copper catalyst. This reaction is one of the rate determining steps during water-gas shift and hence methanol synthesis reaction, which is found to inhibit or limit the methanol synthesis for low pressures or feeds with a high CO-to-CO_2 ratio, respectively. It is known from literature that this reaction shows a constant low apparent

activation energy for a wide range of oxygen coverages, hence a coverage-dependent activation energy was included in the modeling approach. A logarithmic type of coverage-dependence leads to good modeling results. The results may further enhance the knowledge about a crucial reaction on the copper surface, especially with changing reaction conditions over a wide spectrum of experimental conditions.

7.2 Outlook

The microkinetic approach used in this study is shown to enhance the knowledge and to reveal issues of high relevance in methanol synthesis over $Cu/ZnO/Al_2O_3$ catalysts. Besides, the very precise global kinetic models can further be applied for studying diffusion limitations or reactor design issues.

The findings strongly suggest further research about the active sites in methanol synthesis. Especially possible morphology changes under high pressure should further be studied in more detail. In particular the influence of adsorbates on the surface free energy of copper under high pressure conditions could be considered for the Wulff construction. However, further experimental studies are required. The results from modeling the hydrogen temperature-programmed desorption from CO pre-treated catalysts support the presence of the morphology changes, further experiments with a combined hydrogen carbon monoxide pre-treatment could enhance the understanding of such a re-structuring. It was suggested that a H_2-to-CO ratio of 1:1 could further reduce the copper zinc oxide interface. Pre-treatments with other adsorbates, i.e. water, carbon dioxide or even methanol, should be applied to study the influence of these gas-phase molecules. When these experiments are further evaluated by the methods presented in this thesis, it could be possible to find a better relationship between the gas phase and catalyst morphology. The microkinetic model suggests especially to investigate water induced structural changes in more detail. In this context the influence of gas-phase methanol is up to now completely neglected and such studies could easily prove a possible influence. Furthermore, strain effects are presently not considered in the microkinetic model, however, the model experiment conformability may further be enhanced when such effects are accounted for.

The microkinetic model is a very versatile tool for studying the deactivation of the ternary copper catalyst. Many different modeling approaches can easily be implemented in such a model. This is already demonstrated by the inclusion of structural changes due to gas-phase molecules or surface intermediates, which may further enhance the initial deactivation of the catalyst. A comprehensive deactivation study, including TEM imaging and surface area measurements before, during and after reaction is highly suggested. Hereby, the surface area should not only be measured by the commonly applied N_2O frontal chromatography, but also by hydrogen TPD to check for possible morphology changes. Incorporation of a detailed sintering mechanism into the microkinetic model could then lead to a proper description of the drop in activity. Changes of interfacial energies between copper and the oxidic support as a function

of the gas atmosphere might also affect the rate of sintering processes. Besides, the impact of the catalyst formation period on the overall deactivation progress, especially on the steady state activity, should be investigated.

The methods presented in this study can further serve as basic tools to study other processes, i.e. methanol steam reforming, or even processes occuring on other surfaces than copper, i.e. methanisation over nickel.

A Appendix

A.1 Thermodynamic data

Table A.1: Thermodynamic data, adsorbed species on Cu(110) [10–13].

Species	Vibrational parameters	Ground state energy
CH_3O*	$\omega_\perp = 400\,\mathrm{cm^{-1}}$, $\omega_\parallel = 37(2)\,\mathrm{cm^{-1}}$, $\omega_{rot} = 360(3)\,\mathrm{cm^{-1}}$, $\psi = 1020, 1150(2), 1460(3), 2840, 2940(2)\,\mathrm{cm^{-1}}$	-300 kJ·mol^{-1}
CH_3OH*	$\omega_\perp = 290\,\mathrm{cm^{-1}}$, $\omega_\parallel = 36(2)\,\mathrm{cm^{-1}}$, $\omega_{rot} = 360(3)\,\mathrm{cm^{-1}}$, $\psi = 750, 820, 1030, 1150(2), 1470(3), 2860, 2970(2), 3320\,\mathrm{cm^{-1}}$	-413 kJ·mol^{-1}
CO_2*	$\omega_\perp = 410\,\mathrm{cm^{-1}}$, $\omega_\parallel = 14(2)\,\mathrm{cm^{-1}}$, $\psi = 667(2), 1343, 2349\,\mathrm{cm^{-1}}$	-463 kJ·mol^{-1}
H_2COO*	$\omega_\perp = 405\,\mathrm{cm^{-1}}$, $\omega_\parallel = 30(2)\,\mathrm{cm^{-1}}$, $\omega_{rot} = 400(3)\,\mathrm{cm^{-1}}$, $\psi = 630, 960, 1090, 1220(2), 1420, 1480, 2920, 3000\,\mathrm{cm^{-1}}$	-568 kJ·mol^{-1}
H_2O*	$\omega_\perp = 460\,\mathrm{cm^{-1}}$, $\omega_\parallel = 21(2)\,\mathrm{cm^{-1}}$, $\psi = 745, 1600, 3370, 3370\,\mathrm{cm^{-1}}$	-365 kJ·mol^{-1}
O*	$\omega_\perp = 391\,\mathrm{cm^{-1}}$, $\omega_\parallel = 508(2)\,\mathrm{cm^{-1}}$	-243 kJ·mol^{-1}
OH*	$\omega_\perp = 280\,\mathrm{cm^{-1}}$, $\omega_\parallel = 670(2)\,\mathrm{cm^{-1}}$, $\psi = 3380\,\mathrm{cm^{-1}}$	-319 kJ·mol^{-1}
H*	$\omega_\perp = 1291\,\mathrm{cm^{-1}}$, $\omega_\parallel = 157(2)\,\mathrm{cm^{-1}}$	-29** kJ·mol^{-1}
HCOO*	$\omega_\perp = 322\,\mathrm{cm^{-1}}$, $\omega_\parallel = 36(2)\,\mathrm{cm^{-1}}$, $\omega_{rot} = 400(3)\,\mathrm{cm^{-1}}$, $\psi = 758, 1331, 1640, 2879, 1073, 1377\,\mathrm{cm^{-1}}$	-561 kJ·mol^{-1}
CO*	$\omega_\perp = 342\,\mathrm{cm^{-1}}$, $\omega_\parallel = 17(2)\,\mathrm{cm^{-1}}$, $\psi = 2088\,\mathrm{cm^{-1}}$	-190 kJ·mol^{-1}

** Extracted from reference [103], original value 27 kJ·mol^{-1}, well in the range of reported accuracy (3 kJ·mol^{-1}) [12, 13]; ω are frustrated translational parameters; ψ are vibrational constants; the number in parentheses denotes the degeneracy of a specific frequency.

Table A.2: Thermodynamic data, adsorbed species on Cu(111) and Cu(100) [10–13].

Species	Vibrational parameters	Ground state energy
CH_3O*	$\omega_\perp = 400\,\mathrm{cm^{-1}}$, $\omega_\parallel = 37(2)\,\mathrm{cm^{-1}}$, $\omega_{rot} = 360(3)\,\mathrm{cm^{-1}}$, $\psi = 1020, 1150(2), 1460(3), 2840, 2940(2)\,\mathrm{cm^{-1}}$	-300 kJ·mol^{-1}
CH_3OH*	$\omega_\perp = 290\,\mathrm{cm^{-1}}$, $\omega_\parallel = 36(2)\,\mathrm{cm^{-1}}$, $\omega_{rot} = 360(3)\,\mathrm{cm^{-1}}$, $\psi = 750, 820, 1030, 1150(2), 1470(3), 2860, 2970(2), 3320\,\mathrm{cm^{-1}}$	-413 kJ·mol^{-1}
CO_2*	$\omega_\perp = 410\,\mathrm{cm^{-1}}$, $\omega_\parallel = 14(2)\,\mathrm{cm^{-1}}$, $\psi = 667(2), 1343, 2349\,\mathrm{cm^{-1}}$	-463 kJ·mol^{-1}
H_2COO*	$\omega_\perp = 405\,\mathrm{cm^{-1}}$, $\omega_\parallel = 30(2)\,\mathrm{cm^{-1}}$, $\omega_{rot} = 400(3)\,\mathrm{cm^{-1}}$, $\psi = 630, 960, 1090, 1220(2), 1420, 1480, 2920, 3000\,\mathrm{cm^{-1}}$	-568 kJ·mol^{-1}
H_2O*	$\omega_\perp = 460\,\mathrm{cm^{-1}}$, $\omega_\parallel = 21(2)\,\mathrm{cm^{-1}}$, $\psi = 745, 1600, 3370, 3370\,\mathrm{cm^{-1}}$	-359 kJ·mol^{-1}
O*	$\omega_\perp = 391\,\mathrm{cm^{-1}}$, $\omega_\parallel = 508(2)\,\mathrm{cm^{-1}}$	-243 kJ·mol^{-1}
OH*	$\omega_\perp = 280\,\mathrm{cm^{-1}}$, $\omega_\parallel = 670(2)\,\mathrm{cm^{-1}}$, $\psi = 3380\,\mathrm{cm^{-1}}$	-319 kJ·mol^{-1}
H*	$\omega_\perp = 1291\,\mathrm{cm^{-1}}$, $\omega_\parallel = 157(2)\,\mathrm{cm^{-1}}$	-29** kJ·mol^{-1}
HCOO*	$\omega_\perp = 322\,\mathrm{cm^{-1}}$, $\omega_\parallel = 36(2)\,\mathrm{cm^{-1}}$, $\omega_{rot} = 400(3)\,\mathrm{cm^{-1}}$, $\psi = 758, 1331, 1640, 2879, 1073, 1377\,\mathrm{cm^{-1}}$	-553 kJ·mol^{-1}
CO*	$\omega_\perp = 330\,\mathrm{cm^{-1}}$, $\omega_\parallel = 17(2)\,\mathrm{cm^{-1}}$, $\psi = 2077\,\mathrm{cm^{-1}}$	-181 kJ·mol^{-1}

** Extracted from reference [103], original value 27 kJ·mol^{-1}, well in the range of reported accuracy (3 kJ·mol^{-1}) [12, 13]; ω are frustrated translational parameters; ψ are vibrational constants; the number in parentheses denotes the degeneracy of a specific frequency.

Table A.3: Thermodynamic data, gas phase [10–13].

Species	Vibrational parameters	Ground state energy
$H_{2(g)}$	$B = 60.8\,\mathrm{cm^{-1}}$, $\sigma = 2$, $\psi = 4405\,\mathrm{cm^{-1}}$	-35 kJ·mol^{-1}
$CO_{2(g)}$	$B = 0.39\,\mathrm{cm^{-1}}$, $\sigma = 2$, $\psi = 1340, 667(2), 2350\,\mathrm{cm^{-1}}$	-433 kJ·mol^{-1}
$CO_{(g)}$	$B = 1.90\,\mathrm{cm^{-1}}$, $\sigma = 1$, $\psi = 2170\,\mathrm{cm^{-1}}$	-132 kJ·mol^{-1}
$H_2O_{(g)}$	$I_{abc} = 5.77 \cdot 10^{-141}\,\mathrm{kg^3 \cdot m^6}$, $\sigma = 2$, $\psi = 1590, 3660, 3760\,\mathrm{cm^{-1}}$	-306 kJ·mol^{-1}
$CH_3OH_{(g)}$	$I_a = 6.578 \cdot 10^{-47}\,\mathrm{kg \cdot m^2}$, $I_b = 34 \cdot 10^{-47}\,\mathrm{kg \cdot m^2}$, $I_c = 35.3 \cdot 10^{-47}\,\mathrm{kg \cdot m^2}$, $\sigma = 3$, $\psi = 270, 1033, 1060, 1165, 1345, 1477(2), 1455, 2844, 2960, 3000, 3681\,\mathrm{cm^{-1}}$	-343 kJ·mol^{-1}

ψ are vibrational constants; I is the moment of inertia, σ the symmetry number and B the rotational constant; the number in parentheses denotes the degeneracy of a specific frequency.

A.2 Additional information microkinetic model

Table A.4: Rate constants [13].

Rate constant	A	E_a
$k_{2,111}, k_{2,100}$	$2.6{\cdot}10^{14}\,s^{-1}$	$114\,kJ{\cdot}mol^{-1}$
$k_{4,111}, k_{4,100}$	$2.3{\cdot}10^{8}\,s^{-1}$	$99\,kJ{\cdot}mol^{-1}$
$k_{7,111}$	$1.1{\cdot}10^{13}\,s^{-1}$	$72\,kJ{\cdot}mol^{-1}$
$k_{7,100}$	$1.8{\cdot}10^{13}\,s^{-1}$	$87\,kJ{\cdot}mol^{-1}$
$k_{2,110}$	$7.7{\cdot}10^{12}\,s^{-1}$	$91\,kJ{\cdot}mol^{-1}$
$k_{4,110}$	$6.3{\cdot}10^{8}\,s^{-1}$	$114\,kJ{\cdot}mol^{-1}$
$k_{7,110}$	$1.8{\cdot}10^{13}\,s^{-1}$	$85\,kJ{\cdot}mol^{-1}$

Calculation of intermediates [10]:

$$\begin{aligned}(\theta^*)^{-1} = 1 &+ \sqrt{\frac{f_{H_2}}{K_5 p_0}} + K_1\frac{f_{H_2O}}{p_0} + K_6\frac{f_{CO}}{p_0} + \frac{1}{K_8}\frac{f_{CO_2}}{p_0} \\ &+ \sqrt{\frac{K_1 f_{H_2O}}{K_3 p_0}}\left(\frac{-b+\sqrt{b^2-4ac}}{2a}\right) + \frac{K_9}{K_8}\sqrt{\frac{f_{H_2}}{K_5 p_0}}\frac{f_{CO_2}}{p_0} \\ &+ \frac{K_9 K_{10}}{K_5 K_8}\frac{f_{H_2} f_{CO_2}}{p_0^2} + \frac{1}{K_{13}}\frac{f_{CH_3OH}}{p_0} + \frac{1}{K_{12}K_{13}}\frac{f_{CH_3OH}}{p_0} \\ &\cdot\left(\frac{f_{H_2}}{K_5 p_0}\right)^{-1/2} + \left(\frac{-b+\sqrt{b^2-4ac}}{2a}\right)^2\end{aligned} \tag{A.1}$$

$$\theta_{HCOO} = \frac{K_9}{K_8}\sqrt{\frac{f_{H_2}}{K_5 p_0}}\frac{f_{CO_2}}{p_0}\theta^* \tag{A.2}$$

$$\theta_H = \sqrt{\frac{f_{H_2}}{K_5 p_0}}\theta^* \tag{A.3}$$

$$\theta_{H_3CO} = \frac{1}{K_{12}K_{13}}\frac{f_{CH_3OH}}{p_0}\left(\frac{f_{H_2}}{K_5 p_0}\right)^{-1/2}\theta^* \tag{A.4}$$

$$\theta_O = \left(\frac{-b+\sqrt{b^2-4ac}}{2a}\right)^2\theta^* \tag{A.5}$$

$$\theta_{CO} = K_6\frac{f_{CO}}{p_0}\theta^* \tag{A.6}$$

$$\theta_{CO_2} = \frac{1}{K_8}\frac{f_{CO_2}}{p_0}\theta^* \tag{A.7}$$

with

$$a = 2k_7K_6\frac{f_{CO}}{p_0} + 2\frac{k_{11}}{K_{11}K_{12}K_{13}}\frac{f_{CH_3OH}}{p_0}\left(\frac{f_{H_2}}{K_5p_0}\right)^{-1/2} + \frac{k_4}{K_4}\sqrt{\frac{f_{H_2}}{K_5p_0}} \tag{A.8}$$

$$b = \frac{k_2}{K_2}\sqrt{\frac{K_1}{K_3K_5}\frac{f_{H_2}f_{H_2O}}{p_0^2}} - k_4\sqrt{\frac{K_1f_{H_2O}}{K_3p_0}} \tag{A.9}$$

$$c = -2\frac{k_7}{K_7K_8}\frac{f_{CO_2}}{p_0} - k_2K_1\frac{f_{H_2O}}{p_0} - 2k_{11}\frac{K_9K_{10}}{K_8}\frac{f_{CO_2}}{p_0}\left(\frac{f_{H_2}}{K_5p_0}\right)^{3/2} \tag{A.10}$$

A.3 Additional information LHHW model

Normalized concentration of free active sites [59]:

$$\beta = \theta^* = \frac{-b + \sqrt{b^2 + 4a}}{2a}, \tag{A.11}$$

with:

$$a = K_2c_tK_3K_4\sqrt{K_{H_2}}f_{CO_2}\sqrt{f_{H_2}} + \frac{K_2c_tK_{H_2O}}{K_{H_2}K_8K_9}\frac{f_{H_2O}f_{CO_2}}{f_{H_2}} \tag{A.12}$$

$$b = 1 + \frac{K_{H_2O}}{K_{H_2}K_8K_9}\frac{f_{H_2O}}{f_{H_2}} + \sqrt{K_{H_2}f_{H_2}} + K_{H_2O}f_{H_2O} \tag{A.13}$$

A.4 Comparisons of the kinetic models

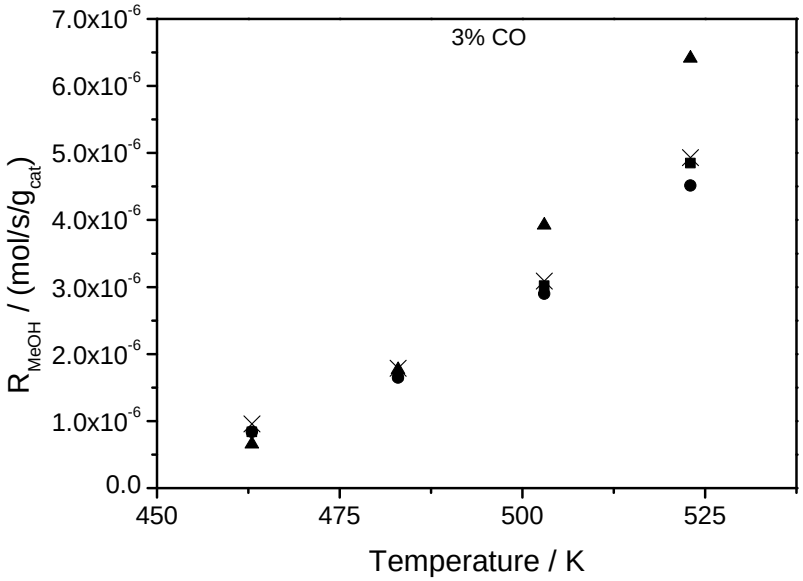

Figure A.1: Comparison of the kinetic models; (x) experimental, ■ power law model, • LHHW model, ▲ microkinetic model, standard feed with varied CO content (3%), p = 60 bar, Q = 100 Nml·min^{-1}.

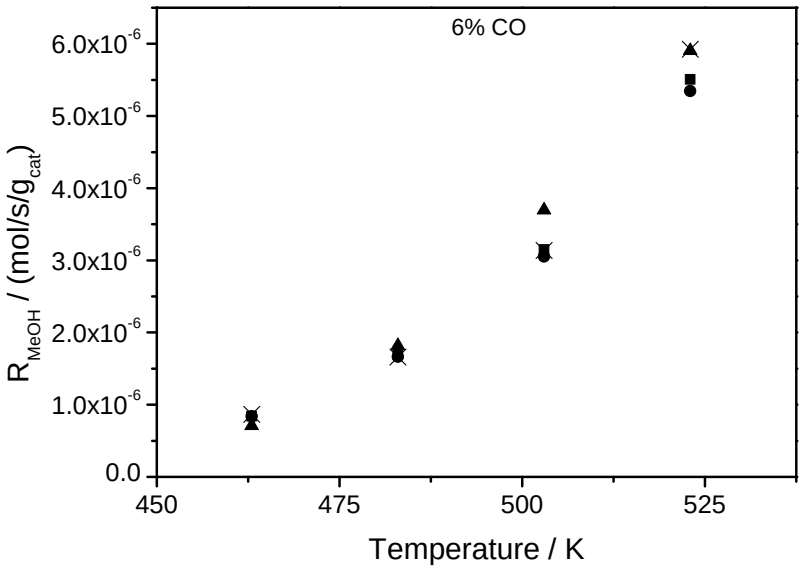

Figure A.2: Comparison of the kinetic models; (x) experimental, ■ power law model, • LHHW model, ▲ microkinetic model, standard feed with varied CO content (6%), p = 60 bar, Q = 100 Nml·min^{-1}.

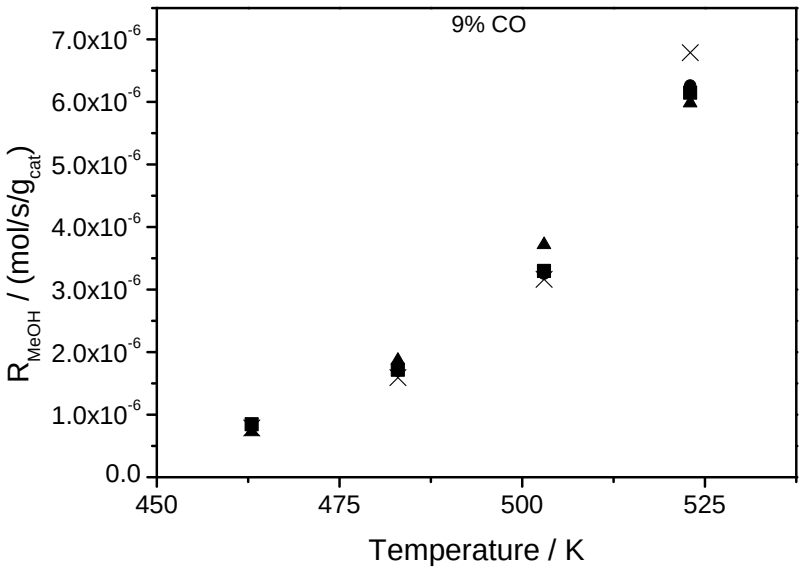

Figure A.3: Comparison of the kinetic models; (x) experimental, ■ power law model, • LHHW model, ▲ microkinetic model, standard feed with varied CO content (9%), p = 60 bar, Q = 100 Nml·min^{-1}.

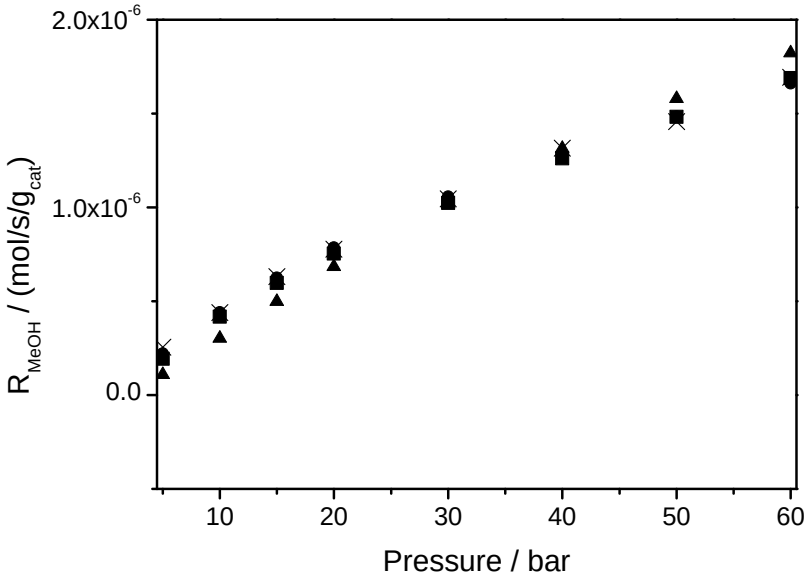

Figure A.4: Comparison of the kinetic models, total pressure variation; (x) experimental, ■ power law model, • LHHW model, ▲ microkinetic model, standard feed, T = 483 K, Q = 100 Nml·min^{-1}.

Curriculum vitae

Personal

Name:	Maximilian Peter
Date of birth:	12.05.1983
Place of birth:	Ingolstadt
Nationality:	German

Education

since 05/2008	**Technische Universität München** Doctoral candidate, Chair of Chemical Engineering, Prof. Dr.-Ing. Kai-Olaf Hinrichsen Topic: "Mechanistic modeling of reaction kinetics and dynamic changes in catalyst morphology on a mesoscopic scale"
10/2003 - 03/2008	**Technische Universität München** Chemical engineering studies Diploma thesis: "Hydrogenation of COS and CS_2 over supported, transition metal promoted, potassium thiomolybdate catalysts" Degree: Diplom-Ingenieur
05/2007 - 09/2007	**Unversity of Wisconsin-Madison** Visiting researcher, topic: "C-C linkling by aldol condensation of furfurals and ketones in a biphasic system for a jetfuel production process"
09/1993 - 06/2002	**Katharinen-Gymnasium Ingolstadt** Qualification: Abitur

Alternative military service

09/2002 - 06/2003 **Klinikum Ingolstadt**
Civilian service

Internships

08/2006 - 11/2006 **Audi AG, Ingolstadt**
07/2003 - 09/2003 **Conti Temic microelectronic GmbH, Ingolstadt**

Publications

Journal Publications

- M. Peter, M.B. Fichtl, H. Ruland, S. Kaluza, M. Muhler and O. Hinrichsen: *Detailed Kinetic Modeling of Methanol Synthesis over a Ternary Copper Catalyst.* Chapter 3: Chem. Eng. J., http://dx.doi.org/10.1016/j.cej.2012.06.066, **2012**.
- M .Peter, J. Fendt, H. Wilmer and O. Hinrichsen: *Modeling of Temperature-Programmed Desorption (TPD) Flow Experiments from $Cu/ZnO/Al_2O_3$ Catalysts.* Chapter 5: Catal. Lett., 142:547–556, **2012**.
- M. Peter, J. Fendt, S. Pleintinger and O. Hinrichsen: *On the Interaction of Carbon Monoxide with Ternary $Cu/ZnO/Al_2O_3$ Catalysts: Modeling of Dynamic Morphology Changes and the Influence on Elementary Step Kinetics.* Chapter 6: Catal. Sci. Technol., http://dx.doi.org/10.1039/C2CY20189E, **2012**.
- R. M. West, Z. Y. Liu, M. Peter and J. A. Dumesic: *Liquid Alkanes with Targeted Molecular Weights from Biomass-Derived Carbohydrates.* ChemSusChem, 1:417-424, **2008**.
- R.M. West, Z.Y. Liu, M. Peter, C.A. Gärtner and J.A. Dumesic: *Carbon–Carbon Bond Formation for Biomass-Derived Furfurals and Ketones by Aldol Condensation in a Biphasic System.* Journal of Molecular Catalysis A: Chemical, 296:18-27, **2008**.

Selected conference paper

- M. Peter, J. Fendt, S. Pleintinger and O. Hinrichsen: *Modeling the Dynamic Morphology Changes of a Ternary $Cu/ZnO/Al_2O_3$ Catalyst under Ambient Pressure.* 45. Jahrestreffen Deutscher Kataytiker, Weimar, **2012**.
- M. Peter, O. Hinrichsen, H. Ruland, S. Kaluza and M. Muhler: *Microkinetics of Methanol Synthesis under Industrial Conditions.* 45. Jahrestreffen Deutscher Kataytiker, Weimar, **2012**.
- M. Peter, O. Hinrichsen, H. Ruland, S. Kaluza and M. Muhler: *Engineering Multiscale Modeling: Differently Detailed Models to Describe Methanol Synthesis over a Ternary Copper Catalyst.* EuropaCat X, Glasgow, **2011**.

- M. Peter, J. Fendt and O. Hinrichsen: *A Numerical Method to Interpret Data from Temperature-Programmed Desorption Experiments.* IDECAT Workshop Advanced utilisation of temperature-programmed experiments in catalysis research, Helsinki, **2010**.
- M. Peter, T. von Aretin und O. Hinrichsen: *Multiskalen-Modellierung: Mesoskopische Modellierung der Methanol-Synthesereaktion.* 43. Jahrestreffen Deutscher Kataytiker, Weimar, **2010**.

List of Tables

List of Figures

Bibliography

[1] R.D. Cortright and J.A. Dumesic: *Kinetics of Heterogeneous Catalytic Reactions: Analysis of Reaction Schemes.* Adv. Catal., 46:161–264, 2001.

[2] J.A. Dumesic, D.F. Rudd, L.M. Aparicio, J.E. Rekoske and A.A. Treviño: *The Microkinetics of Heterogeneous Catalysis.* ACS Professional Reference Book, 1993.

[3] Nobelprize.org: *The Nobel Prize in Chemistry 2007.* http://www.nobelprize.org, 2011.11.19.

[4] O. Hinrichsen: *Kinetic Simulation of Ammonia Synthesis Catalyzed by Ruthenium.* Catal. Today, 53:177–188, 1999.

[5] M. Bowker, I.B. Parker and K.C. Waugh: *Extrapolation of the Kinetics of Model Ammonia Synthesis Catalyst to Industrially Relevant Temperatures and Pressures.* Appl. Catal., 14:101–118, 1985.

[6] M. Bowker, I. Parker and K.C. Waugh: *The Application of Surface Kinetic Data to the Industrial Synthesis of Ammonia.* Surf. Sci., 197:223–229, 1988.

[7] P. Stoltze: *Surface Science as the Basis for the Understanding of the Catalytic Synthesis of Ammonia.* Phys. Scr., 36:824–64, 1987.

[8] P. Stoltze and J.K. Nørskov: *Bridging the "Pressure Gap" between Ultrahigh-Vacuum Surface Physics and High-Pressure Catalysis.* Phys. Rev. Lett., 55:2502–2505, 1985.

[9] P. Stoltze and J.K. Nørskov: *A Description of the High-Pressure Ammonia Synthesis Reaction Based on Surface Science.* J. Vac. Sci. Technol. A, 5:581–585, 1987.

[10] T.S. Askgaard, J.K. Nørskov, C.V. Ovesen and P. Stoltze: *A Kinetic Model of Methanol Synthesis.* J. Catal., 156:229–242, 1995.

[11] C.V. Ovesen: *Kinetic Modeling of Reactions on Cu Surfaces.* PhD thesis, Technical University of Denmark, 1992.

[12] C.V. Ovesen, B.S. Clausen, B.S. Hammershøi, G. Steffensen, T. Askgaard, I. Chorkendorff, J.K. Nørskov, P.B. Rasmussen, P. Stoltze and P. Taylor: *A Microkinetic Analysis of the Water-Gas Shift Reaction under Industrial Conditions.* J. Catal., 158:170–80, 1996.

[13] C.V. Ovesen, B.S. Clausen, J. Schiøtz, P. Stoltze, H. Topøse and J.K. Nørskov: *Kinetic Implications of Dynamical Changes in Catalyst Morphology during Methanol Synthesis over Cu/ZnO Catalysts.* J. Catal., 168:133–142, 1997.

[14] C.V. Ovesen, P. Stoltze, J.K. Nørskov and C.T. Campbell: *A Kinetic Model of the Water Gas Shift Reaction.* J. Catal., 134:445–468, 1992.

[15] P.B. Rasmussen, P.A. Taylor and I. Chorkendorff: *The Interaction of Carbon Dioxide with Cu(100).* Surf. Sci., 269/270:352–359, 1992.

[16] P.B. Rasmussen, P.M. Holmblad, T. Askgaard, C.V. Ovesen, P. Stoltze, J.K. Nørskov and I. Chorkendorff: *Methanol Synthesis on Cu(100) from a Binary Gas Mixture of CO_2 and H_2.* Catal. Lett., 26:373–81, 1994.

[17] P.A. Taylor, P.B. Rasmussen, C.V. Ovesen, P. Stoltze and I. Chorkendorff: *Formate Synthesis on Cu(100).* Surf. Sci., 261:191–206, 1992.

[18] J.B. Hansen and P.E. Højlund Nielsen: *Methanol Synthesis.* in: Handbook of Heterogeneous Catalysis, Vol. 6 (Eds. G. Ertl, H. Knözinger, F. Schüth and J. Weitkamp). Wiley-VCH, 2008.

[19] G.A. Olah, A. Goeppert and G.K.S. Prakash: *Beyond Oil and Gas: The Methanol Economy.* Wiley-VCH, 2009.

[20] The Methanol Institute: *Global Methanol Supply and Demand.* http://www.methanol.org, 2011.09.08.

[21] J.B. Wagner, P.L. Hansen, A.M. Molenbroek, H. Topsøe, B.S. Clausen and S. Helveg: *In Situ Electron Energy Loss Spectroscopy Studies of Gas-Dependent Metal-Support Interactions in Cu/ZnO Catalysts.* J. Phys. Chem., 107:7753–7758, 2003.

[22] T. Ressler, B.L. Kniep, I. Kasatkin and R. Schlögl: *The Microstructure of Copper Zinc Oxide Catalysts: Bridging the Materials Gap.* Angew. Chem. Int. Ed. Engl., 44:4704–4707, 2005.

[23] J. Nakamura, Y. Choi and T. Fujitani: *On the Issue of the Active Site and the Role of ZnO in Cu/ZnO Methanol Synthesis Catalysts.* Top. Catal., 22:277–285, 2003.

[24] J.-D. Grunwaldt, A.M. Molenbroek, N.-Y. Topsøe, H. Topsøe, and B.S. Clausen: *In Situ Investigations of Structural Changes in Cu/ZnO Catalysts.* J. Catal., 194:452–460, 2000.

[25] B.S. Clausen, J. Schiøtz, L. Grabaek, C.V. Ovesen, K.W. Jacobsen, J.K. Nørskov and H. Topsøe: *Wetting/non-wetting Phenomena during Catalysis: Evidence from in situ on-line EXAFS Studies of Cu-Based Catalysts.* Top. Catal., 1:367–376, 1994.

[26] N.-Y. Topsøe and H. Topsøe: *FTIR Studies of Dynamic Surface Structural Changes in Cu-based Methanol Synthesis Catalysts.* J. Mol. Catal. A: Chem., 141:95–105, 1999.

[27] N.-Y. Topsøe and H. Topsøe: *On the Nature of Surface Structural Changes in Cu/ZnO Methanol Synthesis Catalysts.* Top. Catal., 8:267–270, 1999.

[28] P.L. Hansen, J.B. Wagner, S. Helveg, J.R. Rostrup-Nielsen, B.S. Clausen and H. Topsøe: *Atom-Resolved Imaging of Dynamic Shape Changes in Supported Copper Nanocrystals.* Science, 295:2053–2055, 2002.

[29] P.C.K. Vesborg, I. Chorkendorff, I. Knudsen, O. Balmes, J. Nerlov, A.M. Molenbroek, B.S. Clausen and S. Helveg: *Transient Behavior of Cu/ZnO-based Methanol Synthesis Catalysts.* J. Catal., 262:65–72, 2009.

[30] I. Løvik: *Modelling, Estimation and Optimization of the Methanol Synthesis with Catalyst Deactivation.* PhD thesis, Norwegian University of Science and Technology, 2001.

[31] L.C. Grabow and M. Mavrikakis: *Mechanism of Methanol Synthesis on Cu through CO_2 and CO Hydrogenation.* ACS Catal., 1:365–384, 2011.

[32] G.C. Chinchen, P.J. Denny, D.G. Parker, M.S. Spencer and D.A. Whan: *Mechanism of Methanol Synthesis from $CO_2/CO/H_2$ Mixtures over Copper/Zinc Oxide/Alumina Catalysts: Use of ^{14}C-Labelled Reactants.* Appl. Catal., 30:333–338, 1987.

[33] G. Liu, D. Willcox, M. Garland and H.H. Kung: *The Role of CO_2 in Methanol Synthesis on Cu-Zn Oxide: An Isotope Labeling Study.* J. Catal., 96:251–260, 1985.

[34] M. Muhler, E. Törnqvist, L.P. Nielsen, B.S. Clausen and H. Topsøe: *On the Role of Adsorbed Atomic Oxygen and CO_2 in Copper Based Methanol Synthesis Catalysts.* Catal. Lett., 25:1–10, 1994.

[35] H.H. Kung: *Deactivation of Methanol Synthesis Catalysts. A Review.* Catal. Today, 11:443–453, 1992.

[36] M. Sahibzada, I.S. Metcalfe and D. Chadwick: *Methanol Synthesis from $CO/CO_2/H_2$ over $Cu/ZnO/Al_2O_3$ at Differential and Finite Conversions.* J. Catal., 174:111–118, 1998.

[37] G. Liu, D. Willcox, M. Garland and H.H. Kung: *The Rate of Methanol Production on a Copper-Zinc Oxide Catalyst: The Dependence on the Feed Composition.* J. Catal., 90:139–146, 1984.

[38] Lurgi GmbH: *Lurgi MegaMethanol®.* http://www.lurgi.com, 2011.11.08.

[39] G.C. Chinchen, K.C. Waugh and D.A. Whan: *The Activity and State of the Copper Surface in Methanol Synthesis Catalysts.* Appl. Catal., 25:101–107, 1986.

[40] W.X. Pan, R. Cao, D.L. Roberts and G.L. Griffin: *Methanol Synthesis Activity of Cu/ZnO Catalysts.* J. Catal., 114:440–446, 1988.

[41] H. Wilmer and O. Hinrichsen: *Dynamical Changes in $Cu/ZnO/Al_2O_3$ Catalysts.* Catal. Lett., 82:117–122, 2002.

[42] M. Kurtz, N. Bauer, C. Büscher, H. Wilmer, O. Hinrichsen, R. Becker, S. Rabe, K. Merz, M. Driess, R.A. Fischer and M. Muhler: *New Synthetic Routes to More Active Cu/ZnO Catalysts Used for Methanol Synthesis.* Catal. Lett., 92:49–52, 2004.

[43] T.M. Yurieva and T.P. Minyukova: *State of Copper in Cu-Zn-Al Oxide Catalysts for Methanol Synthesis.* React. Kinet. Catal. Lett., 29:55–61, 1985.

[44] M. Kurtz, H. Wilmer, T. Genger, O. Hinrichsen and M. Muhler: *Deactivation of Supported Copper Catalysts for Methanol Synthesis.* Catal. Lett., 86:77–80, 2003.

[45] R.T. Figueiredo, A. Martinez-Arias, M.L. Granados and J.L.G. Fierro: *Spectroscopic Evidence of Cu–Al Interactions in Cu–Zn–Al Mixed Oxide Catalysts Used in CO Hydrogenation.* J. Catal., 178:146–152, 1998.

[46] R. Burch, S.E. Golunski and M.S. Spencer: *The Role of Copper and Zinc Oxide in Methanol Synthesis Catalysts.* J. Chem. Soc. Faraday Trans., 86:2683–2691, 1990.

[47] M.M. Günter, T. Ressler, B. Bems, C. Büscher, T. Genger, O. Hinrichsen, M. Muhler and R. Schlögl: *Implication of the Microstructure of Binary Cu/ZnO Catalysts for Their Catalytic Activity in Methanol Synthesis.* Catal. Lett., 71:37–44, 2001.

[48] Y. Choi, K. Futagami, T. Fujitani and J. Nakamura: *The Difference in the Active Sites for CO_2 and CO Hydrogenation on Cu/ZnO-based Methanol Synthesis Catalysts.* Catal. Lett., 73:27–31, 2001.

[49] Y. Choi, K. Futagami, T. Fujitani and J. Nakamura: *The Role of ZnO in Cu/ZnO Methanol Synthesis Catalysts - Morphology Effect or Active Site Model?* Appl. Catal. A, 208:163–167, 2001.

[50] T. Fujitani and J. Nakamura: *The Effect of ZnO in Methanol Synthesis Catalysts on Cu Dispersion and the Specific Activity.* Catal. Lett., 56:119–124, 1998.

[51] J. Skrzypek, J. Sloczynski and S. Ledakowicz: *Methanol Synthesis.* Polish Scientific Publishers, Warsaw, 1994.

[52] G.W. Roberts, D.M. Brown, T.H. Hsiung and J.J. Lewnard: *Deactivation of Methanol Synthesis Catalyst.* Ind. Eng. Chem. Res., 32:1610–1621, 1993.

[53] K. Klier, V. Chatikavanij, R.G. Herman and G.W. Simmons: *Catalytic Synthesis of Methanol from CO/H_2 - IV. The Effects of Carbon Dioxide.* J. Catal., 74:343–360, 1982.

[54] M.V. Twigg and M.S. Spencer: *Deactivation of Copper Metal Catalysts for Methanol Decomposition, Methanol Steam Reforming and Methanol Synthesis.* Top. Catal., 22:191–203, 2003.

[55] V.E. Leonov, M.M. Karavaev, E.N. Tsybina and G.S. Petrishcheva: *Kinetics of Methanol Synthesis on a Low-Temperature Catalyst.* Kinet. Katal., 14:970–975, 1973.

[56] P. Villa, P. Forzatti, G. Buzzi-Ferraris, G. Garone and I. Pasquon: *Synthesis of Alcohols from Carbon Oxides and Hydrogen. 1. Kinetics of the Low-Pressure Methanol Synthesis.* Ind. Eng. Chem. Process Des. Dev., 24:12–19, 1985.

[57] M.A. McNeil, C.J. Schack and R.G. Rinker: *Methanol Synthesis from Hydrogen, Carbon Monoxide and Carbon Dioxide over a $CuO/ZnO/Al_2O_3$ Catalyst: II. Development of a Phenomenological Rate Expression.* Appl. Catal., 50:265–285, 1989.

[58] G.H. Graaf, E.J. Stamhuis and A.A.C.M. Beenackers: *Kinetics of Low-Pressure Methanol Synthesis.* Chem. Eng. Sci., 43:3185–3195, 1988.

[59] K.M. Vanden Bussche and G.F. Froment: *A Steady-State Kinetic Model for Methanol Synthesis and the Water Gas Shift Reaction on a Commercial $Cu/ZnO/Al_2O_3$ Catalyst.* J. Catal., 161:1–10, 1996.

[60] G.C. Chinchen, P.J. Denny, J.R. Jennings, M.S. Spencer and K.C. Waugh: *Synthesis of Methanol. Part 1. Catalysts and Kinetics.* Appl. Catal., 36:1–65, 1988.

[61] I. Chorkendorff and J.W. Niemantsverdriet: *Concepts of Modern Catalysis and Kinetics.* Wiley-VCH, 2007.

[62] P.W. Atkins and J. de Paula: *Physikalische Chemie.* Wiley-VCH, 2006.

[63] T.L. Hill: *An Introduction to Statistical Thermodynamics.* Dover Publications, 1986.

[64] F.H.P.M. Habraken, G.A. Bootsma, P. Hofmann, S. Hachicha and A.M. Bradshaw: *The Adsorption and Incorporation of Oxygen on Cu(110) and its Reaction with Carbon Monoxide.* Surf. Sci., 88:285–298, 1979.

[65] M.A. Vannice: *Kinetics of Catalytic Reactions.* Springer, 2005.

[66] T.J. Keskitalo, M.K. Veringa Niemelae and A.O.I. Krause: *Modeling of the Adsorption and Desorption of CO_2 on Cu/ZrO_2 and ZrO_2 Catalysts.* Langmuir, 23:7612–7619, 2007.

[67] A.B. Mhadeshwar, H. Wang and D.G. Vlachos: *Thermodynamic Consistency in Microkinetic Development of Surface Reaction Mechanisms.* J. Phys. Chem. B, 107:12721–1273, 2003.

[68] G. Wulff: *Zur Frage der Geschwindigkeit des Wachstums und der Auflösung der Krystallflächen.* Kristallogr., 34:449–530, 1901.

[69] L. Vitos, A. Ruban, H. Shriver and J. Kollar: *The Surface Energy of Metals.* Surf. Sci., 411:186–202, 1998.

[70] W. Kaminsky: *WinXMorph: A Computer Program to Draw Crystal Morphology, Growth Sectors and Cross Sections with Export Files in VRML V2.0 utf8-Virtual Reality Format.* J. Appl. Crystallogr., 38:566–567, 2005.

[71] W. Kaminsky: *From CIF to Virtual Morphology Using the WinXMorph Program.* J. Appl. Crystallogr., 40:382–385, 2007.

[72] MathWorks: *Matlab®.* www.mathworks.com, 2010.

[73] M. Caracotsios: *Athena Visual Studio 14.0.* www.athenavisual.com, 2010.

[74] A. Löwe: *Chemische Reaktionstechnik.* Wiley-VCH, 2001.

[75] H.D. Baehr and K. Stephan: *Wärme- und Stoffübertragung.* Springer, 2008.

[76] B.A. Finlayson: *Introduction to Chemical Engineering Computing.* John Wiley & Sons, 2006.

[77] M. Muhler, L.P. Nielsen, E. Törnqvist, B.S. Clausen and H. Topsøe: *Temperature-Programmed Desorption of H_2 as a Tool to Determine Metal Surface Areas of Cu Catalysts.* Catal. Lett., 14:241–249, 1992.

[78] A.M. de Jong and J.W. Niemantsverdriet: *Thermal Desorption Analysis: Comparative Test of Ten Commonly Applied Procedures.* Surf. Sci., 233:355–365, 1990.

[79] J.L. Falconer and J.A. Schwarz: *Temperature-Programmed Desorption and Reaction: Applications to Supported Catalysts.* Catal. Rev., 25:141–227, 1983.

[80] O. Hinrichsen: *Transient Catalytic Studies.* in: Handbook of Heterogeneous Catalysis, Vol. 3 (Eds. G. Ertl, H. Knözinger, F. Schüth and J. Weitkamp). Wiley-VCH, 2008.

[81] J.M. Kanervo, T.J. Keskitalo, R.I. Slioor and A.O.I. Krause: *Temperature-Programmed Desorption as a Tool to Extract Quantitative Kinetic or Energetic Information for Porous Catalysts.* J. Catal., 238:382–393, 2006.

[82] T. Genger: *Mikrokinetische Untersuchungen zur Methanol-Synthese an Cu-Trägerkatalysatoren.* PhD thesis, Ruhr-Universität Bochum, 2000.

[83] G. Emig and E. Klemm: *Technische Chemie.* Springer, 2005.

[84] R.G. Griskey: *Transport Phenomena and Unit Operations.* Wiley-VCH, 2006.

[85] E. Fitzer and W. Fritz: *Technische Chemie.* Springer, 1989.

[86] R.A. Demmin and R.J. Gorte: *Design Parameters for Temperature-Programmed Desorption from a Packed Bed.* J. Catal., 90:32–39, 1984.

[87] O. Levenspiel: *Chemical Reaction Engineering.* John Wiley & Sons, Inc., 1999.

[88] H. Rabitz, M. Kramer and D. Dacol: *Sensitivity Analysis in Chemical Kinetics.* Annu. Rev. Phys. Chem., 34:419–461, 1983.

[89] D.M. Hamby: *A Review of Techniques for Parameter Sensitivity Analysis of Environmental Models.* Environ. Monit. Assess., 32:135–154, 1994.

[90] A. Varma, M. Morbidelli and H. Wu: *Parametric Sensitivity in Chemical Systems.* Cambridge Univerity Press, 1999.

[91] C.T. Campbell: *Finding the Rate-Determining Step in a Mechanism: Comparing DeDonder Relations with the "Degree of Rate Control".* J. Catal., 204:520–524, 2001.

[92] Silicon fire AG: *Silicon fire.* http://www.siliconfire.com, 2011.08.29.

[93] I. Kasatkin, P. Kurr, B. Kniep, A. Trunschke and R. Schlögl: *Role of Lattice Strain and Defects in Copper Particles on the Activity of $Cu/ZnO/Al_2O_3$ Catalysts for Methanol Synthesis.* Angew. Chem. Int. Ed. Engl., 46:7324–7., 2007.

[94] M. Boudart and G. Djega-Mariadassou: *Kinetics of Heterogeneous Catalytic Reactions.* Princeton University Press, 1984.

[95] J. Solsvik and H.A. Jakobsen: *Modeling of Multicomponent Mass Diffusion in Porous Spherical Pellets: Application to Steam Methane Reforming and Methanol Synthesis.* Chem. Eng. Sci., in press, 2011.

[96] G.C. Chinchen, C.M. Hay, H.D. Vanderwell and K.C. Waugh: *The Measurement of Copper Surface Areas by Reactive Frontal Chromatography.* J. Catal., 103:79–86, 1987.

[97] O. Hinrichsen, T. Genger and M. Muhler: *Chemisorption of N_2O and H_2 for the Surface Determination of Copper Catalysts.* Chem. Eng. Technol., 23:956–959, 2000.

[98] J.J.F. Scholten and J.A. Konvalinka: *Reaction of Nitrous Oxide with Copper Surfaces.* Trans. Faraday Soc., 65:2465–2473, 1969.

[99] G.H. Graaf, P.J.J.M. Sijtsema, E.J. Stamhuis and G.E.H. Joosten: *Chemical Equilibrium in Methanol Synthesis.* Chem. Eng. Sci., 41:2883–2890, 1986.

[100] T. Chang, R.W. Rousseau and J.K.. Ferrell: *Use of the Soave Modification of the Redlich-Kwong Equation of State for Phase Equilibrium Calculations. Systems Containing Methanol.* Ind. Eng. Chem. Process Des. Dev., 22:462–8, 1983.

[101] G. Soave: *Equilibrium Constants from a Modified Redlich-Kwong Equation of State.* Chem. Eng. Sci., 27:1197–203, 1972.

[102] H. Wilmer, T. Genger and O. Hinrichsen: *The Interaction of Hydrogen with Alumina-Supported Copper Catalysts: A Temperature-Programmed Adsorption/Temperature-Programmed Desorption/Isotopic Exchange Reaction Study.* J. Catal., 215:188–198, 2003.

[103] M. Peter, J. Fendt, H. Wilmer and O. Hinrichsen: *Modeling of Temperature-Programmed Desorption (TPD) Flow Experiments from $Cu/ZnO/Al_2O_3$ Catalysts.* Catal. Lett., 142:547–556, 2012.

[104] M. Peter, J. Fendt, S. Pleintinger and O. Hinrichsen: *On the Interaction of Carbon Monoxide and Ternary $Cu/ZnO/Al_2O_3$ Catalysts: Modeling of Dynamic Morphology Changes and the Influence on Elementary Step Kinetics.* Catal. Sci. Technol., http://dx.doi.org/10.1039/C2CY20189E, 2012.

[105] J.T. Sun, I.S. Metcalfe and M. Sahibzada: *Deactivation of $Cu/ZnO/Al_2O_3$ Methanol Synthesis Catalyst by Sintering.* Ind. Eng. Chem. Res., 38:3868–3872, 1999.

[106] E.p Supp: *Improved Methanol Process.* Lurgi Kohle und Mineralöltechnik GmbH, 1981.

[107] M. Peter, M.B. Fichtl, H. Ruland, S. Kaluza, M. Muhler and O. Hinrichsen: *Detailed Kinetic Modeling of Methanol Synthesis over a Ternary Copper Catalyst.* Chem. Eng. J., http://dx.doi.org/10.1016/j.cej.2012.06.066, 2012.

[108] C. Küchen and U. Hoffmann: *Investigation of Simultaneous Reaction of Carbon Monoxide and Carbon Dioxide with Hydrogen on a Commercial Copper/Zinc Oxide Catalyst.* Chem. Eng. Sci., 48:3767–3776, 1993.

[109] J.W. Niemantsverdriet: *Spectroscopy in Catalysis.* Wiley-VCH, 2007.

[110] J.B. Miller, H.R. Siddique, S.M. Gates, J.N. Russell Jr., J.T. Yates Jr., J.C. Tully and M.J. Cardillo: *Extraction of Kinetic Parameters in Temperature Programmed Desorption: A Comparison of Methods.* J. Chem. Phys., 87:6725–6732, 1987.

[111] G. Anger, A. Winkler and K.D. Rendulic: *Adsorption and Desorption Kinetics in the Systems H_2/Cu(111), H_2 /Cu(110) and H_2/Cu(100).* Surf. Sci., 220:1–17, 1989.

[112] T. Genger, O. Hinrichsen and M. Muhler: *The Temperature-Programmed Desorption of Hydrogen from Copper Surfaces.* Catal. Lett., 59:137–141, 1999.

[113] J. Tabatabaei, B.H. Sakakini, M.J. Watson and K.C. Waugh: *The Detailed Kinetics of the Desorption of Hydrogen from Polycrystalline Copper Catalysts.* Catal. Lett., 59:143–149, 1999.

[114] X. Xia, J. Strunk, S. Litvinov and M. Muhler: *Influence of Readsorption and Surface Heterogeneity on the Microkinetic Analysis of Temperature-Programmed Desorption Experiments.* J. Phys. Chem. C, 111:6000–6008, 2007.

[115] J.M. Campbell and C.T. Campbell: *The Dissociative Adsorption of H_2 and D_2 on Cu(110): Activation Barriers and Dynamics.* Surf. Sci., 259:1–17, 1991.

[116] B.E. Hayden, D. Lackey and J. Schott: *A Vibrational Study of the Hydrogen Induced Reconstructions on Cu(110).* Surf. Sci., 239:119–126, 1990.

[117] B.E. Hayden and C.L.A. Lamont: *The Energy and Angular Dependence of Dissociative Hydrogen Adsorption on Cu(110).* Chem. Phys. Lett., 160:331–334, 1989.

[118] B.E. Hayden and C.L.A. Lamont: *Coupled Translational-Vibrational Activation in Dissociative Hydrogen Adsorption on Cu(110).* Phys. Rev. Lett., 63:1823–1825, 1989.

[119] O. Hinrichsen, F. Rosowski, M. Muhler and G. Ertl: *Microkinetic Analysis of Temperature-Programmed Experiments in a Microreactor Flow Systems.* Stud. Surf. Sci. Catal., 109:389–400, 1997.

[120] A.R. Balkenende, J.W. Geus, A.J.H.M. Kock and R.J. van der Pas: *The Effect of a Coverage-Dependent Heat of Adsorption on Temperature-Programmed Desorption and Adsorption in Porous Catalysts.* J. Catal., 115:365–375, 1989.

[121] P. Forzatti, E. Tronconi and L. Lietti: *Temperature-Programmed Desorption Technique.* in: Handbook of Heat and Masstransfer, Vol. 3 (Ed. N.P. Cheremisinoff). Gulf Publishing Co., 1988.

[122] J.S. Rieck and A.T. Bell: *Influence of Adsorption and Mass Transfer Effects on Temperature-Programmed Desorption from Porous Catalysts.* J. Catal., 85:143–153, 1984.

[123] P.A. Redhead: *Thermal Desorption of Gases.* Vacuum, 12:203–211, 1962.

[124] D.L. Roberts and G.L. Griffin: *Temperature-Programmed Desorption and Infrared Study of CO and H_2 Adsorption on Cu/ZnO Catalysts.* J. Catal., 110:117–126, 1988.

[125] G.A. Olah: *Beyond Oil and Gas: The Methanol Economy.* Angew. Chem. Int. Edit., 44:2636–2639, 2005.

[126] O. Hinrichsen, T. Genger and M. Muhler: *Probing the Elementary Steps of the Water-gas Shift Reaction over $Cu/ZnO/Al_2O_3$ with Transient Experiments.* Stud. Surf. Sci. Catal., 130:3825–3830, 2000.

[127] K.I. Choi and M.A. Vannice: *CO Oxidation over Pd and Cu Catalysts. IV. Prereduced Al_2O_3-Supported Copper.* J. Catal., 131:22–35, 1991.

[128] O.P. Van Pruissen, M.M.M. Dings and O.L.J. Gijzeman: *Surface and Subsurface Oxygen on Cu(111), Cu(111)-Fe and Cu(110) and Their Influence on the Reduction with CO and H_2.* Surf. Sci., 179:377–386, 1987.

[129] J.W. Evans, M.S. Wainwright, A.J. Bridgewater and D.J. Young: *On the Determination of Copper Surface Area by Reaction with Nitrous Oxide.* Appl. Catal., 7:75–83, 1983.

[130] M.E. Domagala and C.T. Campbell: *The Mechanism of CO Oxidation over Cu(110): Effect of CO Gas Energy.* Catal. Lett., 9:65–70, 1991.

[131] D.F. Cox and K.H. Schulz: *Interaction of CO with Cu^+ Cations: CO Adsorption on $Cu_2O(100)$.* Surf. Sci., 249:138–148, 1991.

[132] F.H.P.M. Habraken, E.P. Kieffer and G.A. Bootsma: *A Study of the Kinetics of the Interactions of O_2 and N_2O with a Cu(111) Surface and of the Reaction of CO with Adsorbed Oxygen Using AES, LEED and Ellipsometry.* Surf. Sci, 83:45–59, 1979.

[133] B.H. Sakakini, J. Tabatabaei, M.J. Watson and K.C. Waugh: *Structural Changes of the Cu Surface of a $Cu/ZnO/Al_2O_3$ Catalyst, Resulting from Oxidation and Reduction, Probed by CO Infrared Spectroscopy.* J. Mol. Catal. A: Chem., 162:297–306, 2000.

[134] F.H.P.M. Habraken and G.A. Bootsma: *The Kinetics of the Interactions of O_2 and N_2O with a Cu(110) Surface and of the Reactions of CO with Adsorbed Oxygen Studied by Means of Ellipsometry, AES and LEED.* Surf. Sci., 87:333–347, 1979.

[135] F.H.P.M. Habraken, C.M.A.M. Mesters and G.A. Bootsma: *The Adsorption and Incorporation of Oxygen on Cu(100) and Its Reaction with Carbon Monoxide; Comparison with Cu(111) and Cu(110).* Surf. Sci., 97:64–282, 1980.

[136] J. Nakamura, J.M. Campbell and C.T. Campbell: *Kinetics and Mechanism of the Water-Gas Shift Reaction Catalysed by the Clean and Cs-Promoted Cu(110) Surface: A Comparison with Cu(111).* J. Chem. Soc. Faraday Trans., 86:2725–2734, 1990.

[137] A.A. Gokhale, J.A. Dumesic and M. Mavrikakis: *On the Mechanism of Low-Temperature Water Gas Shift Reaction on Copper.* J. Am. Chem. Soc., 130:1402–1414, 2008.

[138] C.T. Campbell and K.-H. Ernst: *Forward and Reverse Water-Gas Shift Reactions on Model Copper Catalysts: Kinetics and Elementary Steps.* ACS Sym. Ser., 482:130–142, 1992.

[139] I. Nakamura, T. Fujitani, T. Uchijima and J. Nakamura: *A Model Catalyst for Methanol Synthesis: Zn-Deposited and Zn-Free Cu Surfaces.* J. Vac. Sci. Technol. A, 14:1464–1468, 1996.

[140] S. Kaluza, M. Behrens, N. Schiefenhövel, B. Kniep, R. Fischer, R. Schlögl and M. Muhler: *A Novel Synthesis Route for $Cu/ZnO/Al_2O_3$ Catalysts Used in Methanol Synthesis: Combining Continuous Consecutive Precipitation with Continuous Aging of the Precipitate.* ChemCatChem, 3:189–199, 2011.